Dissertation (Dr. rer. nat.)

Oleksiy Dyachenko

2016

Surface preparation and characterization of CVD and HPHT diamond for quantum computing applications

Dissertation

zur Erlangung des Grades eines
Doktors der Naturwissenschaften (Dr. rer. nat.)
am Fachbereich Physik der Universität Osnabrück

vorgelegt von

Oleksiy Oleksandrovich Dyachenko

Osnabrück, März 2016

Gutachter der Dissertation:

Prof. Dr. Michael Reichling

Prof. Dr. Wolfgang Harneit

Acknowledgements

I would like to express my sincere gratitude to Prof. Dr. Michael Reichling for the opportunity to work in the “Nanoscience” group and for continuous support of my PhD related research.

I would like to thank also my former colleague Dr. Andrij Borodin for his help with the lab instrumentation and measurement techniques utilization.

Besides my advisor, I would like to thank the rest of my thesis committee: Prof. Dr. Wolfgang Harneit, Prof. Dr. Philipp Maass and Dr. Johann Klare for their essential comments and encouragement.

I am also thankful to my colleagues and staff members from the “Nanoscience” group and Osnabrück University, our collaborate partners from Mainz University Jülich Forschungszentrum and Dr. Wolfer from the Fraunhofer Institut für Angewandte Festkörperphysik for diamond sample.

I would like to thank my family: my parents, my brother, my grandparents and my beloved wife for supporting me all the time during my work and my life.

Content:

1. Introduction ……..*8*

2. Diamond structure and properties……*10*

2.1. Diamond bulk properties and types of diamond……*10*

2.2. Synthetic diamond and its classification……*13*

2.3. Diamond surfaces……*17*

2.4. Diamond samples used for this study……..*21*

2.5. Nitrogen vacancy centers (NVCs)……...*22*

3. Principles and experimental techniques……*25*

3.1. Instrumentation……*25*

3.2. Hemispherical energy analyzer (HSA)……*28*

3.3. X-ray photoelectron spectroscopy (XPS)……*31*

3.4. Ultraviolet photoelectron spectroscopy (UPS)……*36*

3.5. Confocal fluorescence microscopy and optically detected magnetic resonance (ODMR)……*40*

3.6. Low energy ion implantation……...*42*

3.7. Contact angle measurements principles……...*45*

3.8. Wet chemical treatment with acids……..*47*

References……*48*

4. Results…….....*51*

4.1. Principles and setup for metastable impact electron spectroscopy (MIES) …….....*51*

4.2. Effect of doping diamond on the near- surface electronic structure..*69*

4.3. Cyclic preparation of diamond (100) with perfect phase purity……*81*

4.4. Influence of wet and dry etching, Ar sputtering and shallow nitrogen implantation on diamond surfaces……*93*

4.4.1. Recovery of the perfect phase purity diamond (100) surface after Ar sputtering induced damage……..*94*

4.4.2. Influence of a wet and dry etching, Ar sputtering and shallow nitrogen implantation via plasma source on a diamond surface…….***97***
4.5. NV centers production in nitrogen implanted diamond……..***100***
4.5.1. Features of nitrogen detection by XPS…….***100***
4.5.2. Shallow NV center production ……***103***
4.5.3. Optical measurements, detection of NV^- centers…….***104***
4.5.4. Effect of X-ray irradiation on the near- surface electronic structure……..***105***
4.6. Effect of the oxidation and hydrogen termination on the diamond surface……***108***
4.6.1. Diamond surface oxidation……..***108***
4.6.2. Diamond surface hydrogen passivation……...***111***
4.7. Hydrogen terminated diamond surface……...***113***
4.8. Fullerene molecule C_{60} deposition on diamond surface……..***115***
5. Instrumentation calibration…….***118***
5.1. XPS calibration……***118***
5.2. Temperature calibration……...***119***
5.3. Plasma source calibration……....***120***
6. Summary……...***121***
References……..***123***
Curriculum Vitae……***125***

List of abbreviations

XPS	X-ray photoelectron spectroscopy
UPS	Ultraviolet photoelectron spectroscopy
MIES	Metastable impact electron spectroscopy
AFM	Atomic force microscopy
ODMR	Optically detected magnetic resonance
UHV	Ultra high vacuum
APD	Avalanche photodiode
WCA	Wet contact angle
CVD	Chemical vapor deposition
HPHT	High pressure high temperature
ppm	Parts per million
ppb	Parts per billion
hwhm	Half width half maximum
GL	Gauss to Lorenz
W_f	Work function
E_B	Binding energy
E_K	Kinetic energy
E_F	Fermi energy
At%	Atomic percent
CB	Conduction band
VB	Valence band
NV	Nitrogen vacancy
ODMR	Optically detected magnetic resonance
ESCA	Electron Spectroscopy for Chemical Analysis
TMP	Turbo molecular pump
DOS	Density of states

Chapter I

1. Introduction

The fast development of the computer industry has nearly reached the maximum possible level for the transistor miniaturization. This maximum has been predicted by Moore's law once transistors become as small as atomic particle. However, even for the modern CPUs chips made using process technologies between 10 and 20 nanometers quantum mechanical phenomenon such as tunneling effect comes into a play. This leads to much more sophisticated chips architecture and to a significant increase in production costs. Thus a new computer technology is required. It is reasonable that the future computer technology should be based on the on the quantum-mechanical phenomena.

There are a several popular quantum computing concepts. The first one is a based on a superconducting integrated circuit has been already realized.[1, 2] A Canadian company D-Wave Systems launched a 512-qubit quantum processor in 2013.[3] Despite of such important contribution a superconducting integrated circuit has a considerable drawback as low temperature conditions are required for the circuit superconductive operation.

Another attractive quantum computing concept is a diamond based quantum computer. This concept has two main advantages namely stable room temperature operation and operational speed implemented by optical read-write. A key element of such a quantum computer is a diamond point defect nitrogen vacancy center (NV center). An individual NV center has been proposed to be used as a basic unit of a diamond based quantum computer.[4-6]

One of the promising diamond based quantum computing concepts proposed by Prof. Dr. Harneit is based on spin coupling interaction between nitrogen doped fullerene atoms ($N@C_{60}$) located on the diamond surface comprising negatively charged nitrogen vacancy (NV^-) centers for information readout. The general view of such a concept is shown in the Fig.1. Main requirements for such a system are a quantum-mechanical two-level system or few-level systems, robust quantum states with long quantum phase coherence and the ability to manipulate states, that allows to perform signal input, calculation, as well as the output of the signal. Another important demand is a truly scalable many qubits architecture.

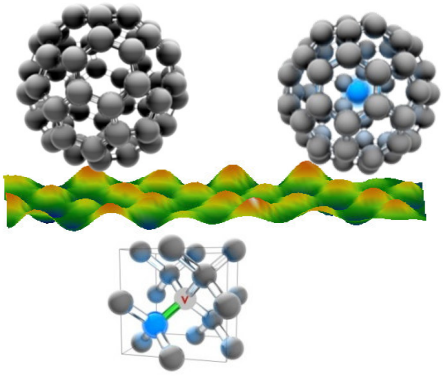

Fig. 1 Drawing of the $N@C_{60}$ and NV^- based quantum computing concept.*

To fulfill all of these requirements, an enhanced concept has been proposed (Fig. 2). According to the new concept design, $N@C_{60}$ should be placed inside single wall carbon nanotubes (SWCNT) allowing to generate perfectly aligned qubits on top of the diamond surface.

The development of such a system is quite a challenging task involving a number of different complex preparation steps. These steps comprise: C_{60} doping with nitrogen, filling

of single wall nanotube (SWCNT) with $N@C_{60}$ fullerenes, controllable nitrogen implantation and formation of NV^- centers in the near surface region.

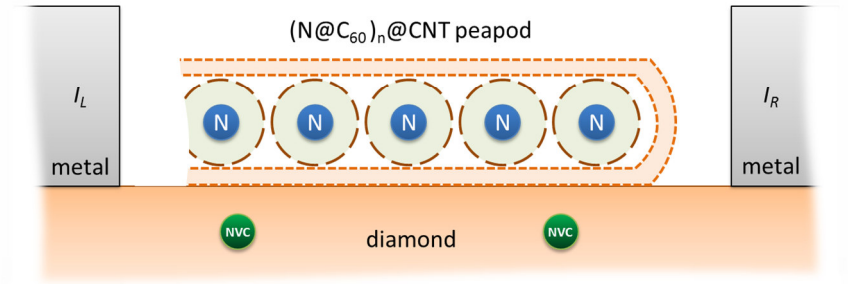

Fig. 2 Drawing of the $N@C_{60}$ encapsulated in the SWCNT and NV^- quantum computing concept.*

The work documented in this thesis is a part of a cooperative effort for establishing quantum computer based on the described principles. The work is focused on the implantation of diamond surfaces and the formation of NV centers. The implantation process is described, including subsequent steps of NV center formation.

In this context, it is also of great importance to control the diamond surface structure, stoichiometry and phase purity as this is essential for the formation of a perfect interface required for the quantum computing concept realization. Therefore, taking into account the large number and the technical complexity of all preparation steps to form such a quantum computing system, the precise analysis of diamond surface is required.

This work comprises studies addressing fundamental questions of the diamond surface physics for different doping concentrations of nitrogen and boron, and how doping is reflected in the core shell analysis, valance band structure and work function values. A second aspect of the work is the controllable creation of nitrogen-vacancy (NVs) centers accompanied by comprehensive surface spectroscopy studies. Additionally, in order to increase and stabilize NV negative (NV^-), which are required for quantum computing system, studies on diverse oxygen termination procedures has been executed. The efficiency of oxygen termination procedures compared and is confirmed by spectroscopy and wet contact angle (WCA) measurements. Furthermore, an alternative method of hydrogen termination of the diamond surface is proposed and compared to the traditional hydrogen plasma termination. As related side aspect, the deposition of C_{60} molecules on the diamond surface is performed and investigated by means of UPS and MIES spectroscopy.

A distinctive experimental capability of studies is the implementation of the Metastable Impact Electron Spectroscopy (MIES) spectroscopy. This unique surface spectroscopy technique and individual instrumentation design for probing the electronic structure of the outermost surface layer, including measurement examples is introduced in this work.

* These figures are used with permission of the Prof. Dr. Harneit.

Chapter II

2. Diamond structure and properties

In this chapter general information and main properties of bulk diamond and diamond surface are presented, and the diamond samples used in studies will be introduced.

2.1. Diamond bulk properties and types of diamond

Diamond is known as a gemstone used in the jewelry industry for ages. At present, diamond is considered as a very promising material for a huge number of applications, due to its remarkable combination of mechanical, physical and chemical properties.

First, diamond attracted attention as an exceptionally hard material, thanks to its high thermal, conductivity and tensile (Young) modulus. It has been logically used for various cutting applications like medical scalpel tools, drilling tools and as a protective and as a resistive coating for aggressive environmental conditions.

Properties	Values	Units
Band gap	5.45	eV
Lattice constant	0.36	nm
Density	3.52	g / cm^3
Atomic density	1.77×10^{23}	cm^{-3}
Dielectric constant	5.7	dimensionless
Mechanical hardness	5700 – 10400	kg / mm^2
Thermal conductivity	22	W / cmK
Thermal expansion coefficient	0.0000011	/ K
Thermal shock parameter	30.000.000	W / m
Debye temperature	2.200	K
Young Modulus	1143	GPa
Electrical resistivity	$> 10^{11}$	Ohm / cm
Optical transmission	220 nm $\leq \lambda \geq$ 2500 nm and $\geq$ 6000 nm	nm
Electron mobility	2.200	cm^2 / Vs
Hole mobility	1.600	cm^2 / Vs
Electron saturated velocity	27.000.000	cm / s
Hole saturated velocity	10.000.000	cm / s
Sound velocity	18.000	m / s
Acids resistivity	yes	
Biocompatibility	yes	

Table 1 Main diamond mechanical, physical and chemical properties.

Diamond is considered as a wide band gap of 5.45 eV semiconductor revealing remarkable electro and optical properties. It has been demonstrated that diamond could be used for high power electronic devices [7, 8], diamond based photonic devices [9], radiation sensors [10], electrochemical [11, 12], biochemical applications [13, 14] and many others. Diamond due to its surface stability and biocompatibility appears to be perfect material for a number of possible biological applications, like surface functionalization[15], drug delivery[16] and implant material[17].

The most remarkable diamond properties are presented in Table 1.[18-21] Carbon atoms could have three allotrope forms namely graphite, diamond and graphene. Under standard conditions graphite, where carbon atoms are arranged in a honeycomb lattice, is the most stable form of carbon. Graphene is a two-dimensional planar sheet of carbon, where carbon atoms are arranged in a honeycomb-shaped lattice. Diamond is a metastable allotrope form of carbon, where carbon atoms are arranged in the face-centered cubic (FCC) crystal lattice, which is also called "diamond lattice". Graphite is thermodynamically more stable than diamond, however under the normal conditions, the conversion rate from the diamond to the graphite form is insignificant. Diamond has a strong covalent bonding between atoms in the lattice and, according to the statistical wave function interpretation proposed by Max Born the density probability amplitude of the bond-forming electrons is concentrated in the space between atoms. The diamond crystal lattice is shown in the Fig. 3, and has a bond length of 0.154 nm and lattice constant is a = 0.357 nm. [22] In graphite, the bond length is 0.142 nm, with the distance between layers of 0.335 nm. [22] The diamond FCC lattice can be considered as consisting of two cubic lattices shifted with respect to each other by (1/4, 1/4, 1/4).

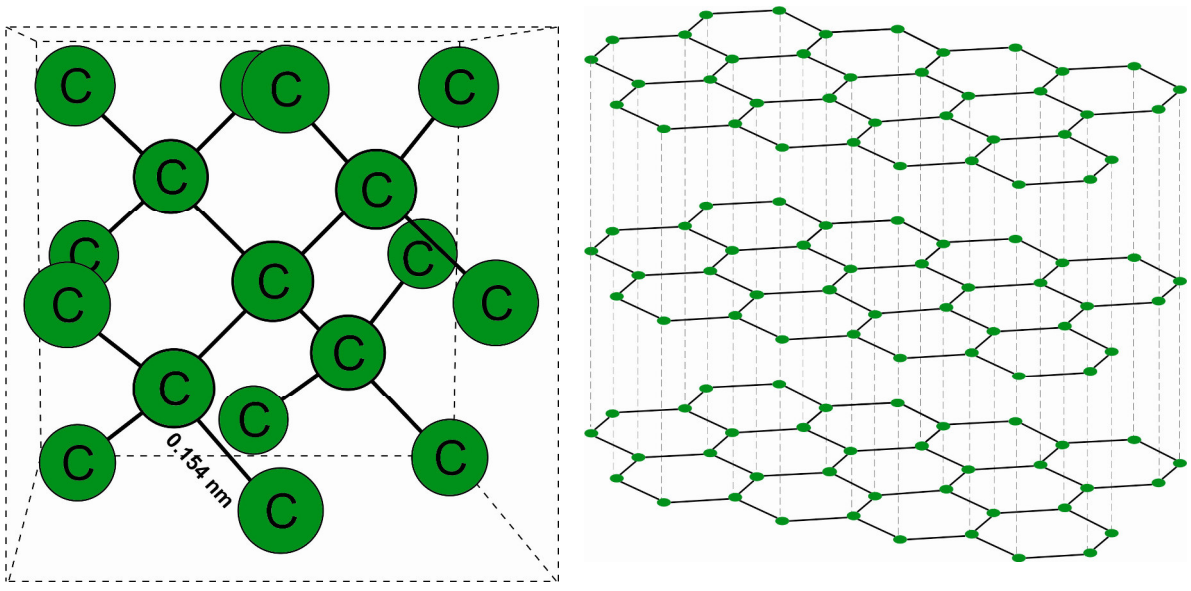

Fig. 3 Diamond lattice structure diagram left, and graphite lattice structure right.

Carbon atoms have four valence electrons on the 2*s* and 2*p* atomic orbitals, thus the carbon-carbon (C-C) bond can be sp^3 or sp^2 hybridized. In diamond, carbon forms a three-dimensional tetrahedral structure due to the sp^3 carbon hybridization that is linked to four other sp^3 hybridized carbon atoms, what results in a mixed state formed from one *s*-orbital

and three *p*-orbitals. The characteristic angle between the hybridized sp^3 configuration orbitals is 109° degree. Comparing to the carbon in graphite, the four carbon valance electrons are used for sp^2 hybridized σ-bonds (characteristic angle 120°) with the three neighbors and the remaining one electron forming the perpendicular π-bond. In the case of amorphous carbon, the C-C bond consists of a mixture of sp^2 and sp^3 hybridized bonds.

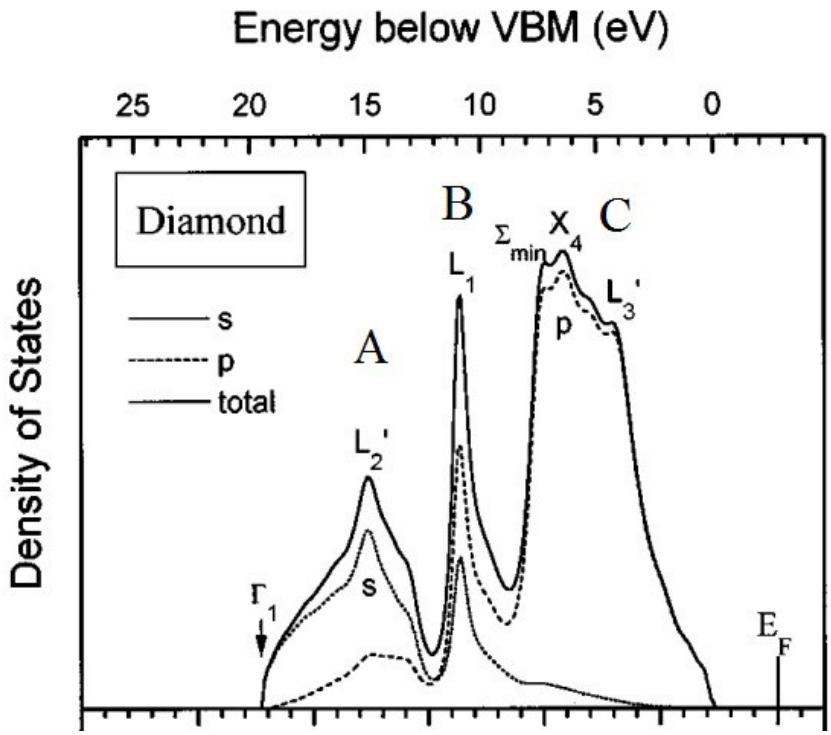

Fig. 4 Calculated partial and total densities of states for diamond by J. Schäfer et al.[23].

Figure 4 shows calculations by J. Schäfer for the partial s-type, p-type and the total valance band DOS for diamond. It is calculated by the same LCAO formalism used for the amorphous structures[23]. Generally, three peaks can be resolved, as it has been reported by earlier DOS calculations [24]; these is a C peak related to σ_p bonds, a B peak associated to the hybridized sp^3 diamond structure, and A peak related to σ_s bonds. The DOS, corrected for the orbital cross-section, should be mirrored in the acquired photoemission spectra from the VB[23] and makes diamond suitable for tracking electronic structure changes by means of ultraviolet- (UPS) or X-ray photoelectron spectroscopy (XPS).

2.2. Synthetic diamond and its classification

First attempts to produce synthetic diamonds are known from the 1879 performed by James Ballantyne Hannay and by Ferdinand Frédéric Henri Moissan in 1893 years, which was in record proved officially much later. However, generally identified research and the establishment of synthetic diamond growth methods refers to the early 1940's, when extensive systematic studies of this topic were started in the USA, Soviet Union and Sweden. This became possible after the detailed phase diagram of the carbon by O. I. Leipunskii in 1939.[25] Figure 5 demonstrates the carbon phase diagram with possible temperature and pressure conditions matching different diamond synthesis production processes.[26]

The term "synthetic diamond" itself has a few alternatives namely "laboratory-grown" and "laboratory-created", that were introduced in order to clarify the origin of the diamond production and not to be mistaken interpreted as synthetic with the meaning of an imitation product.

The two most popular synthetic diamond industrial production methods are Chemical Vapor Deposition (CVD) and High Pressure High Temperature (HPHT) synthesis. There are also two more known methods like the detonation synthesis, which has been used recently for the production of nanodiamonds (NDs) and a fabrication method using high-power ultrasound, which has been demonstrated under laboratory conditions and has so far no industrial application.

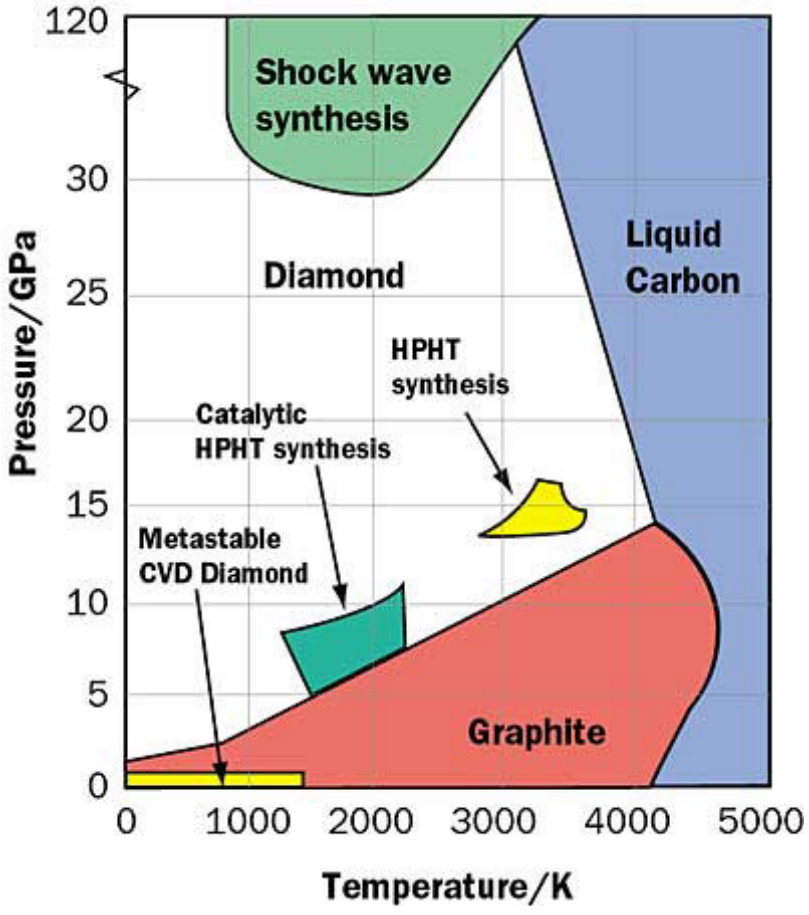

Fig.5 Carbon phase diagram.[26]

HPHT diamond growth

The HPHT method simulates the conditions of the natural diamonds formation in the earth crust. The first commercially successful HPHT diamond production has been reported by the US company General Electric (GE) in 1954. Typical HPHT parameters are as following: pressure values are 5 – 6 GPa and the temperature is ranging from 1300 to 1600° C. The process involves quite complicated technical instrumentation, for instance, a huge hydraulic presses, equipped with numerical anvils pressing systems or cubic presses. This method also requires the utilization a solvent material that is usually a metal (e.g. nickel, cobalt, iron) and a catalyst material, both being a possible source of contamination. Another HPHT drawback is the limitation of the produced diamond samples size to some millimeter. Due to the relatively high nitrogen impurity concentration, HPHT diamonds does not fulfill the requirements for electronic grade electronic devices and is thus not applicable for quantum computing applications, as they contain a significant amount of nitrogen vacancy centers.

CVD diamond growth

To reduce the manufacturing costs and to be able to create larger diamonds a new CVD growth method has been invented. The first successful CVD growth implementation has been reported by researchers W. G. Eversole in1959 [27] and J. C. Angus in 1968 [28], both from the Union Carbide Corporation in the U.S.A. and later in 1980 [29] by scientist B. Derjaguin from USSR.

This method introduces the chemical vapor deposition process, which is a gas-phase chemical reaction on a solid substrate leading to carbon deposition onto the substrate. During the growth, methane gas is introduced in the reactor, then it is activated by an intense plasma or a hot filament to break the hydrocarbon molecules and to produce carbon radicals and atomic hydrogen, which reach the substrate with a certain concentration and a certain temperature gradient. The precise optimization of the growth parameters plays a paramount role in the CVD process as it consists of different reactions in combination all having different rates.

Activated carbon radicals undergo a series of reactions leading to graphite sp^2 bonds and diamond sp^3 bonds formation. Under the condition that growth parameters are properly optimized, sp^2 bonds will be much faster removed by the atomic hydrogen leading to primary diamond growth.

In 1994 P. K. Bachmann presented a C-H-O phase diagram for diamond deposition, based on the reports on over 70 diamond growth experiments, that is now referred as the Bachmann triangle diagram.[30] Figure 6 shows a simplified version of this diagram published by P. May in 2000.[31] It clearly shows that good quality diamond growth follows conditions in the area near the H-CO line. This means that diamond growth is only depended on the ratio of C, H and O rather than the used precursor gases. Nowadays, the CVD diamond growth method is the most popular and extensively used, as it allows growing large diamonds on different types of substrates. Electronic grade quality CVD diamonds are applicable for quantum computing application.

Diamonds could be grown polycrystalline or monocrystalline, this work refers only to monocrystalline or single crystal diamonds. The quality of a sample surface is crucial for a low energy shallow implantation[32], thus monocrystalline diamonds are more suitable for quantum computing applications.

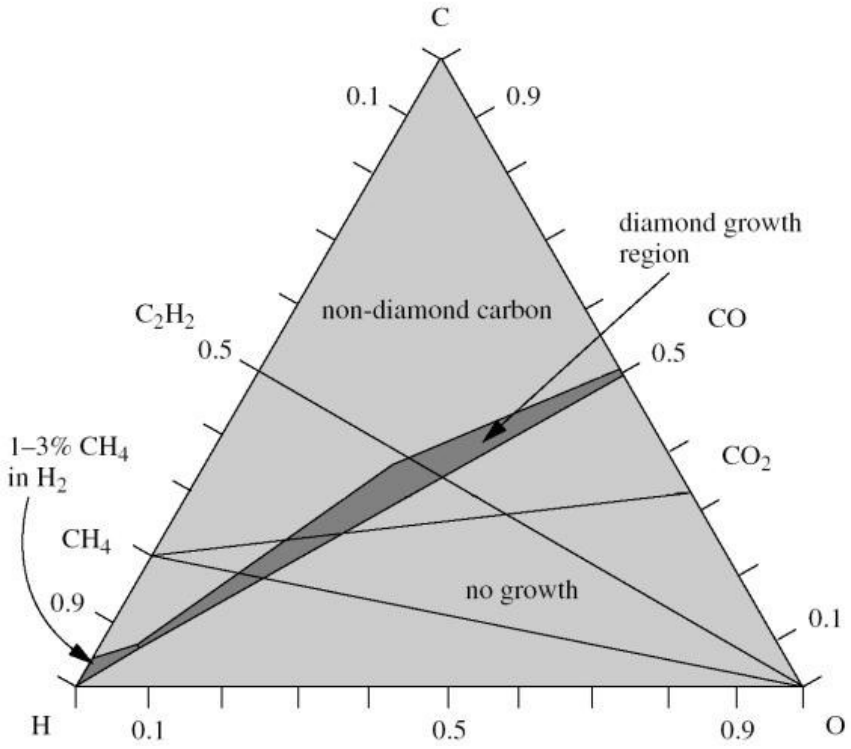

Fig.6 A simplified version of the Bachmann triangle diagram by P. May.[31]

The classification of natural and synthetic diamond is based on the type and quantity of impurities, namely the boron and nitrogen dopant concentration and their specific configurations. Figure 7 is a simplified diagram of different diamond types including defects, configuration type and the way how dopants are incorporated in the diamond lattice [33]. Type I is related to diamond with nitrogen (N) impurities and is divided into Ib type containing isolated single N impurities, and Ia type subdivide into IaA containing N pairs and IaB that comprises of a vacancy surrounded by four N atoms. Type II consists of IIb type with boron impurities and the cleanest IIa diamond type with negligible no nitrogen or boron impurities.

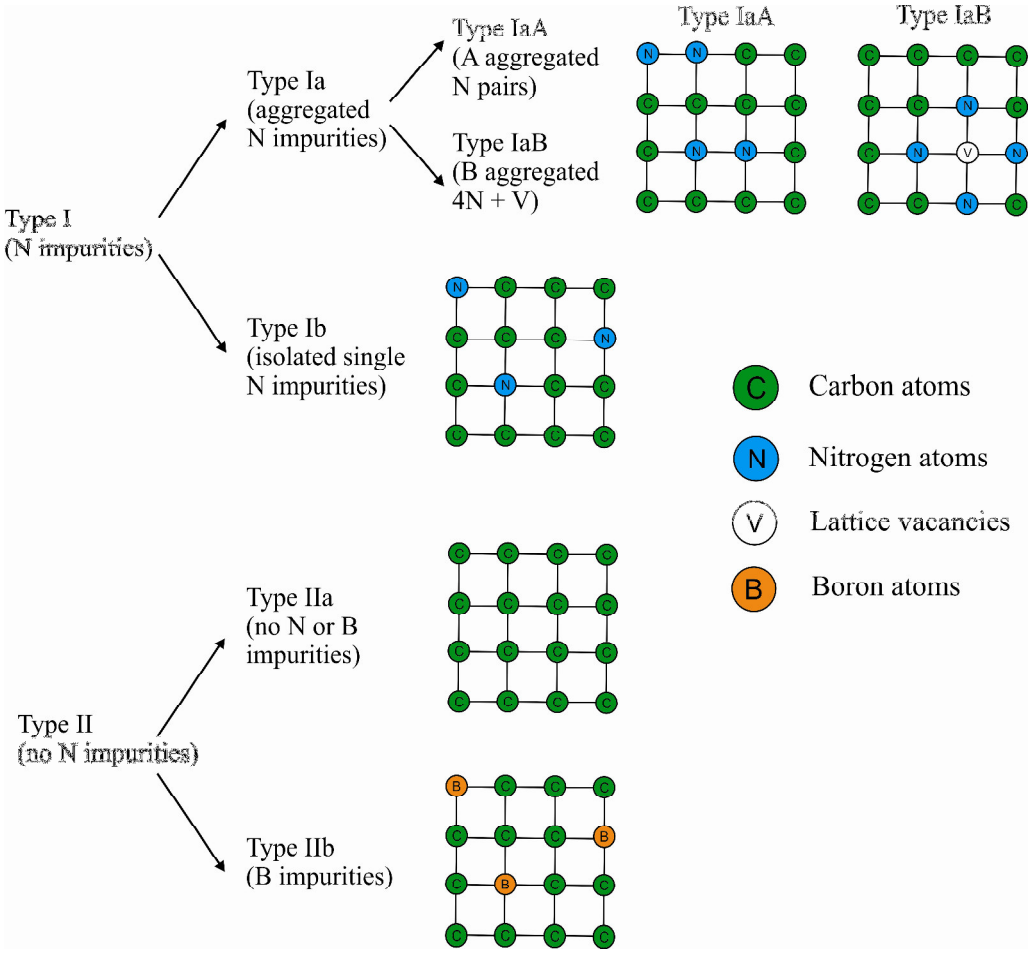

Fig. 7 Simplified diagram illustrates the diamond type classification.

In fact diamonds marked by manufactures as IIa type usually consist of a very small concentration of nitrogen impurities, typically in the range of 1 ppm to a few ppb. Only cleanest ppb or so called electronic grade diamonds are applicable for diamond computing applications.

2.3. Diamond surfaces

Surface properties play a paramount role for a wide range of applications like quantum computing, electrochemical, bio applications and high power electronic devices. For these applications surface termination or functionalization, that can dramatically change material properties, is frequently performed. In this section specific properties of different type diamond surfaces will be presented. As well as the most widespread termination of the diamond surface will be introduced together with the main parameters of these surface types. The diamond surface structure and geometry has been investigated by various techniques like electron energy loss spectroscopy (HREELS), Auger electron spectroscopy (AES), electron loss spectroscopy (ELS) [34], scanning probe microscopy NC-AFM [35], photoelectron spectroscopy [36], theoretically [37] and by many other methods.

The most common diamond crystal orientations are (100) and (111) as they can be selectively grown by CVD process under precise parameter control. The (100) surface is more stable by CVD growth, whereas for the (110) orientation, during growth the gas phase etching processes occurs less frequent. Figure 8 demonstrates possible crystal faces and edge orientations for commercial diamond.

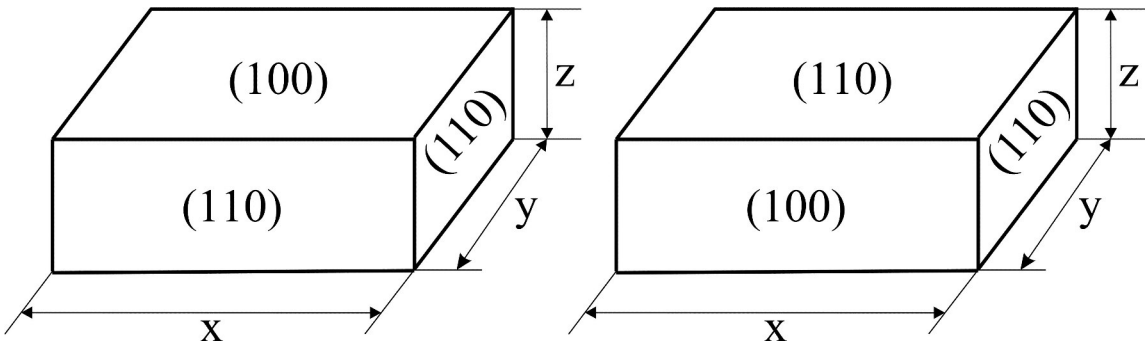

Fig.8 Possible crystal faces and edges orientation for commercial diamonds (left) with (100) face and (right) with (110) geometry

Clean surface

It is very difficult to obtain a clean diamond surface. For a clean diamond (100) surface, each surface carbon atom possesses two dangling bonds, thus the (1 x 1) geometry will be unstable and tends to form a (2 x 1) reconstruction with π-bonded dimer formation by neighboring atoms as shown in Fig. 9. For a clean intrinsic diamond surface π-type, dangling bonds or C-C dimers are expected, which would form a graphene like surface as well as defect clusters. It is remarkable for intrinsic diamond that charge carriers form a hole accumulation layer leading to a prominent surface conductivity (SC).

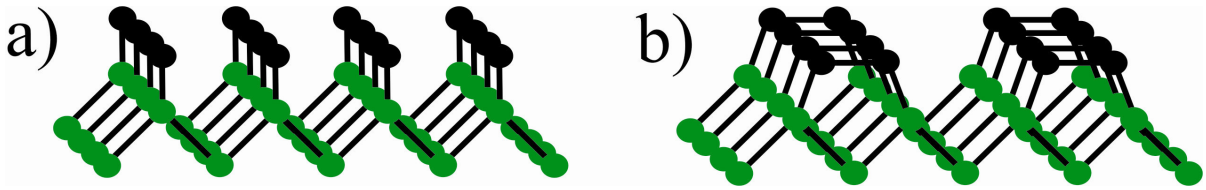

Fig. 9 Atomic structure side view of the ideal (1 x 1) (a) and (b) the (2 x 1) reconstructed π-bonded dimers formation diamond (100) surface.

The C-C dimers are arranged in rows with a weak splitting between dimer orbitals. They form the surface band structure consisting of an empty band that arises from the π* antibonding orbital and an occupied band from the π bonding orbital. This causes a large distance of 2.52 Å between surface dimers and the interplay between them results in broadening of π and π* bands. However, there will be a gap of only 1.3 eV [37] between occupied and unoccupied surface states giving the surface semiconducting properties. It should be noticed that the occupied surface states are placed within the valance band (VB) and do not penetrate in the band gap. According to the density functional theory (DFT) calculation, unoccupied surface states are predicted to be between 1.3 eV and 2.4 eV above the valence band maximum (VBM) [37], and the occupied surface states are found to be in the range -2.0 eV to 0 eV below VBM [37], which and that was confirmed revealing position from -1.9 to -0.2 eV below VBM [38].

Oxygen terminated surface

During the CVD growth, oxygen plays a major role and is responsible for the final crystal quality and defect density. Also, oxygen has an impact on surface conductivety and the shallow nitrogen vacancy centers charge state, for instance conversion from neutral to negative.[39]

There are a few models describing the oxygen bonding stucture on the diamond (100) surface. Diamond oxidation theoretical and experimental studies have been reported in literature describing the formation of atomic oxygen chemisortion in configurations like C-O, C=O, C-O-C and C-OH as shown schematically in Fig. 10. When half of the on-top CO oxygen monolayer is removed the surface will reconstruct from the (1 x 1) to (2 x 1) geometric configuration. For a half monlayer (ML) surface coverage, the C-O-C bridge structure reveals the lowest energy. Theoretical calculations predict an electron affinity of χ = +2.0 eV for the (100) - (1 X 1) C-O-C species, and +3.0 eV for the C=O bonding geometry. Experiments reveal that oxygen favours the bridge C-O-C configuration upon oxidation tretament. Theory and experimental data show occupied surface states around -2eV but no unocupied states[40]. The presence of chemisorped oxygen species suppresses surface conductivity and leads to the so-called positive electron affinety (PEA).

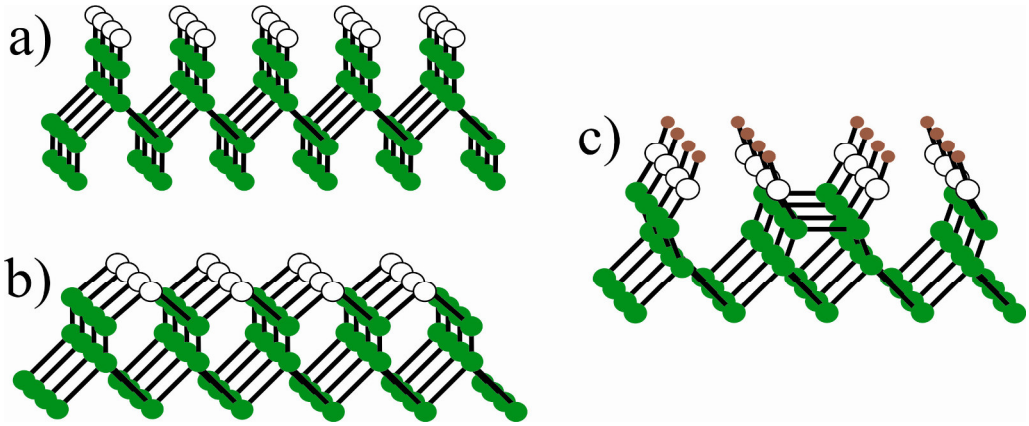

Fig. 10 Schematic drawings of possible oxygen groups on diamond (100): (a) ether or bridging (C-O-C); (b) carbonyl (C=O) fully covered surface; (c) hydroxyl (C-OH).

Hydrogen terminated surface

The hydrogen terminated surface has attracted significant attention as it exhibits a low or 'negative' electron affinity (NEA) and makes it feasible to use it for photon-emitter applications. Also it exhibits surface the conductivity required for a number of applications like electronic or surface functionalization. All as-grown CVD diamond samples contain hydrogen as it is always present in the reactors.

Hydrogen plasma-treated (100) surfaces are expected to have one hydrogen atom per surface carbon atom, what implies that the surface uniformly terminated by monohydride in a (2 x 1) arrangement. Having such a termination, the surface is quite stable and unreactive in normal atmosphere. However, under vacuum conditions, annealing at elevated temperature in molecular oxygen leads to surface oxidation.[34] Figure 11 presents possible hydrogen bonding configurations on (100) surface such as the formation of monohydride dimers or the termination formation when each of the two carbon dangling bonds are passivated by hydrogen. The π and π^* bands of the clean surface will be replaced by the bonding and antibonding states of the carbon-hydrogen bonds due to the change in bonding structure after hydrogen termination. Due to that fact the corresponding surface states will be shifted more than 2 eV below the VBM. The unoccupied surface states from theory are predicted in the range from 3.3 to 6.0 eV [37] above the VBM, notably these states located in the band gap close to the conduction band minimum (CBM) and would be extending into the CB itself, what lead to the negative electron affinity properties on H-terminated diamond surface. At the same time no occupied surface states within the gap could be revealed by photoemission experiments, which is in a good agreement with the theoretical calculation.[41, 42]

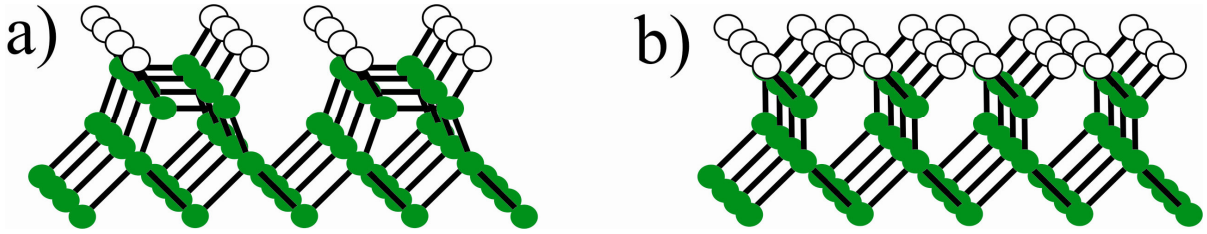

Fig. 11 Hydrogen terminated (100) (2x1) diamond surface (a) shows monohydrid dimers and (b) shows case when two dangling bonds per carbon are H-terminated.

It should be noticed that when discussing the phenomenon of NEA, one should distinguish between true and effective electron affinity [43]. Namely the true NEA means the vacuum level (E_{vac}) at the surface positioned below the CBM, thus electrons excited into the CB can be easily emitted into the vacuum. The NEA effect strongly depends on diamond doping, for instance, the H terminated (100)-(2×1) surface of boron doped diamond reveals a strong NEA, however, it is not noticeable for the H passivated (100)-(2×1) surface of nitrogen doped diamond due to strong upward band bending.[44]

2.4. Diamond samples used for this study

Most part of our samples are produced by Element Six (Element Six Ltd., Ascot, United Kingdom) by CVD or HPHT grows methods. Boron doped samples have been received from the Fraunhofer Institut für Angewandte Festkörperphysik (IAF, Freiburg, Germany). In Table 2, the main parameters of the samples are presented.

Sample #	Size (mm)	Company	Type	Description
OS5	3x3	Element Six	IIa	H-terminated
OS20, OS21, OS22, OS 23	4.5x4.5	Element Six	IIa	N < 1 ppm, B< 0.05 ppm
OS 9, OS 10, OS 31-35, OS 41-45	3x3	Element Six	IIa	N < 1 ppm, B < 0.05 ppm
OS 46-50, OS 51-55	3x3	Element Six	Ib	HPHT N < 200 ppm, B < 0.1 ppm
OS 56	4.5x4.5	Element Six	Ib	HPHT N < 200 ppm, B < 0.1 ppm
DS7, MZ15	4x4, 3.5x3.5	Element Six	IIa EL	N < 5 ppb, B < 1 ppb

Table 2 Main parameters of diamond samples used in this work.

IIa Element Six CVD (100) diamonds:

- CVD SC Plate 4.5x4.5 mm, 0.5 mm thick, P2
  Typically 100% single sector (100), [N] < 1 ppm, [B] < 0.05 ppm
  Orientation (100) faces, <110> edges

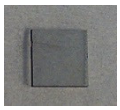

- CVD SC Plate 3.0x3.0 mm, 0.5 mm thick, P2
  Typically 100% single sector (100), [N] < 1 ppm, [B] < 0.05 ppm
  Orientation (100) faces, <100> edges

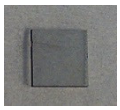

- CVD SC Plate Electronic grade, P2
  Typically 100% single sector (100), [N] < 5ppb, [B] < 1 ppb
  Orientation (100) faces, <110> edges

Ib Element Six HPHT (100) diamonds:

- SC Plate Type Ib 3.0x3.0x0.3mm, PL
  Typically 80% single sector (100), [N] < 200 ppm, [B] < 0.1 ppm
  Side 1 Ra < 10 nm; Side 2 Ra < 250 nm
  Orientation (100) faces, <110> edges

- IIb Boron doped diamond:
  Boron doped IIb type sample with the (111) orientation
  B ~ 100ppm

2.5. Nitrogen vacancy centers (NVCs)

Diamond is one of the hardest materials and has a close-packed lattice structure, however, it is also known to usually contain many defects. One of the most remarkable diamond point defects is the nitrogen vacancy (NV) color center schematically depicted in Fig. 12. The Nv center exhibits magnetic and quantum behavior that is stable at room temperature (RT). The most intriguing aspect is the ability of NV centers to measure magnetic and electric fields because of the quantum mechanical interactions of the defect spin state. This point defect consists of a neighboring pair of a lattice vacancy and a nitrogen atom, where both are positioned substitutional at carbon atom sites. Nitrogen vacancy centers exist as a negatively charged species (NV^-) called the "bright state" and neutrally charged species (NV^0) called the "dark state".[45] The NV^0 has five electrons three from carbon and two from nitrogen, whereas NV^- has six electrons. The NV^- center is practically the more important for applications in quantum computing, quantum magnetometry, electrometry and many others. The NV^- orientation of the defect structure is considered upon its major and minor symmetry axes directions. The overall symmetry is C_{3v} trigonal and has a <111> major symmetry axis as illustrated on the right side of the Fig. 12. There are four possible major symmetry axis alignments for the given [100] crystal orientation and three possible definitions of its minor symmetry axis.

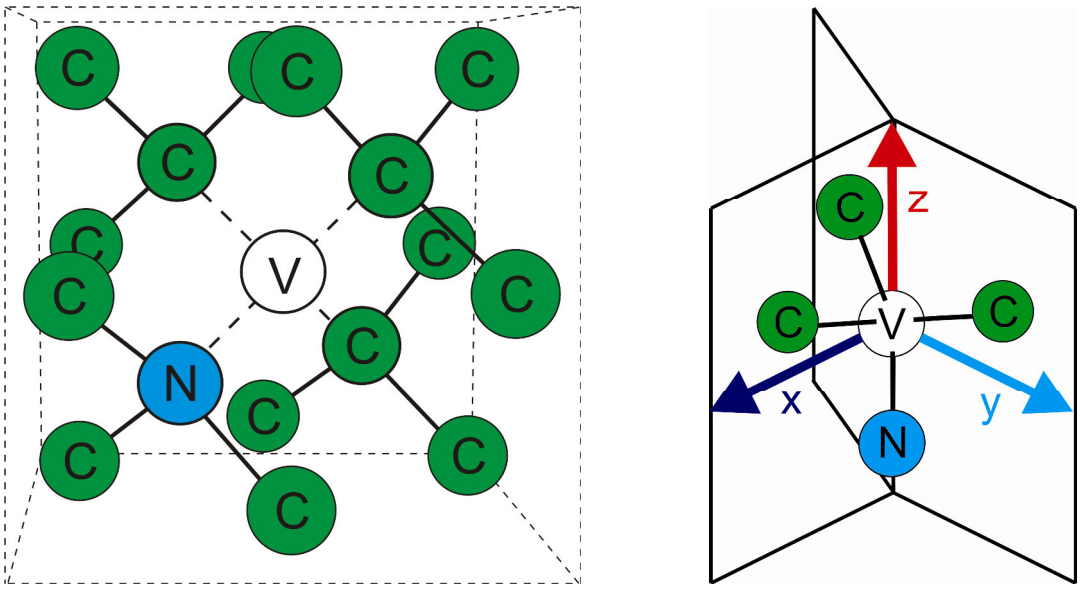

Fig. 12 Schematic drawing of the NV center defect in diamond lattice (left) and (right) the defect structure of an NV center major trigonal symmetry along axis z, also its reflection planes and one definitions of its minor symmetry axis x.

The NV^- center has a ground state |g> at the $^3A_2$ level and an excited state |e> at the ^3E level.[46] The main transition between ground and exited states has a wavelength of 638 nm (zero phonon line - ZPL) and can be excited by light with a wavelength below 640 nm. Figure 13 shows typical photoluminescence spectrum when excited with a green laser at of

wavelength 532 nm, revealing both NV^0 and NV^- related peaks. As long as only a few percent of the photons emitted directly into ZPL, most luminescence will be reflected in vibrational side bands between 600 and 800 nm.

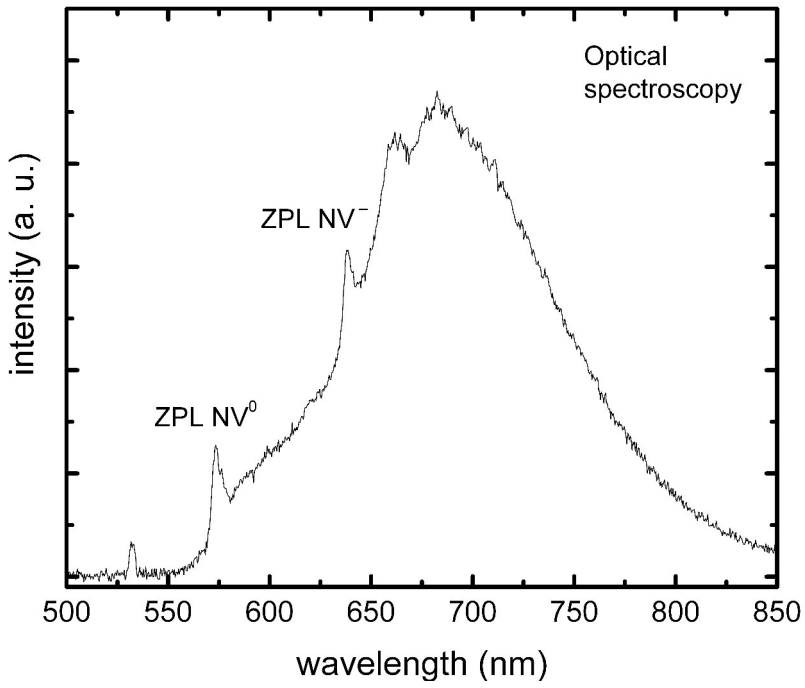

Fig. 13 Typical photoluminescence spectrum revealing NV^0 ZPL and NV^- ZPL.

The ground |g> and exited |e> states split into three spin sub-levels, with spin triplet symmetry. The ground state has a zero-field splitting between the $m_s = 0$ and the $m_s = \pm 1$ spin sublevels, m_s here indicating the quantum number of the spin sublevel along NV center symmetry axis [47]. Due to the axial symmetry of the NV center $m_s = \pm 1$ states will be degenerated and $m_s = 0$ state will be energetically lower. The energy-level diagram of the NV center is shown in the Fig. 14. For the $^3A_2$ states require D = 2.87 GHz splitting energy due to the spin-spin interaction origin from the electron charge distribution related to high localization around each of three carbon atoms [48]. Here D refers to the zero-field splitting. The energy difference for ^3E states between spin sublevels at RT is equal to D = 1.42 GHz [48]. The spin-lattice relaxation time refers to the so-called T1 value of a few milliseconds at RT and is related to the transition rate between $m_s = 0$ and $m_s = \pm 1$ sublevels. A magnetic field destroys the degeneracy between $m_s = 0$ and $m_s = \pm 1$ and causes the $m_s = \pm 1$ levels to shift. This is the fundamental effect for all possible magnetic sensing applications of diamond NV centers. The spin state is preserved by optical transitions while cycling between ground and exited states. The metastable singlet state |s> plays a paramount role, because the system either decays via fluorescence emission or non-radiatively via inter-system-crossing to a metastable state, depending on the fluorescence emission quantum yield. At the same time, the percentage of excited electrons that decay via the radiative triplet-triplet transition define the quantum yield, and is spin state dependent. This spin-dependent luminescence is used to perform electron paramagnetic resonance (EPR) measurements on a single electron spin.

Further, the optically detected magnetic resonance (ODMR) effect is a common method used with NV centers, that allows precisely determine the orientation of the defect. The use of the ODMR technique allows tracking the fluorescence intensity related to the excitation transition from ground to excited state upon light illumination, when the microwave frequency resonant with the EPR transition is applied to the ground state.[4, 49]

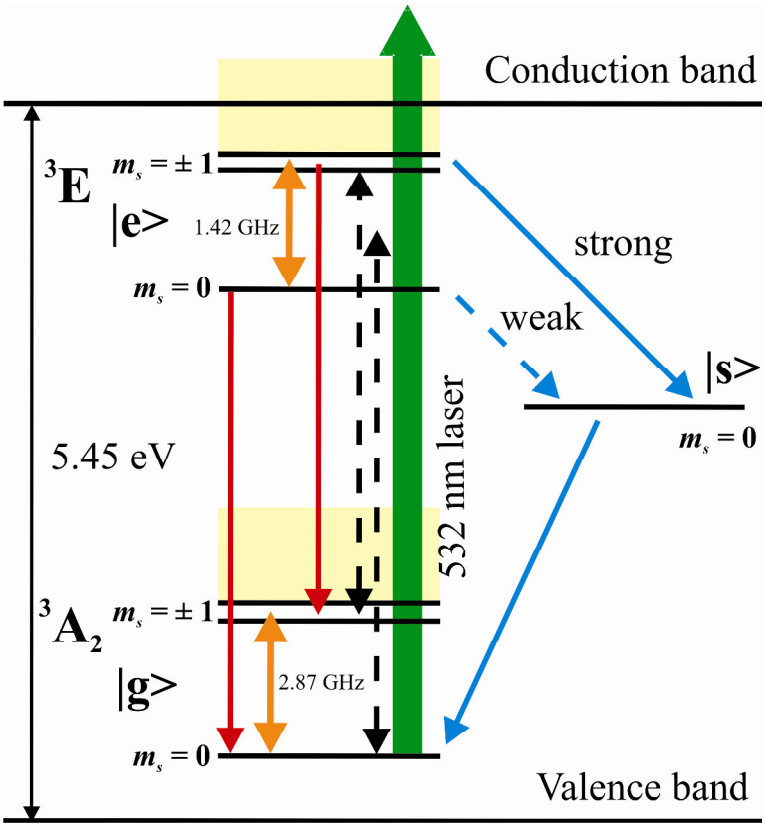

Fig. 14 Level diagram showing spin-triplet ground and excited states for NV^- center, including optical pumping via 532 nm laser (green arrow), ZPL transition at 637 nm (red arrow), phonon sideband (yellow), (black dashed line) indicate the radiative transition, and (blue solid and dashed lines) presents strong and weak non-radiative decay via the meta-stable |s> singlet state.

Therefore, employing the ODMR technique together with confocal microscopy one can detect and control a single NV center. The implementation of such measurements has been already demonstrated in the literature.[50]

Chapter III

3. Principles and experimental techniques

3.1. Instrumentation

Figure 15 shows the UHV spectroscopy system that consists of three parts a main measurements chamber, a plasma source chamber and a transfer chamber. The main chamber has a base pressure below $5 \cdot 10^{-11}$ mbar maintained by a 500 l/s turbo molecular pump (TMP) HiPace 700 (Pfeiffer Vacuum GmbH, Asslar, Germany), two liquid nitrogen cold traps, a Ti sublimation pump and a sorption getter pump CapaciTorr D400-2 (SAES Getters S.p.A., Milan, Italy). It is equipped with a hemispherical energy electron analyser PHOIBOS 100 (Specs GmbH, Berlin, Germany) supplied with a five channel MCD detector, an X-ray source XR 50 (SPECS Surface Nano Analysis GmbH, Berlin, Germany), evaporators, sample holder manipulator and sample holder. The sample holder manipulator allows sample positioning in the x, y and z directions as well as 360° rotation. The main chamber is also supplied with magnetic shielding.

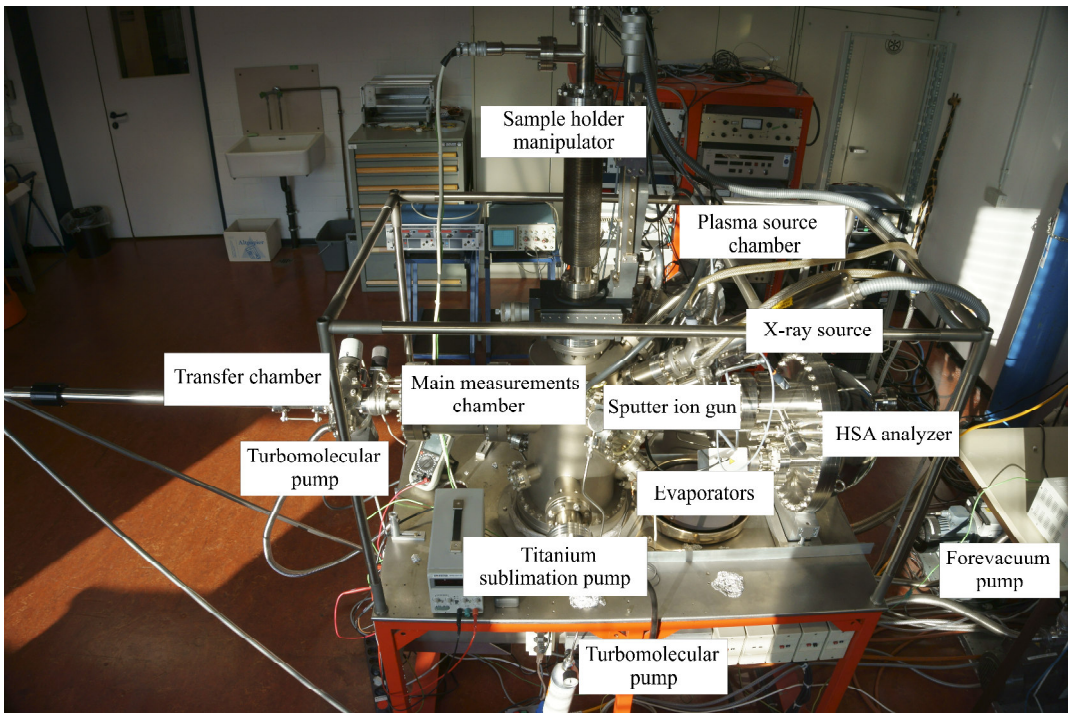

Fig. 15 UHV spectroscopy chamber with corresponding instrumentation.

A transfer chamber with a base pressure of 1×10^{-9} mbar is equipped with a transfer-manipulator pumped by small TMP TURBOVAC 50 (Oerlikon Leybold Vacuum, Cologne,

Germany) and a rotary roughing pump. This chamber is used for fast sample exchange and is separated by a mechanical UHV gate valve from the main measurement chamber.

The plasma chamber with a base pressure $1x10^{-9}$ mbar is pumped by a two TMPs, a 500 l/s turbo molecular pump TMU 521P (Pfeiffer Vacuum GmbH, Asslar, Germany) and a 33 l/s TURBOVAC 50 (Oerlikon Leybold Vacuum, Cologne, Germany) pump located at the buffer chamber.

The plasma chamber contains a dual discharge source for UPS and MIES. This is a homemade source that is used to produce UV photons 21.2 eV (He I) and 40.8 eV (He II), and the main purpose of this source is to produce metastable helium atoms He*(2^1S) of energy 19.82 eV. More details on the plasma source construction, performance capabilities and MIES technique itself are presented in the results section. Fig. 16 shows a photo of the plasma chamber.

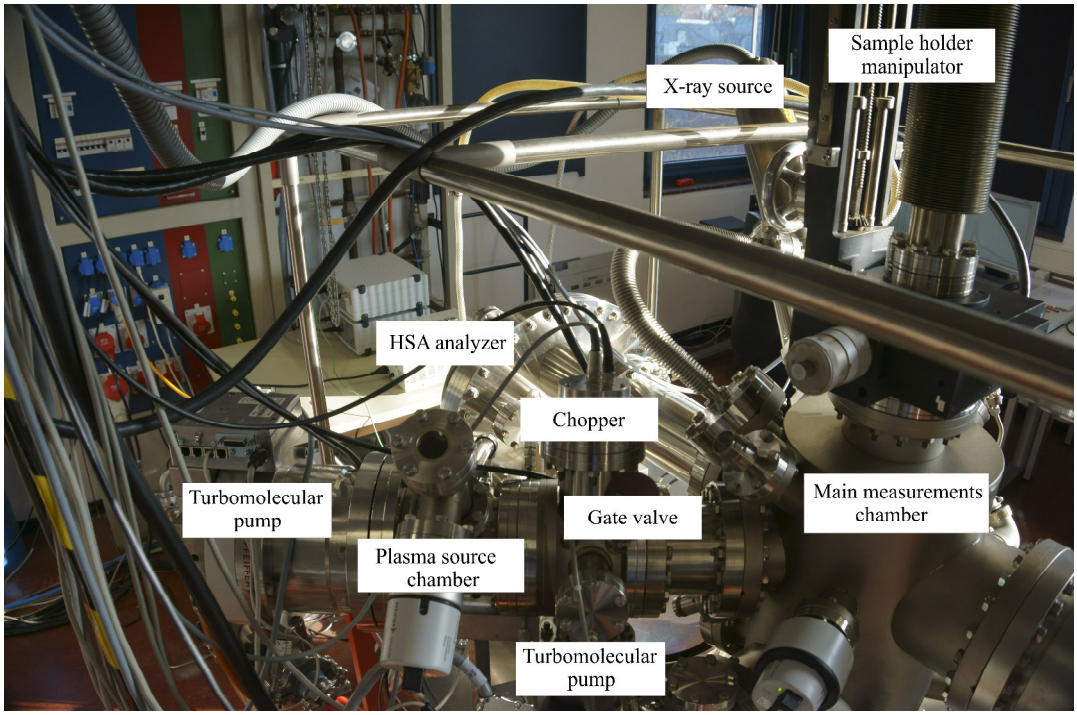

Fig.16 Photo of a plasma chamber.

A homemade sample holder construction vacuum part is shown in the Fig. 17, it provides space for two samples and equipped with a heater, as well as two K-type thermocouple connections. A sample holder plate made from stainless steel has an Omicron compatible design to be able to transfer samples to NC-AFM systems.

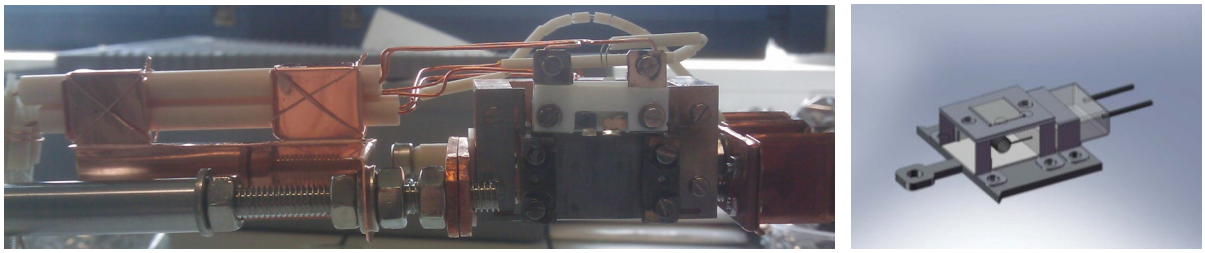

Fig. 17 Photos of sample holder construction vacuum part (left) and a removable sample holder plate (right) with heating option and K- type thermocouple.

The sample holder plate has an additional construction for electron bombardment heating up to a 900° C and a K-type thermocouple attached near the sample position.

Due to some special measurement options and features, it is important to discuss the geometry arrangement in the chamber schematically shown in Fig. 18.

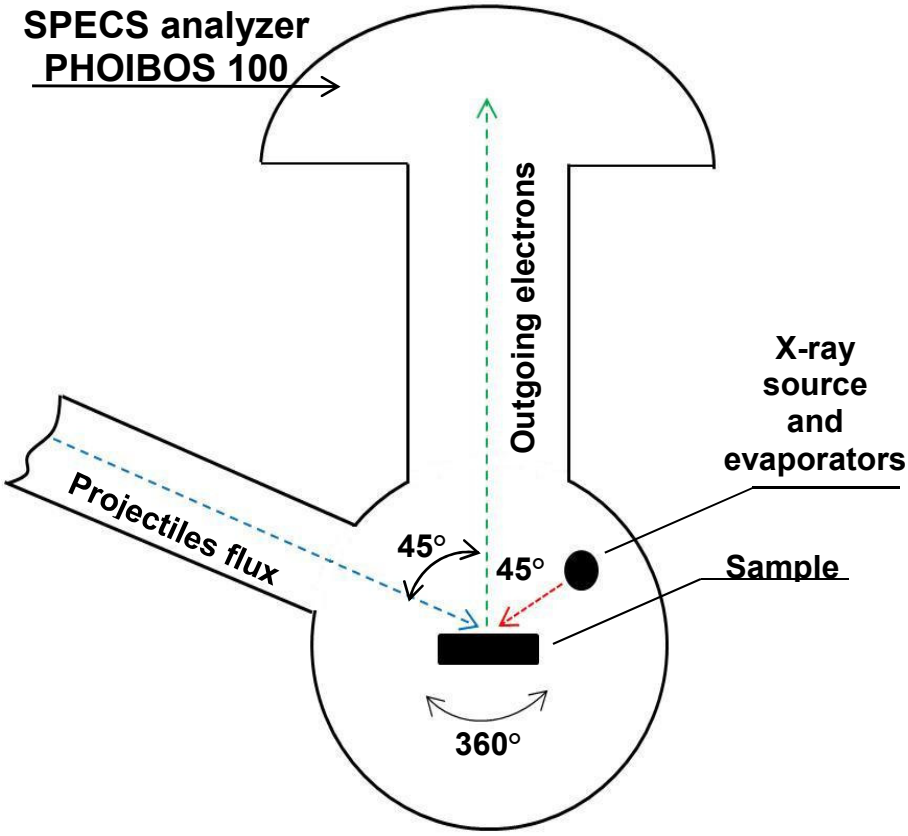

Fig. 18 Geometries of measurements, sample position and installed instrumentation.

Usually, the sample is positioned under 90° towards the HAS analyzer. UV photons and He* projectiles from the plasma source impinge on the sample under 45° angle. The X-ray source and evaporators are mounted also under 45° from the other side. The sample holder allows sample positioning in x, y and z directions and precise 360° rotation, therefore, angle resolved XPS could be recorded.

3.2. Hemispherical energy analyzer (HSA)

The main part of the spectroscopy setup is an energy analyzer used for all spectroscopy measurements regardless the excitation. The spectroscopy chamber is equipped with a SPECS PHOIBOS 100 hemispherical energy analyzer (HSA) providing high energy resolution. This model has a 180° hemisphere with a radius of 100 mm and is supplied with a five Channel Electron Multiplier (CEM) detector also called as a Multi-channel detector (MCD) for single particle detection. To avoid particle collision and deflection and to achieve good energy resolution UHV vacuum conditions and proper magnetic shielding are required.

A simplified scheme of the analyzer is presented in Fig. 19. It consists of inner and outer hemispheres that are actually two concentric hemispherical electrodes kept at proper voltages.

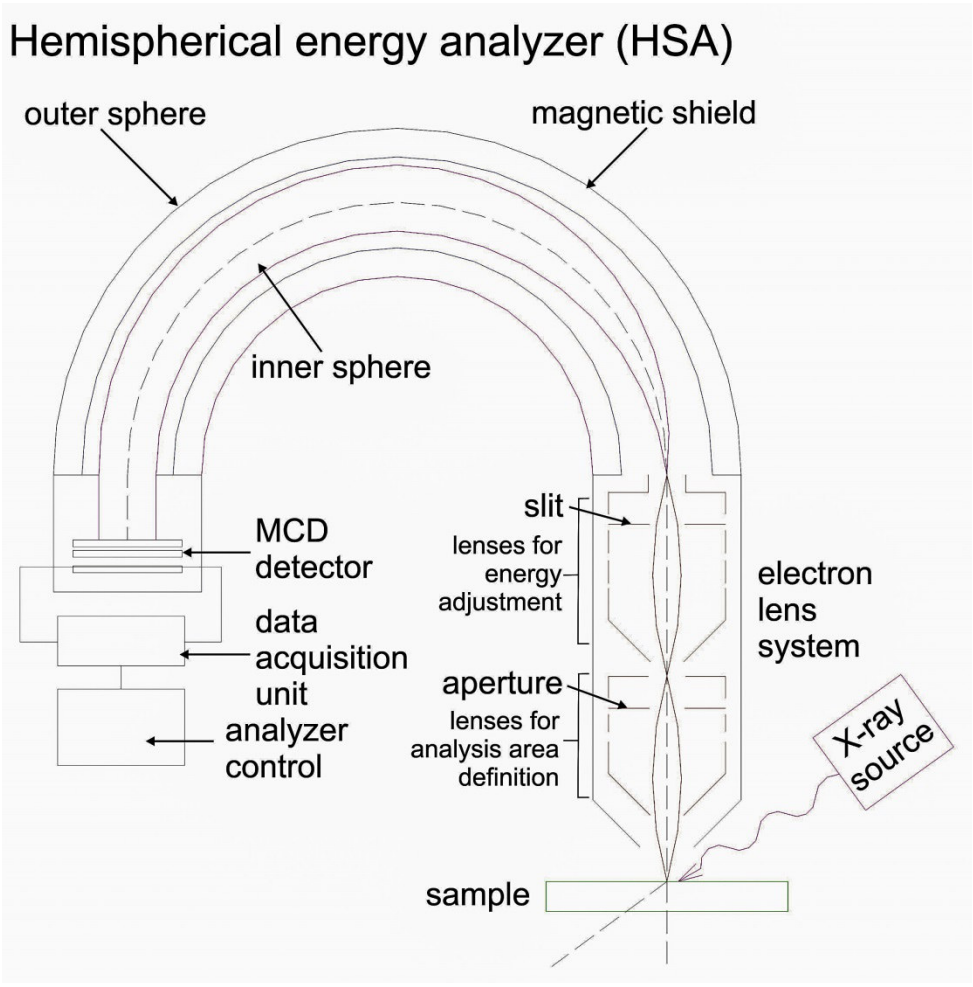

Fig. 19 Simplified scheme of the hemispherical energy analyzer (HAS).

Electrons resulting from excitation by the source (here X-ray photons) are collected by the analyzer electron optics, consisting from a set of electrostatic or magnetic lenses. The optics is a grid-free construction and can be divided into the lenses that are responsible for sampling area definition and lenses performing a function for the electrons energy adjustment. The electron optic column can also be equipped with an adjustable size aperture and an entrance

slit. Electron optics and apertures serve for collection, transferring and energy spreading, however, they also play an important role for operating the system in different analyzer modes and to perform angular and spatially resolved studies. These analyzer operation modes are specified by the lens stage for the certain electron collection angles and areas, depending on parameters applied for lenses and selected aperture configurations. After passing the electron optic system and the entrance slit, electrons are subjected to the electrostatic field in the analyzer hemisphere allowing them to pass if they have the right energy called the pass energy. Only electrons having the pass energy E_{pass} will follow the central trajectory (dashed line), the hemispheres and reach the MCD detector. Electrons having higher kinetic energy will be pointed outside and electrons with lower energy will be directed inside in the hemisphere exit plane. This allows the simultaneous spectra recording in the range of energies around the nominal pass energy by utilization of the MCD detector. The MCD detector that is an array of five channeltrons arranged parallel close to each other, where each channel equipped with a separate preamplifier attached outside of the setup vacuum part. The number of incoming particles to each channel is recorded separately, subsequently stored and processed by the data acquisition unit. Summing up the particles with the same kinetic energy collected by each channel reveals the total electron flux for each kinetic energy.

There are two main modes for analyzer and lens system operation, these are the fixed analyzer transmission (FAT) or the constant analyzer energy (CAE), and the fix retard ratio (FRR) mode also referred to as the constant retard ratio (CRR). In the FAT mode, the pass energy is kept constant and it depends totally on the transfer lens system to retard the electrons kinetic energy in the analyzer preset range. In the FAT mode, the signals of all particles is independent of their kinetic energy E_K and will be recorded with the same energy resolution, where intensity drops with the kinetic energy:

$$I = \frac{1}{E_K}$$

In the FRR mode, the retardation ratio R follows the following formula:

$$R = \frac{E_K}{E_{pass}}$$

In this mode all electrons will be decelerated with this same fixed factor, so that the pass energy will be proportional to the kinetic energy and the intensity rises with E_K.

For Auger electron spectroscopy (AES) the FRR mode is mostly used and it is suitable for recording a survey spectrum. The FAT mode is suggested to be used for XPS and UPS, but generally both FAT and FRR modes are applicable for XPS, UPS and MIES surface spectroscopy an their choice depends on sample peculiarities. An additional lens could be operated in a three main modes. First is the spatially resolved divided into high, medium and low magnification modes. Second is the transmission optimized divided into large, medium and small modes. Third is the angular resolved mode divided into high angular dispersion,

medium angular dispersion, low angular dispersion and wide angle modes. The spatially resolved mode depending on the aperture configuration allows one to perform spatially resolved studies by the adjustment of the maximum particles collecting angle. In the transmission optimized mode the angular resolution is accomplished changing the iris aperture size, which is located in the diffraction plane; this mode offers higher angular acceptance, but the spatial resolution is worse. The angular resolved mode allows one to adjust the angular resolution down to ± 0.05 ° and makes it the perfect mode for angular dependent studies. Utilization of the iris slits allows one to achieve very high spatial resolution with a collection spot of about 0.5 x 0.5 mm, however, the intensity will drop dramatically.

3.3. X-ray photoelectron spectroscopy (XPS)

X-ray photoelectron spectroscopy has been developed by Kai Siegbahn in Uppsala, Sweden. This became possible after an important discovery of a photoelectric effect by Heinrich Rudolf Hertz in 1887.[51] Later in 1905 it has been explained by Elbert Einstein.[52] This gave a strong impulse and leads to start of research in this field and further technique development. In 1954 Kai Siegbahn has improved significantly his equipment, what enabled him to record sodium chloride (NaCl) spectra a year later. Some of the spectra measured by Kai Siegbahn even nowadays look impressive. In 1981 Kai Siegbahn was awarded the Nobel Prize for his great contribution to the XPS technique development and his research in this field.[53] The Siegbahn's group introduced other abbreviation for XPS namely the Electron Spectroscopy for Chemical Analysis (ESCA).

The XPS is used extensively as a tool for investigation of the chemical composition in a sampling depth region, related to projected photoelectrons energy. The XPS technique allows to measure core shell levels of atoms, having atomic number greater that Z=2, for instance Lithium (Z=3) and higher. It is not possible to measure Hydrogen (Z=1) and Helium (Z=2), due to their exceedingly low photoelectron cross sections and the fact that XPS is optimized for investigation of core electrons. Detection limit of the XPS lies between 0.1 – 1 At%, depending on the element atomic number.

The XPS is based on the photoelectric effect, means that material exposed to a photon flux of certain energy causes photoelectron emission, e.g. ejection of photoelectrons. Most X-ray photons have wavelength in the range of 0.01 – 10 nm and energy of 100 keV – 100 eV. Simplified schematic one-electron model interpretation of the photoelectron effect for semiconductor material is shown in Fig. 20. After the photoelectron effect, atom will release energy by the emission of Auger electron. The electron from L level falls to the empty core level to fill the vacancy and in order to conserve the released energy KLL Auger electron is emitted (Fig.20).

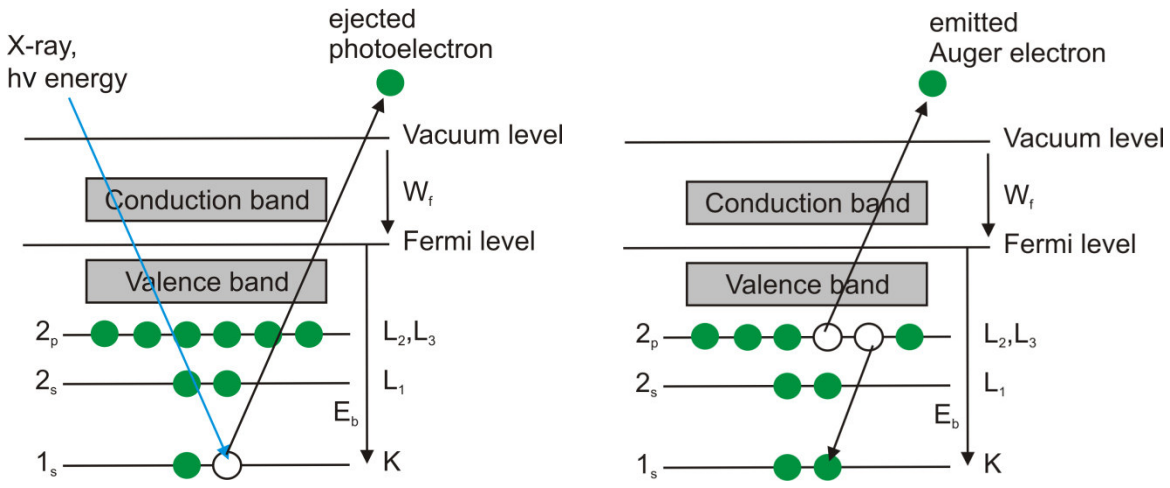

Fig. 20 Simplified drawing of the photoelectric effect (left) and a subsequent Auger process (right).

The kinetic energy (E_K) of the emitted electrons measured by analyzer and the binding energy (E_B) for core shell energy level by Einstein relationship follows the formula:

$$E_K = h\upsilon - (E_B + W_f)$$

where $h\upsilon$ is the photon X-ray energy and W_f is a work function. The difference in energy between the ionized and neutral atom state is called the binding energy (E_B), and the W_f of a material is the energy difference between the Fermi level (E_F) and the vacuum level.

Figure 21 shows an example of a typical XPS survey spectrum obtained from an Au (111) on glass. Using an electron analyzer it is possible to measure the number of electrons ejected at various E_B (E_K) energies, reveals the photoelectron spectrum, showing all the accessible energy levels (Fig. 21). The electron signal collected by XPS instrumentation includes contribution from photoelectron and Auger electron lines. Kinetic energy E_K is independent of the X-ray photon energy. However Auger peak positions, in the E_B scale, depend on the X-ray source energy.

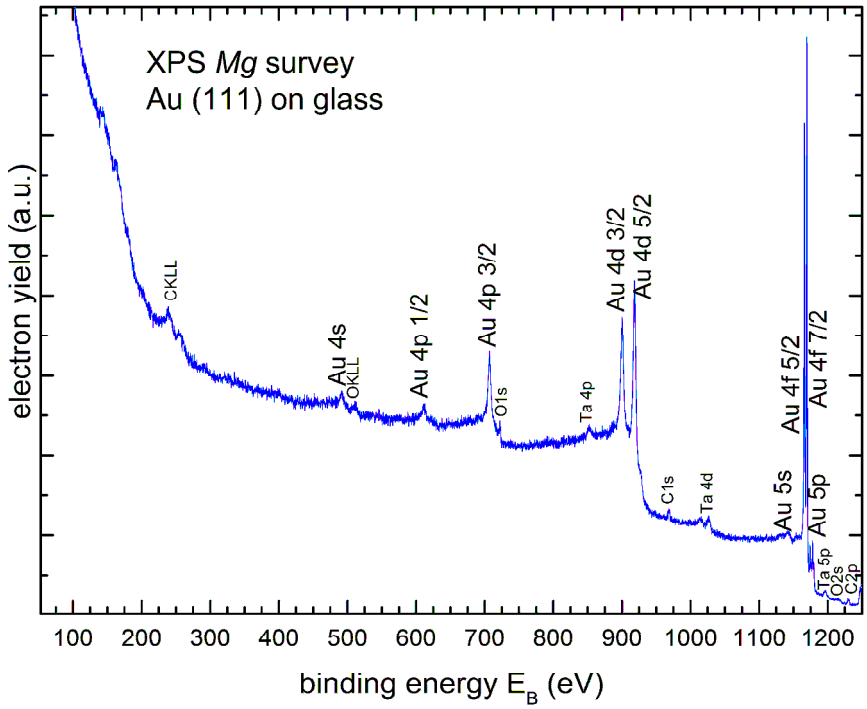

Fig. 21 Example of a typical XPS survey spectrum obtained from the Au (111) on glass.

Due to strong electron interaction with a matter, which leads to plasmon excitation, vibrational excitation and electron-hole pair formation, only electron from the near surface region could escape from the sample without energy loss. The inelastic mean free path shows how far an electron can travel through a matter before losing energy. Graph obtained by L.C. Feldman for the electron inelastic mean free path in Å versus electron energy for surface sensitivity in XPS is shown in Fig. 22.[54] In lab non-monochromatic XPS source with typical anodes Al Kα and Mg Kα corresponding to energy of 1486.6 eV and 1253.6 eV is used. The mean free path for ejected electrons for our system is about 2 – 3 nm.

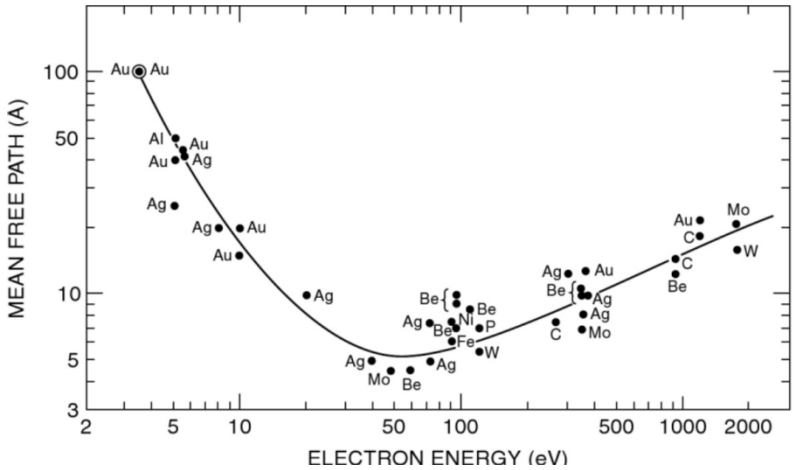

Fig. 22 Electron inelastic mean free path in Å versus electron energy.[54]

Figure 23 represents drawing of the photoemission spectrum with subtracted background correspondence of the band levels and the Fermi level. Under the X-ray exposure electrons from the solid filled states related to a certain kinetic energy are excited. The particular emitted electrons intensities and energies will form the photoemission spectra, which reflect the distribution of the filled levels in the sample. Tabula data of photoelectron and Auger peak energy values, can be obtained in the XPS reference books or online databases.[54, 55]

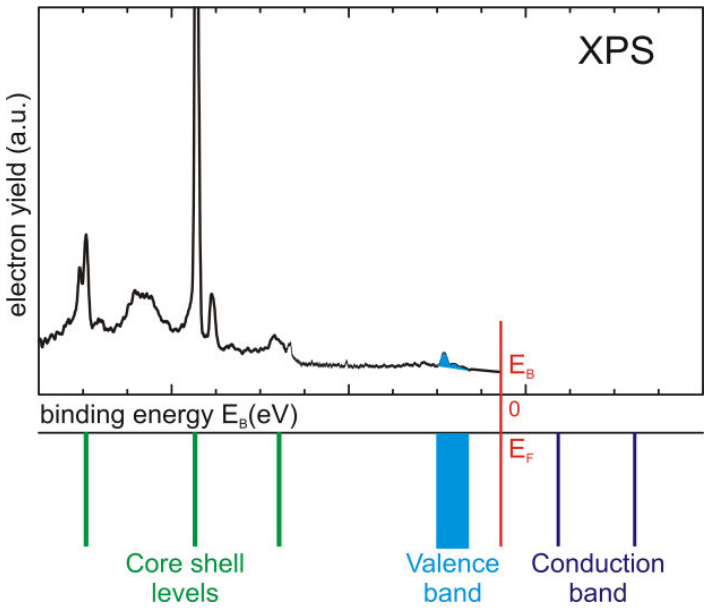

Fig. 23 XPS correspondence to the band levels and Fermi level.

It is important to note that the E_B of energy levels in solids are measured conventionally with respect to the Fermi-level (E_F) of the solid, rather than the vacuum level (Fig. 24).

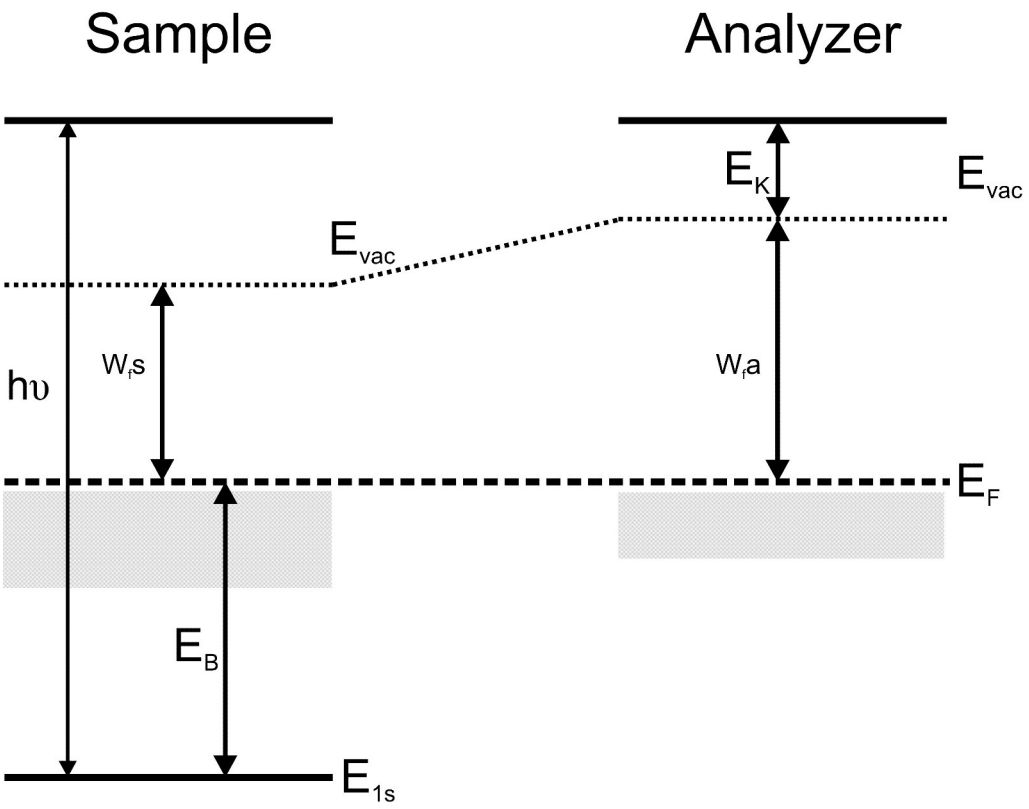

Fig. 24 The sample and the spectrometer (analyzer) levels alignment diagram.

The sample and the spectrometer (analyzer) are electrically grounded and their Fermi levels are aligned (see Fig. 24). The analyzer work function ($W_f a$) is known and provided by the manufacture, and is different from the sample work function ($W_f s$). For the photoelectron binding energy the Fermi level (E_F) is the reference point, explicitly E_F will be a zero on the binding energy scale. Nevertheless, spectrometer is expected to be calibrated regularly using standard samples (e.g. Au or Cu) in order to have accurate peak energy positions during the measurements. Detailed calibration of our analyzer is presented in the chapter 5.

The XPS is intensively used for chemical shift analysis. The chemical shift is defined as an energy difference between a photoelectron line, Auger line or Auger parameter (A.P.) for the element specific compound towards this element's pure state.

Implementation of so-called X-ray-induced Auger electron spectroscopy (XAES) offers additional analysis options for studying X-ray excited Auger peaks. Using this analysis, the Auger parameter (A.P.) [56, 57] and the D-parameter [58, 59] can be obtained.

The A.P. was applied for chemical state identification, it is defined by both the binding energy (EB) of a core electron and of an X-ray excited Auger electron, for a given chemical state. Usually the modified A.P. by Gaarenstroom and Winograd used for analysis [60], where A.P. (α') is independent of the X-ray energy and is defined by the equation:

$$\text{A.P. } (\alpha') = E_K\,(C_1C_2C_3) + E_B,$$

where E_K ($C_1C_2C_3$) is related to the E_K of the Auger process and E_B is the binding energy of the core level C.

Another tool for analysis the Auger transitions, is a so-called D-parameter, which allows to evaluate the sp^2 / sp^3 ratio content from the Auger C KLL peak. The D-parameter is revealed from the distance between the most positive maximum and most negative minimum of the C KLL peak 1st derivative.[58]

Also a powerful technique called Angle-resolved XPS (ARXPS) is extensively used for the top surface depth profiling in the nm range. In this work, ARXPS technique is used only for test measurements, therefore details of the technique are skipped.

The main XPS technique capabilities[55, 61, 62] are summarized below:

• Quantitative surface analysis

• Detection limit 0.1 – 1 at. %

• Sampling depth top 0 – 10 nm

• Detection of periodic table elements excluding H and He

• Chemical state information from peak shifts

• Chemical or electronic state of each element in the surface

- oxidation state of the surface

- bonding information of surface adsorbed species

• Mapping or line profiling (uniformity of elemental composition across the top surface)

• Depth profiling (uniformity of elemental composition within sample depth)

• Easy to utilize, required only slight sample preparation

3.4. Ultraviolet photoelectron spectroscopy (UPS)

The use of the ultraviolet radiation in photoelectron studies has been proposed and developed by two research groups. First is by Prof. A.N. Terenin group from St. Petersburg in 1961 [63] and second by Prof. D. W. Turner group from the Imperial College of London University in the 1963 [64]. The group of Prof. Turner first introduced the use of helium gas discharge providing HeI resonance line of photoelectrons energy at 21.2 eV (584 Å) using differential pumping system. Later in 1970 at the King's College in London Prof. W.C. Price group introduced the use HeII resonance line [65] for photoelectron studies providing energy of 40.81 eV (304 Å), that allowed to perform the inner valence orbitals ionization [66].

Due to the fact that using of the XPS (which is certainly used extensively) for evaluation of the states in the VB region takes much more time, the UPS would be much better choice for this task. In the XPS photoionization cross section for the valence photoelectrons is about one order of magnitude lower than that for the core photoelectrons. In the XPS states near VB edge are quite weak.

For UPS measurement photons generated by homebuilt plasma source (for more details of source technical parameters please see Chapter 4. 1.), providing emission energy of 21.2 eV obtained by HeI resonance line, has been used.

Photoemission process has been described in the previous XPS section. Because of the much lower energy only photoelectrons from the VB will be emitted into the vacuum and collected subsequently by electron analyzer optics (Fig. 25).

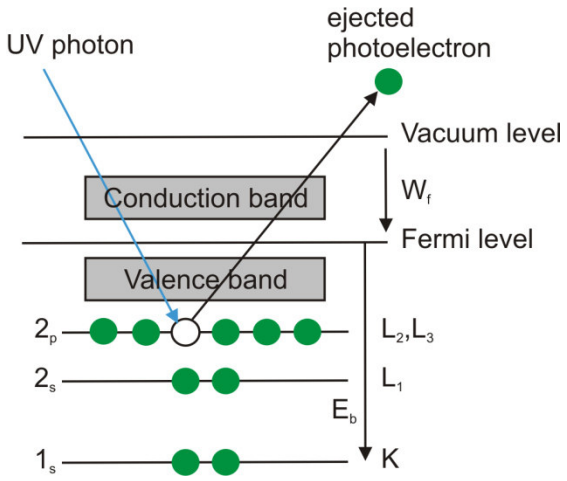

Fig. 25 Shows basic diagram of the photoelectron effect occurring by means of the ultraviolet irradiation.

UPS spectroscopy by means of the certain energy photon beam irradiation will provide information of the ejected valance electrons, estimates electronic density of states in the VB, frontier orbital energies for HOMO (highest occupied molecular orbital) and the work function values for escaping into the vacuum electrons.

The diagram below for energy density of states (DOS) shows the difference between XPS and UPS in the VB (Fig. 26). Assume that the sample will have DOS similar to what is shown on the left side of the figure 26. In the XPS photoelectrons will be excited from the occupied VB into a flat continuum of the final states higher than the X-ray photon energy (e.g. 1253.6 eV in case of Mg anode), so that the spectra will reflects occupied states in the VB. However in the UPS, due to the much lower energy photons will excite the photoelectrons into the final states much more closer to the E_F, and the subsequent spectra will denotes a convolution of the both occupied and unoccupied states in the VB of the characterized sample.

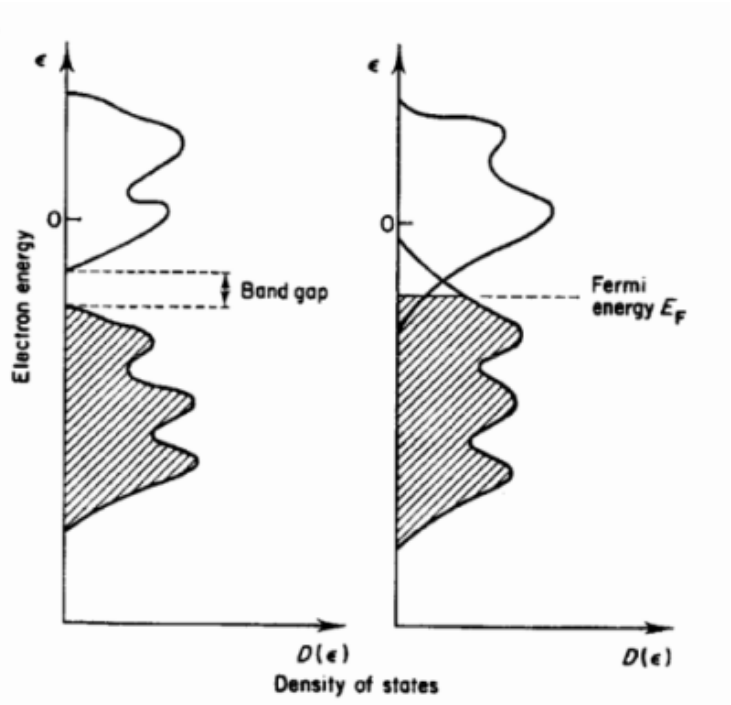

Fig. 26 The comparison of XPS vs. UPS energy DOS diagram by A.F. Orchard [62].

The Fig. 27 demonstrates in diagram form how does the electron density of states relate to the recorded UPS spectra. This diagram illustrates the correspondence between the DOS of entirely filled electron states in the solid sample and the photoemission spectra electron yield. Peaks of the elastic photoelectrons are overlaid by the background signal formed by the secondary inelastically scattered electrons[66].

A typical UPS spectrum of Au film on glass is presented in the Fig. 28. The spectrum is obtained by scanning the E_K range and plotting the number of the ejected electrons presenting counts per second versus E_K. This scale is usually marked as count rate relative energy, in this work for spectrums abbreviation electron yield / a.u. (arbitrary units) has been used. This designation is very important due to the complexity in the absolute count rate estimation due to the number of complex experimental variables related to different instrumentation design, parameters and sample type.

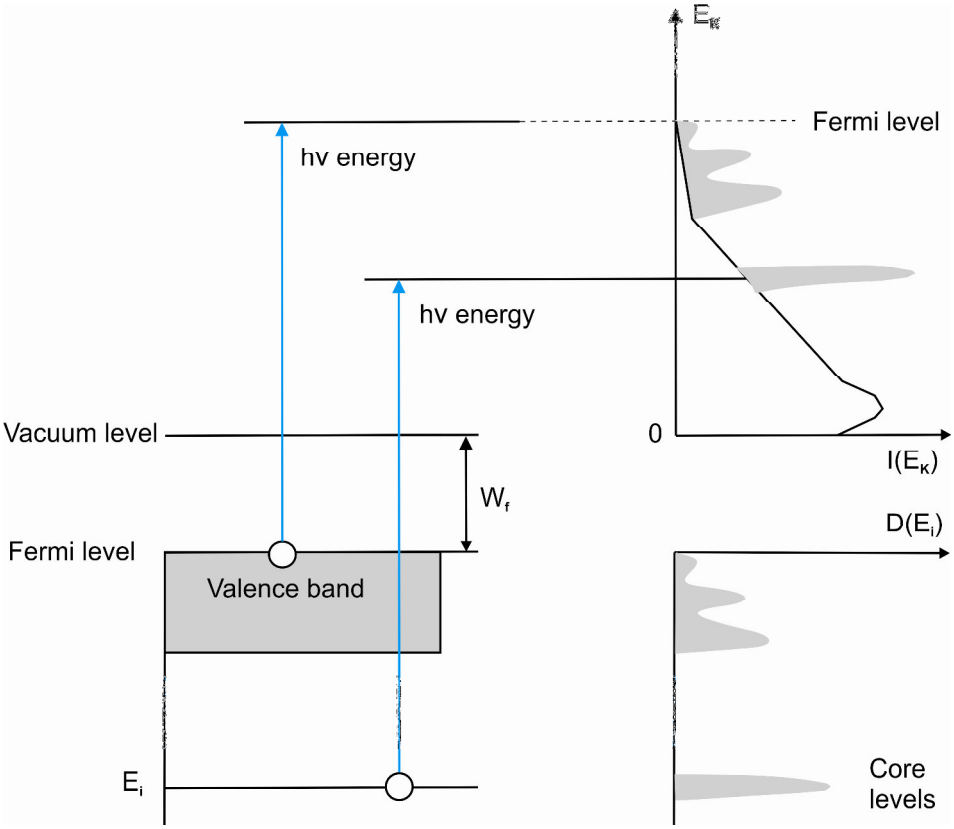

Fig. 27 Relation between DOS in the VB and the recorded spectra.

However the relative intensities could be meaningful and correlated to the relative photoionization probabilities to different states of the surface atoms, what is actually a relative differential photoionization cross section. The x-scale of the UPS spectra usually refers to the ionization energy marked as kinetic energy or binding energy in the electron volt (eV). The E_K values obtained during the measurements could be converted into E_B using Einstein's relation for the photoelectric effect (see XPS chapter 3.3). The inelastically scattered electrons will still have enough energy to escape into the vacuum and will be detected as secondary electrons and will form the background signal. In the Fig. 28 a blue marked area belongs to the secondary electrons.

The main features of the UPS spectra are emission edge, Fermi energy position, work function and DOS. The emission edge will usually introduced as a zone near the UV source energy cut-off, in Fig. 28 this is dashed tangent line to secondary electrons peak, and will reflect the energy limit of the electron excitation. Apparently the UV source cannot excite electrons at energy levels above its own energy. The E_F is the last possible energy state for an emitted electrons collected by the analyzer optics. The E_F level could be changed according to the sample temperature and/or the type of the bonding between atoms and surface adsorbates. The work function is the energy that must be overcomed to emit electrons from sample into the vacuum in order to be gathered by the electron analyzer. The work function value is the difference between UV photons energy and the photoelectron spectrum width from E_F to the

secondary electrons cut-off. The electron will not be emitted in the vacuum and will not be reflected on the spectra, if the electron E_K is below the W_f.

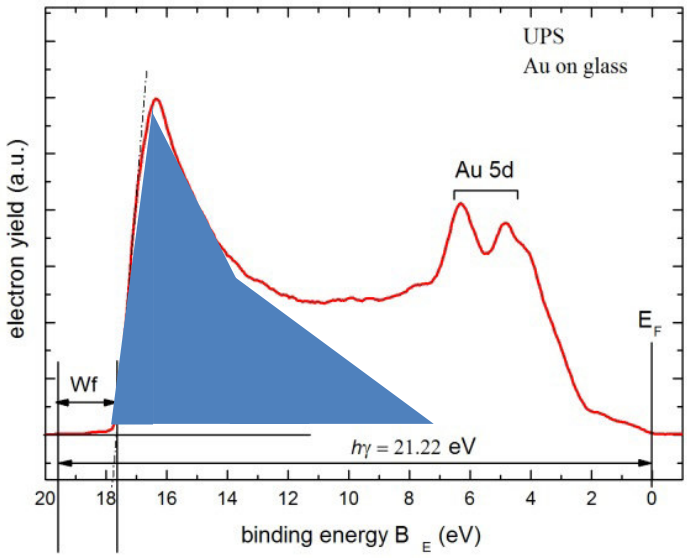

Fig. 28 Typical UPS spectra of Au (111) on glass, blue marked area shows schematically secondary electrons signal.

During the measurements the projectiles in UPS/MIES measurements impinge on the sample under angles to its surface 45° respectively. Electrons emitted from the surface are collected perpendicular to the surface. To precisely resolve the low-energy cut-off in the electron spectra and to avoid possible irregularities of the analyzer transmission function for electrons with low kinetic energies in valence band spectra (UPS/MIES), the sample is biased by 15.00 V. For all such spectra, the kinetic energy scale is corrected for this bias voltage and also for the analyzer work function, so that the low energy cut-off energy E_F directly yields the sample work function W_f. The cut-off energy E_F is determined from electron emission spectra by linearly extrapolating the yield curve and determining the point of intersection with the zero yield axes.

In order to overcome possible negative charging effect sample could be rather heated to increase surface conductivity or electron gun operated at low energy could be utilized.

The Metastable Impact Electron Spectroscopy (MIES) is also used for surface studies in this work. It is introduced in the chapter 4.1, where MIES surface spectroscopy technique principles and instrumentation design are illustrated by measurement examples on diamond and TiO_2 surface.

3.5. Confocal fluorescence microscopy and optically detected magnetic resonance (ODMR)

In order to detect NV^- in diamond samples confocal microscope system by our collaborate partners from the Mainz University has been used.

Confocal microscope is an optical imaging technique with main advantages of the increased contrast and optical resolution. It is a scanning microscope, where sample is scanned by the focused laser beam and an image will be build point by point. The fundamental difference comparing to standard optical microscope is a use of confocal aperture or pinhole situated in the front of the confocal detector. Thanks to the use of such a confocal detector aperture the confocal microscope gained its name. Use of this pinhole restricts the illumination of the entire field of view at once. Fig. 29 shows the principal scheme of the confocal microscope proposed and patented by in 1957 by Marvin Minsky.[67]

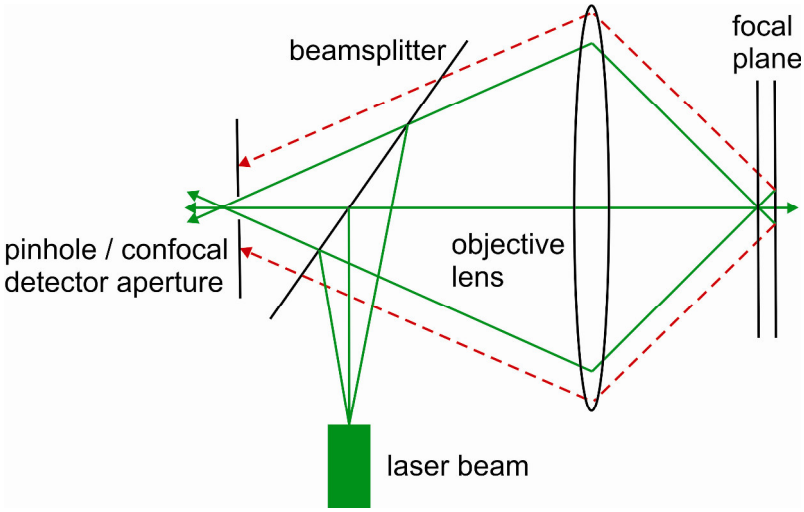

Fig. 29 The principal scheme of the confocal microscope.

Laser is a perfect source for confocal microscope, it provides high focusing and high light power could be achieved in one small point. Objective lens is used to focus the laser beam on the sample. The reflected beam from the focal plane or the fluorescence signal from the certain spot of the sample will be than again by the objective lens towards the detector pinhole. The beam path in Fig. 29 is drawn in green, red dotted lines reproduce the light outside the focal plane, which will be smeared over a wide area till it get into the pinhole, thus only minor amount of it goes through the aperture. This means that confocal image will consists only from the in-focus signal information. Acquiring a set of images with the different focus points allow to accumulate a full three-dimensional image of the sample. Use of the 3d rendering software provides wide range of different sample views. So that 3d imaging and surface profiling of samples significantly broaden application of the confocal microscopy for biological specimens and fluorescence investigation of NV centers in diamond probes.

However, there is also a negative effect, due to the fact that a big amount of light from sample fluorescence signal will be blocked by the pinhole, what will increase resolution, but decrease the signal intensity. Thus long sample exposure time is needed often.
The lateral (XY) resolution is comparable to the traditional optical microscopes and could be improved by the reduction of the confocal detector pinhole, but this will lead of course to the major loss of the light signal intensity. In depth resolution towards Z – axis is weaker, because it involves the square of numerical aperture (NA) comparing to the lateral resolution, where standard NA parameter used. It is important to mention that the Nyquist criterion should be fulfilled in order to obtain Rayleigh resolution a minimum of 2.3 pixels within the expected resolution must be achieved.

Of course in order to perform good quality fluorescence measurements on the NV centers much more technical advanced confocal microscope is required. In the Fig. 30 a part of the Mainz group confocal "homemade" microscope is presented. Green laser wavelength of 532 nm is used to measure NV^0 (575 nm) and NV^- (637 nm) centers fluorescence signal. Sample holder is positioned in the vacuum chamber base pressure of 1 x 10^{-3} mbar. Sample holder also equipped with RF antenna, operated by the RF amplifier, for the optically detected magnetic resonance (ODMR). Sample holding stage has additional liquid nitrogen cooling option. In order to perform sample scanning with the laser beam system equipped with the piezo-stage controller (NV40/3 CLE) that allows to perform scanning over the sample lateral area in the micrometer range. System supplied with spectrometer and two avalanche photodiode based single photon counters (SPCM-ACRH14, Perkin Elmer/Laser Components, 700 cps & 200 cps). More details about this setup could be found in the dissertation work of Dr. Yevgeniy Shapiro. [68]

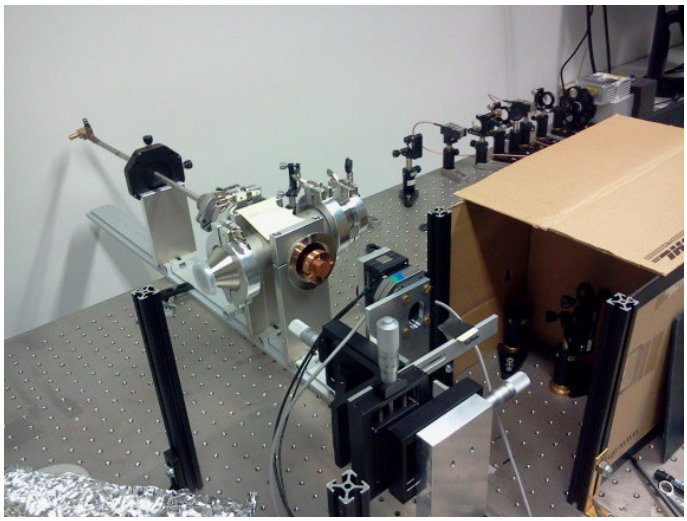

Fig. 30 Confocal microscope and ODMR setup in Mainz University.

Here are the main setup features:

- Laser beam power 10 – 500 mW
- Objective 60x magnification
- Resolution x-axis range 0.24 – 0.60 μm, z-axis 0.48-7.00 μm
- RF antenna 0.8 – 2.4 GHz

3.6. Low energy ion implantation

Ion implantation basics

Ion implantation is a versatile materials engineering tool that allow to modify and to change surface properties of different materials e.g. metals, semiconductors. This process is based on penetration of accelerated ions in to solid, at different energies, where the dose and exposition area could be precisely controlled. This is quite complicated process accompanied by different physical effects occurring between accelerated ions and the exposition material, some of them are ion scattering, surface sputtering and creation of different types of defects in the solid. The ion implantation rustic diagram is shown in the Fig. 31, this very much simplified drawing presents in general how solid is modified by means of ion implantation.

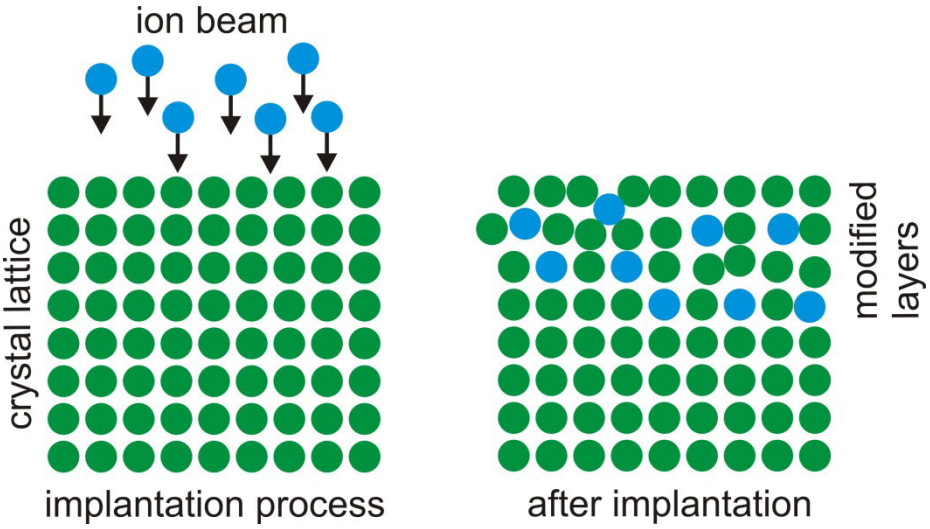

Fig. 31 Schematic diagram of the ion implantation process.

In general ion implantation could be divided into two types: low energy implantation and high energy implantation techniques. Second one belongs to the field of high energy physics and requires complex equipment like linear or cyclotron accelerators, and is beyond the scope of this work. Low energy implantation is a multipurpose and much easier accessible tool that could be established in every lab. Our project task requires shallow implantation, which asserted at low energies, e.g. higher energies leads to deeper ion penetration depth and respectively vise-versa for the low energies. That is why this technics used to be the perfect choice for our experiments.

Different type of sources could be used to generate ions. In this work is used the microwave plasma source to ionize gas molecules. In order to perform implantation ions should be accelerated towards the sample direction. This could be achieved using source acceleration optics or applying additional high voltage potential between source and the sample holder. Materials for sample mask and sample holder should be selected carefully in order to avoid contamination and charging effects leading to sample screening, resulting in ion flux deflection. Another important question is surface damage induced by ion flux. The possible

damage values could be estimated by SRIM by J. F. Ziegler (the stopping and range of ions in matter) modeling software, that allows to calculate ion's energy loss to electron, ion's energy loss to photons, production of vacancies and production of replacement collisions in the target. SRIM also allows estimate possible penetration depth and implantation in depth distribution. By implantation in the single crystal samples channeling effect should be taken into account. Our implantation setup in details is described below.

Setup for low ion implantation setup

Setup for ion implantation is presented in the Fig.32 The base pressure of the chamber is $1x10^{-9}$ mbar provided by turbo molecular pump (TMP) Leybold Turbovac TMP361 (Oerlikon Leybold Vacuum GmbH, Cologne, Germany) and the forevacuum pump Edwards E2M5 (Edwards, Crawley, UK). The setup equipped with the SPECS PCS ECR plasma source (SPECS Surface Nano Analysis GmbH, Berlin, Germany), supplied with two grid configuration, operated in hybrid mode. The source could be operated in the range of 50 - 1000 eV and has beam diameter of ~25 mm at source. The typical working distances between source and sample are from 50 to 300 mm. Nitrogen Air Liquid gas N_2 purity 99.99% (Air Liquid, Düsseldorf, Germany).

In order to be able to change distance between source and sample upon implantation, the source has been mount on the XZ manipulator system. Main parameters of the plasma source are shown below.

SPECS PCS-ECR :

- Ion energy (50 - 1000 eV)
- Beam diameter: ~25 mm at source
- Working distance: 50 - 300 mm
- Operation vacuum $1x10^{-5}$ to $1x10^{-3}$mbar
- Gas flow rate: 0.5 sccm - 50 sccm
- Working distance: 50 - 300 mm

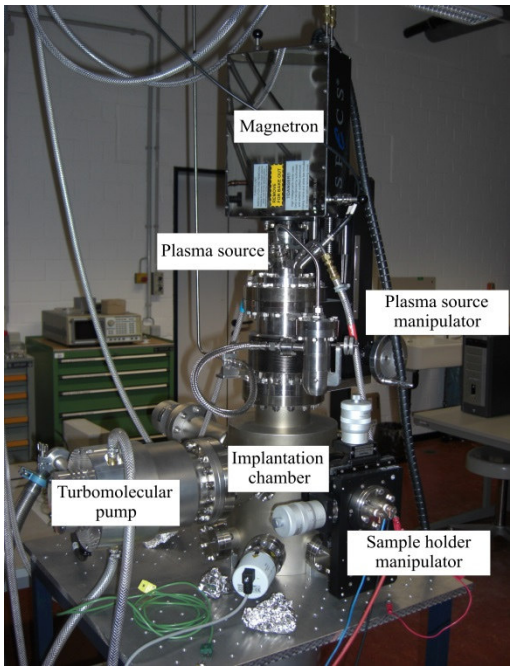

Fig. 32 Setup for ion implantation.

The main part of the source including magnetron is presented in the figure 33. It is equipped with the gas and high voltage feedthroughs. Inside top of the source installed ceramic cup, where the plasma is ignited by means of magnetron. This ceramic cup could be exchanged subject to the type of the used gas. Source could be operated with nitrogen, hydrogen and oxygen gases.

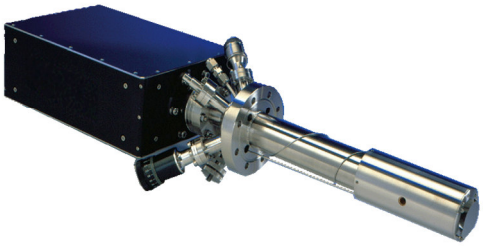

Fig. 33 SPECS PCS-ECR plasma source vacuum part and magnetron

Principal diagram of the implantation chamber is presented in the Fig. 34. The implantation chamber pump by means of the TMP and forevacuum pump, but it is supplied additionally with the Titanium pump. Gas inlet pressure could be tuned by means of the leak valve, installed directly on the gas line.

Chamber also has uninterruptible power supply (UPS) battery, that allows perform safe switch-off of the plasma source in case of power failure.

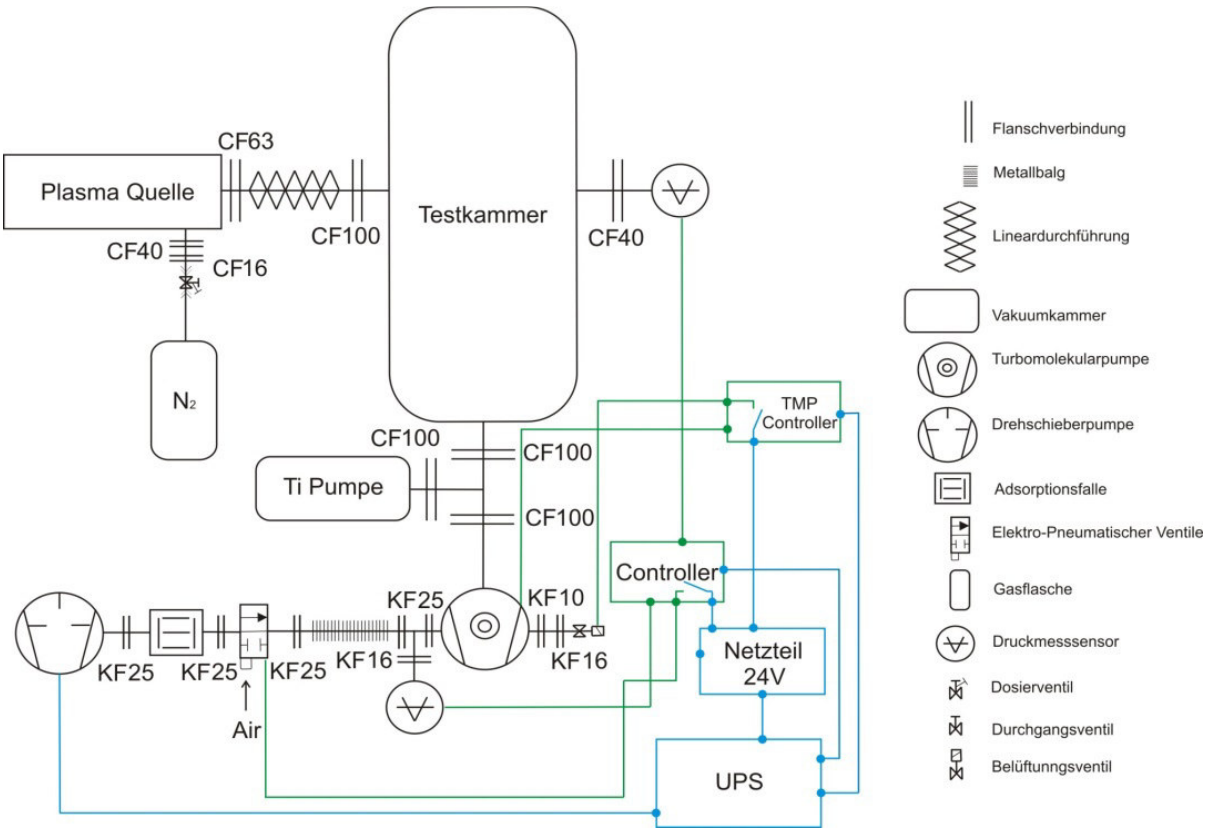

Fig. 34 Principal diagram of the implantation chamber.

Setup is also equipped with the mechanical shutter system between sample holder and implantation source in order to block the ion flux. That allows to control implantation time and as a result the implantation dose.

The main advantage for nitrogen plasma is the low ions acceleration energy that allows to perform shallow implantation, what has been the main requirement of the project tasks.

3.7. Contact angle measurements principles

Precise characterization is of a great importance for solid materials surface in the chemical, physical research as well as industrial applications. The contact angle measurement allows to quantify the wetting effect of a solid sample by a liquid. Contact angle sometimes presented under WCA – water contact angle abbreviation and labeled with Greek letter θ. Wetting effect or wettability revealed by the contact angle values of the known liquid on the solid substrate, this admits to calculate the surface free energy according to the preferred theoretical model.

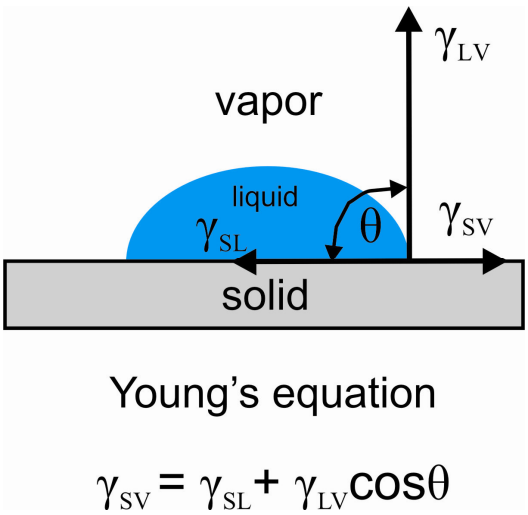

Fig. 35 Contact angle measurement principle diagram and Young's equation, where θ is contact angle, γ_{SV} is the interfacial free energy for solid-liquid, γ_{SV} free energy for the solid surface, and γ_{LV} free energy for the liquid surface.

In the Fig. 35 presented principle diagram for a contact angle measurements and the well-known Young's equation defining the balance between three contact phase of the solid, liquid and vapor. Generally contact angle define these three phase boundary geometry on the intersection of these phases.

It is important that surface free energy or critical surface tension could be estimated to perform a comparative series of measurements of different liquids and record contact angle values. This let to identify the characteristics of the solid surface and reveals the intermolecular interactions at the interface of the solid and liquid. Obtained surface free energy (or critical surface tension) could be considered as the solid substrate "surface tension", that is a characteristic parameter of the solid body likewise the surface tension parameter for a liquid.

In the Fig.36 demonstrates possible contact angle values, and the way how θ should be extracted. It is shown that low contact angle will refer to the good liquid spreading on the solid surface and vice versa high θ values are related to the poor liquid spreading. In case when the θ is less than 90° liquid wets the surface and zero contact angle denote the complete wetting effect. If the θ value is above 90°, the solid surface used to be non-wetting with the appropriate liquid.

Good surface wetting could be interpreted as the hydrophilic surface and bad surface wetting refers to hydrophobic surface.

Determination of the contact angle could be differentiated into static and dynamic angle measurements. In case when liquid droplet positioned statically on the surface and the boundary between three liquid-solid-vapor phases is not moving. In this work the contact angle evaluation refers to the static contact angle measurements.

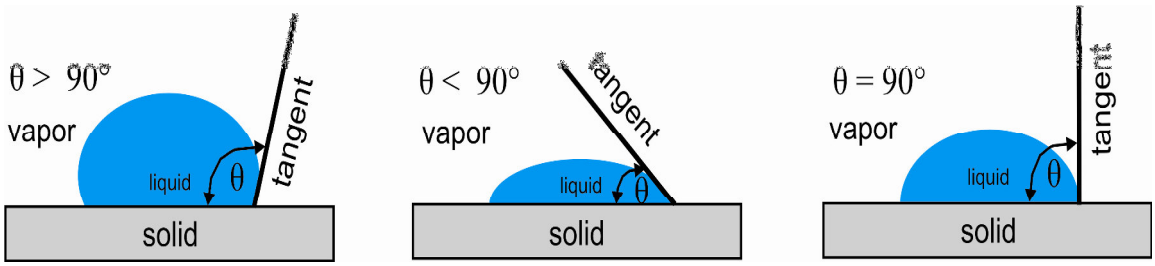

Fig. 36 Contact angle determination upon different different angle values.

The contact angle values interpretation permit to disclose solid surface physical and chemical properties, as well as their qualitative values. The high contact angle is attributed to the hydrophobic surface, reveling poor adhesiveness and poor wettability, and indicating low free energy of the solid surface. Similarly the low contact angle is attributed to the hydrophilic surface, reveling good adhesiveness and good wettability, and indicating high free energy of the solid surface. It should be noticed that hydrogen treatment of the diamond surface leads to the high contact angle values and respectively surface hydrophobic behavior. Vice versa surface oxidation surface leads to the low contact angle values and respectively surface hydrophilic behavior.

In terms of this work contact angle measurements revealing surface wettability is presented in the Chapter 4.6. The setup Drop Shape Analyzer – DSA100 manufactured by KRÜSS GmbH (Hamburg, Germany) (Fig. 37) and water droplet of 1 ml of Type I laboratory purified by the Arium 611UV (Sartorius AG, Goettingen, Germany) has been used.

Fig. 37 Drop Shape Analyzer DSA100 KRÜSS.

Technical data:

Measuring range Contact angle Surface tension	 1-180° 0.01 to 1000 mN/m
Measurement resolution Contact angle Surface tension	 0.1° 0.01 mN/m
Zoom	7 times
Camera resolution (standard camera)	780 × 580 px
Dimensions (standard frame)	555 × 375 × 490 mm
Weight	approx. 35 kg

3.8. Wet chemical treatment with acids

Fig. 38 shows chemical treatment stage. System main part is a chemical cooling condenser tube system positioned on the adjustable platform. Glass with acids attached to the bottom of this tube. On top attached exhaust ventilation line tube, for a safety reasons it is connected to the empty glass reservoir and glass reservoir whereas the second one is filled with the base solution.

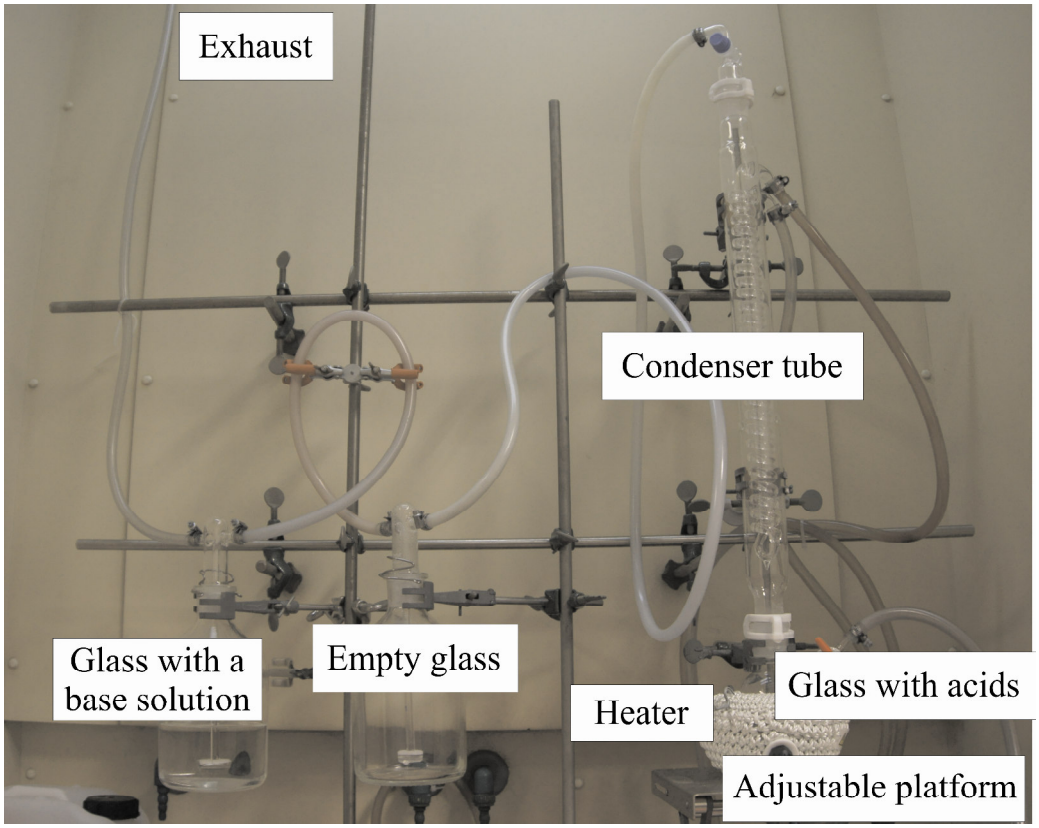

Fig. 38 Chemical treatment stage.

In order to remove graphitized layers wet chemical treatment used extensively. One of the most popular acid treatment methods is boiling in a mixture 10 ml (1:1:1) of H_2SO_4 /HNO_3 /$HClO_4$. Acids should HPLC grade quality in order to avoid probe contamination. For treatment of our samples 4 hours standard treatment applied and extended 8 hours boiling for some samples at the temperature of 359 ± 2° C performed. It is important to mention that during the acid boiling hazardous toxic nitrogen dioxide gas produced. Thus after acid boiling only after the condenser tube cooling and proper ventilation sample could be taken out. Probe handled using Teflon tweezers. Finally sample rinsed extensively in Type I purified laboratory water (Arium 611UV, Sartorius AG, Goettingen, Germany).

References:

[1] M. W. Johnson, P. Bunyk, F. Maibaum, E. Tolkacheva, A. J. Berkley, E. M. Chapple, R. Harris, J. Johansson, T. Lanting, I. Perminov, E. Ladizinsky, T. Oh, and G. Rose, Supercond. Sci. Tech. **23**, 065004 (2010).

[2] R. Harris *et al.*, Phys. Rev. B **82**, 024511 (2010).

[3] P. I. Bunyk, E. M. Hoskinson, M. W. Johnson, E. Tolkacheva, F. Altomare, A. J. Berkley, R. Harris, J. P. Hilton, T. Lanting, A. J. Przybysz, and J. Whittaker, IEEE Trans. Appl. Supercond. **24**, 1700110 (2014).

[4] R. J. Epstein, F. M. Mendoza, Y. K. Kato, and D. D. Awschalom, Nature Physics **1**, 94 (2005).

[5] T. D. Ladd, F. Jelezko, R. Laflamme, Y. Nakamura, C. Monroe, and J. L. O'Brien, Nature **464**, 45 (2010).

[6] J. Wrachtrup, PNAS **107**, 9479 (2010).

[7] H. Umezawa, T. Matsumoto, and S. I. Shikata, IEEE Electron Device Lett. **35**, 1112 (2014).

[8] T. Iwasaki, Y. Hoshino, K. Tsuzuki, H. Kato, T. Makino, M. Ogura, D. Takeuchi, T. Matsumoto, H. Okushi, S. Yamasaki, and M. Hatano, Appl. Phys. Express **5**, 091301 (2012).

[9] P. Rath, S. Ummethala, S. Diewald, G. Lewes-Malandrakis, D. Brink, N. Heidrich, C. Nebel, and W. H. P. Pernice, Appl. Phys. Lett. **105**, 251102 (2014).

[10] R. S. Sussmann, *CVD Diamond for Electronic Devices and Sensors* (John Wiley & Sons, Ltd, 2009).

[11] J. V. Macpherson, Phys. Chem. Chem. Phys. **17**, 2935 (2015).

[12] K. B. Holt, Phys. Chem. Chem. Phys. **12**, 2048 (2010).

[13] J. A. Garrido, A. Härtl, S. Kuch, M. Stutzmann, O. A. Williams, and R. B. Jackmann, Appl. Phys. Lett. **86**, 073504 (2005).

[14] K. V. Purtov, A. I. Petunin, A. E. Burov, A. P. Puzyr, and V. S. Bondar, Nanoscale Res. Lett. **5**, 631 (2010).

[15] I. Rehor, J. Slegerova, J. Kucka, V. Proks, V. Petrakova, M. P. Adam, F. Treussart, S. Turner, S. Bals, P. Sacha, M. Ledvina, A. M. Wen, N. F. Steinmetz, and P. Cigler, Small **10**, 1106 (2014).

[16] E. K. Chow, X. Q. Zhang, M. Chen, R. Lam, E. Robinson, H. J. Huang, D. Schaffer, E. Osawa, A. Goga, and D. Ho, Sci. Trans. Med. **3**, 73ra21 (2011).

[17] Z. Xing, T. O. Pedersen, X. J. Wu, Y. Xue, Y. Sun, A. Finne-Wistrand, F. R. Kloss, T. Waag, A. Krueger, D. Steinmuller-Nethl, and K. Mustafa, Tissue Eng. **19**, 1783 (2013).

[18] J. C. Angus, in *The Physics of Diamond*, edited by A. Paoletti, and A. Tucciarone (IOS Press, Amsterdam, 1997), pp. 9.

[19] A. Paoletti, and A. Tucciarone, *The Physics of Diamond* (IOS Press, Amsterdam, 1997), Vol. 135.

[20] K. E. Spear, and J. P. Dismukes, *Synthetic Diamond: Emerging CVD Science and Technology* (John Wiley & Sons, New York, 1994).

[21] J. E. Field, *The Properties of Natural and Synthetic Diamond* (Academic Press, London, 1993), Vol. 28.

[22] D. Saada, in *Physics Department* (Technion Israel Institute of Technology, Haifa, 2000).

[23] J. Schäfer, J. Ristein, R. Graupner, L. Ley, U. Stephan, T. Frauenheim, V. S. Veerasamy, G. A. J. Amaratunga, M. Weiler, and H. Ehrhardt, Phys. Rev. B **53**, 7762 (1996).
[24] G. S. Painter, D. E. Ellis, and A. R. Lubinsky, Phys. Rev. B **4**, 3610 (1971).
[25] O. I. Leipunskii, Usp. Khim. **8**, 1520 (1939).
[26] F. P. Bundy, H. T. Hall, H. M. Strong, and R. H. Wentorf, Nature **176**, 51 (1955).
[27] W. G. Eversole, edited by U. C. CorporationUSA, 1959), p. 112.
[28] J. C. Angus, H. A. Will, and W. S. Stanko, J. Appl. Phys. **39**, 2915 (1968).
[29] B. V. Derjaguin, and B. V. Splitsyn, 1980), p. 134.
[30] P. K. Bachmann, H.-J. Hagemann, H. Lade, D. Leers, F. Picht, D. U. Wiechert, and H. Wilson, Mater. Res. Soc. Symp. Proc. **339**, 267 (1994).
[31] P. W. May, Phil. Trans. Roy. Soc. Lond. A **358**, 473 (2000).
[32] S. Pezzagna, D. Rogalla, D. Wildanger, J. Meijer, and A. Zaitsev, New J. Phys. **13**, 035024 (2011).
[33] C. M. Breeding, and J. E. Shigley, Gems Gemol. **45**, 96 (2009).
[34] P. E. Pehrsson, and T. W. Mercer, Surf. Sci. **460**, 49 (2000).
[35] M. Nimmrich, M. Kittelmann, P. Rahe, A. J. Mayne, G. Dujardin, A. v. Schmidsfeld, M. Reichling, W. Harneit, and A. Kühnle, Phys. Rev. B **81**, 201403R (2010).
[36] L. Diederich, O. M. Küttel, P. Ruffieux, T. Pillo, P. Aebi, and L. Schlapbach, Surf. Sci. **417**, 41 (1998).
[37] G. Kern, J. Hafner, J. Furthmuller, and G. Kresse, Surf. Sci. **352**, 745 (1996).
[38] R. Graupner, M. Hollering, A. Ziegler, J. Ristein, L. Ley, and A. Stampfl, Phys. Rev. B **55**, 10841 (1997).
[39] K. M. C. Fu, C. Santori, P. E. Barclay, and R. G. Beausoleil, Appl. Phys. Lett. **96**, 121907 (2010).
[40] J. C. Zheng, X. N. Xie, A. T. S. Wee, and K. P. Loh, Diam. Relat. Mater. **10**, 500 (2001).
[41] G. Kern, J. Hafner, and G. Kresse, Surf. Sci. **366**, 445 (1996).
[42] J. Ristein, Appl. Phys. A **82**, 377 (2006).
[43] R. L. Bell, *Negative Electron Affinity Devices* (Clarendon Press, Oxford, 1973).
[44] L. Diederich, O. Küttel, P. Aebi, and L. Schlapbach, Surf. Sci. **418**, 219 (1998).
[45] P. Deak, B. Aradi, M. Kaviani, T. Frauenheim, and A. Gali, Phys. Rev. B **89**, 075203 (2014).
[46] J. Loubser, and J. A. van Wyk, Rep. Progr. Phys. **41**, 1201 (1978).
[47] R. Schirhagl, K. Chang, M. Loretz, and C. L. Degen, Annu. Rev. Phys. Chem. **65**, 83 (2014).
[48] V. M. Acosta, E. Bauch, M. P. Ledbetter, C. Santori, K. M. C. Fu, P. E. Barclay, R. G. Beausoleil, H. Linget, J. F. Roch, F. Treussart, S. Chemerisov, W. Gawlik, and D. Budker, Phys. Rev. B **80**, 115202 (2009).
[49] F. Jelezko, and J. Wrachtrup, Phys. Status Solidi A **203**, 3207 (2006).
[50] M. W. Doherty, J. Michl, F. Dolde, I. Jakobi, P. Neumann, N. B. Manson, and J. Wrachtrup, New J. Phys. **16**, 063067 (2014).
[51] H. Hertz, Ann. Phys. **267**, 983 (1887).
[52] A. Einstein, Ann Phys **17**, 132 (1905).
[53] K. Siegbahn, C. Nordling, A. Fahlman, R. Nordberg, K. Hamrin, J. Hedman, G. Johansson, T. Bermark, S. E. Karlsson, I. Lindgren, and B. Lindberg, Nova Acta Regiae Soc. Sci. Upsal. **20** (1967).
[54] L. C. Feldman, and J. W. Mayer, *Fundamentals of Surface and Thin Film Analysis* (Elsevier Science Publishing Co., New York, 1986).

[55] J. Chastain, and J. F. Moulder, *Handbook of X-Ray Photoelectron Spectroscopy: A Reference Book of Standard Spectra for Identification and Interpretation of XPS Data* (Physical Electronics Division, Perkin-Elmer Corporation, 1992).
[56] Y. Mizokawa, T. Miyasato, S. Nakamura, K. M. Geib, and C. W. Wilmsen, Surf. Sci. **182**, 431 (1987).
[57] T. Chasse, H. Peisert, P. Streubel, R. Szargan, and A. Meisel, Acta Phys. Pol. **83**, 793 (1993).
[58] J. C. Lascovich, R. Giorgi, and S. Scaglione, Appl. Surf. Sci. **47**, 17 (1991).
[59] J. C. Lascovich, and S. Scaglione, Appl. Surf. Sci. **78**, 17 (1994).
[60] S. W. Gaarenstroom, and N. Winograd, J. Chem. Phys. **67**, 3500 (1977).
[61] P. van der Heid, *X-ray Photoelectron Spectroscopy* (Wiley and Sons Inc., New Jersey, 2012).
[62] D. Briggs, *Handbook of X-ray and ultraviolet photoelectron spectroscopy* (Heyden & Son LTD, 1977).
[63] F. I. Vilesov, B. L. Kurbatov, and T. A.N., Sov. Phys. Dokl. **6**, 490 (1961).
[64] D. W. Turner, and M. I. A. Jobory, J. Chem. Phys. **37**, 3007 (1962).
[65] J. W. Rabalais, *Principles of ultraviolet photoelectron spectroscopy* (Wiley, New York, 1976).
[66] K. Oura, V. G. Lifshits, A. Saranin, A. V. Zotov, and M. Katayama, *Surface Science An Introduction* (Springer, Berlin, 2010).
[67] M. Minsky, Scanning **10**, 128 (1988).
[68] Y. Shapiro, in *Fachbereich Chemie, Pharmazie und Geowissenschaften* (Johannes Gutenberg-Universität Mainz, Mainz, 2015).

Chapter IV

In this chapter the MIES spectroscopy and setup design are introduced. Also the experimental results comprise diamond samples preparation and characterizations are presented. Preparation includes nitrogen doping of diamonds; oxidation, hydrogenation, dry etching in UHV condition and via wet chemical treatment. Samples measured by means of XPS, UPS, MIES spectroscopy, wet contact angle analyses and confocal measurements from our colleagues attached to reveal the effect of implantation.

4.1. Principles and setup for metastable impact electron spectroscopy (MIES)

In the first part unique surface spectroscopy technique and instrumentation design for probing outermost surface structure is introduced. This surface spectroscopy called metastable impact electron spectroscopy (MIES). It is presented in the article format that is submitted in the Review of Scientific Instruments journal and expected to be published soon.

The distinctive instrumentation design origin from the earlier TU Clausthal (Germany) design has been redesigned, improved and assembled in the Prof. Michael Reichling "Nanoscience" group by Dr. Andrij Borodin.

As a PhD student, I made an important contribution to the optimization of MIES plasma source optimal stable operation parameters, as well as performing MIES spectroscopy studies on diamond and TiO2 materials including following paper impact.

Dual Discharge Source for Metastable Impact Electron Spectroscopy and Ultraviolet Photoelectron Spectroscopy of solid surfaces

Andriy Borodin, Oleksiy Dyachenko and Michael Reichling

Fachbereich Physik, Universität Osnabrück, Barbarastr. 7, 49076 Osnabrück, Germany

We describe a source providing a high flux of excited He atoms (He^*) and ultraviolet photons for quasi-simultaneous measurements of metastable impact electron spectroscopy (MIES) and ultraviolet photoelectron spectroscopy (UPS). As a new feature compared to previously introduced designs, we introduce a tuneable secondary discharge for the generation of He^* and photons. The dual discharge source yields a He^* flux of approximately $2 \cdot 10^{14}$ atoms/sr with a flux stability of typically $1.2 \cdot 10^{10}$ atoms/s. To demonstrate key features of MIES and the performance of the spectroscopy system, we investigate the development of the surface electronic structure of a $TiO_2(110)$ surface upon adsorption of sodium up to one monolayer. The different processes of the interaction between He^* and the surface are discussed and it is shown that the peak associated with emission from the singlet state is the result of autodetachment. The capability in separating MIES and UPS signals by a time-of-flight technique is illustrated for spectroscopy of the intense Na3s peak.

I. INTRODUCTION

Metastable impact electron spectroscopy (MIES) is a powerful technique for the investigation of the electronic structure in the valence band region. Having various alternative designations such as PIES (Penning Ionization Electron Spectroscopy), MAES (Metastable Atom Electron Spectroscopy) and MDS (Metastable Deexcitation Spectroscopy), the technique has successfully been applied to a wide variety of systems like molecules in the gas phase,[1, 2] liquid surfaces[3-5] and surfaces of solids.[6-8] The concept underlying all of these studies is the energy analysis of secondary electrons created by the interaction of excited noble gas atoms, mostly helium, further on denoted as He^* with a molecule in a collimated beam or a solid or liquid surface. In the latter case, utmost surface sensitivity is the core strength of the method. As the discharge generating He^* also produces photons with an energy in the ultraviolet (UV) spectral region, the MIES measurement is often combined with ultraviolet photoelectron spectroscopy (UPS). For our applications, the spectroscopies are exclusively used for solid surface science studies and, therefore, the He^*/photon source, the sample, the electron energy analyser as well as other devices used for sample preparation are integrated in an ultra-high vacuum system to ensure the cleanliness of surfaces once prepared in-situ.

Various designs have been developed in research laboratories for generating metastable atoms[1, 9-11] and to our knowledge, there is no commercially available source. The operation of such devices often suffers from instabilities and likewise, the UV photon flux is small compared to conventional UPS sources. However, in recent years, the performance of metastable atom sources has been improved continuously, e.g. by adding a booster pump and a nozzle for the discharge source[12] or a quenching component enhancement.[10] Here, we introduce an optimised source with a design based on a development at the Technische Universtät Clausthal (Germany). Such instruments have served the needs for surface studies on a variety of systems[8, 9, 13-18] and excel in cases where the quasi-simultaneous measurement of MIES and UPS signals is required. Separating MIES and UPS signals is accomplished by a time-of-flight separation for photons and electrons.[9]

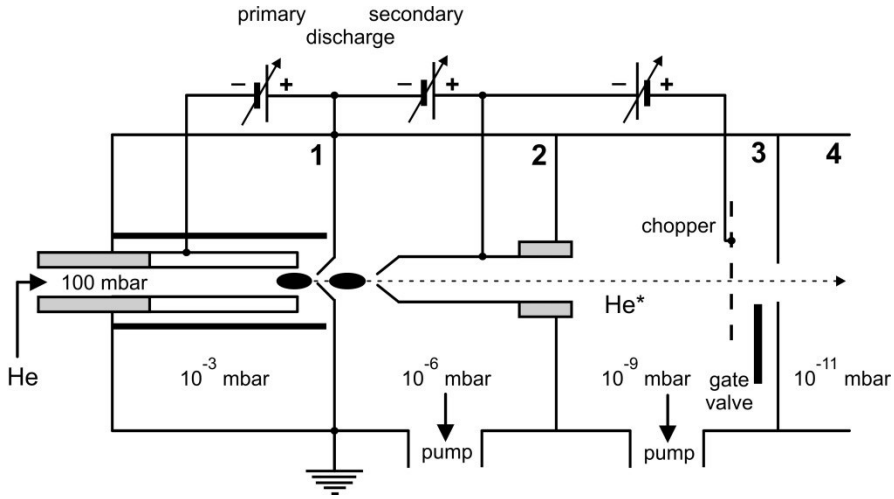

Figure 1. *Schematic overview of the dual discharge MIES source.*

So far, there is no standard design of a MIES source, however, the sources yielding highest intensity[9] have common features similar to our source schematically depicted in Figure 1. Helium is introduced in the high pressure region of the discharge chamber (1) where a cold cathode gas discharge is ignited at a pressure of typically 20 to 100 mbar; this is further on denoted as the *primary discharge*. A cold cathode gas discharge is generally used as He^* with thermal kinetic energy are required for non-destructive surface probing. Surplus helium is released in the differentially pumped discharge chamber (1) where a pressure of typically $1 \cdot 10^{-3}$ mbar is maintained. From the discharge, excited He atoms expand into a high vacuum region through a first skimmer with a millimetre-size aperture to form the *secondary discharge* in the expansion chamber (2) where a pressure of typically $1 \cdot 10^{-6}$ mbar is maintained. To obtain a high flux of metastable atoms, it is important to constrain the discharge current to a small volume crossed by the helium beam so that a large fraction of atoms is excited and to ensure that most of the excited atoms reach the sample following the path of direct line-of-sight. To avoid collisions, the He^* atoms next passes a well pumped ultra-high vacuum buffer chamber (3) separated by a second skimmer from the expansion chamber. The buffer chamber (3) where a pressure of typically $1 \cdot 10^{-9}$ mbar is maintained is a convenient place for mounting the chopper used for the time-of-flight (TOF) separation of photons and atoms. After having passed the chopper, excited atoms travel into the measurement chamber through the penetration orifice (4) where a base pressure below $5 \cdot 10^{-11}$ mbar is maintained through an aperture that can be closed in the fashion of a gate valve. When Helium is introduced for operating the MIES source, the total pressure in the measurement chamber typically rises to a value of $6 \cdot 10^{-9}$ mbar.

Two types of metastable atoms are produced in the plasma, namely singlet $He^*(2^1S)$ with an ionization potential of 3.97 eV and an excitation energy of20.62 eV and triplet $He^*(2^3S)$ with an ionization potential of 4.77 eV and an excitation energy of 19.82 eV.[6] However, for the measurements, we exclusively use the high yield component $He^*(2^3S)$ while $He^*(2^1S)$ produces minor artefacts as discussed below. Compared to a conventional UV photon source emitting both, 21.2 eV (He I) and 40.8 eV (He II) lines, our plasma source produces only He I photons.

II. Source design and construction

The MIES source is integrated in the side arm of a large UHV chamber acting as the preparation and measurement chamber. Figure 2 shows the engineering drawing of the side arm with the metastable atom source in a cross-sectional view. All parts are machined from stainless steel unless otherwise noted. The discharge chamber (1) as well as expansion (2) and buffer (3) chambers are made from standard stainless steel tubes joint by CF100 flanges and are pumped by a 500 l/s turbo molecular pump TMU 521P (Pfeiffer Vacuum GmbH, Asslar, Germany) attached to the left CF100 flange and a 70 l/s turbo molecular pump TurboVac TMP 50 (Oerlikon Leybold Vacuum GmbH, Köln, Germany) attached to the lower CF63 flange. The chopper unit for TOF separation is mounted on the upper CF63 flange. The right

hand side CF100 flange of the buffer chamber is connected to the measurement chamber via a home-made gate valve (4) having an opening of 1 mm diameter guiding He^* into the measurement chamber. The He gas (99,996 % purity, Air Liquide GmbH, Düsseldorf, Germany) supplied from the pressure regulator of a high pressure gas bottle is fed into the discharge chamber through the hollow molybdenum cathode.

The spacer flange (5) between the expansion chamber and the buffer chamber is hollow and flushed by cooling water providing an efficient heat drain for all parts close to the discharge region. A most important point in machining the parts is utmost precision, specifically a perfect alignment of all apertures and skimmers passed by the He^* atoms.

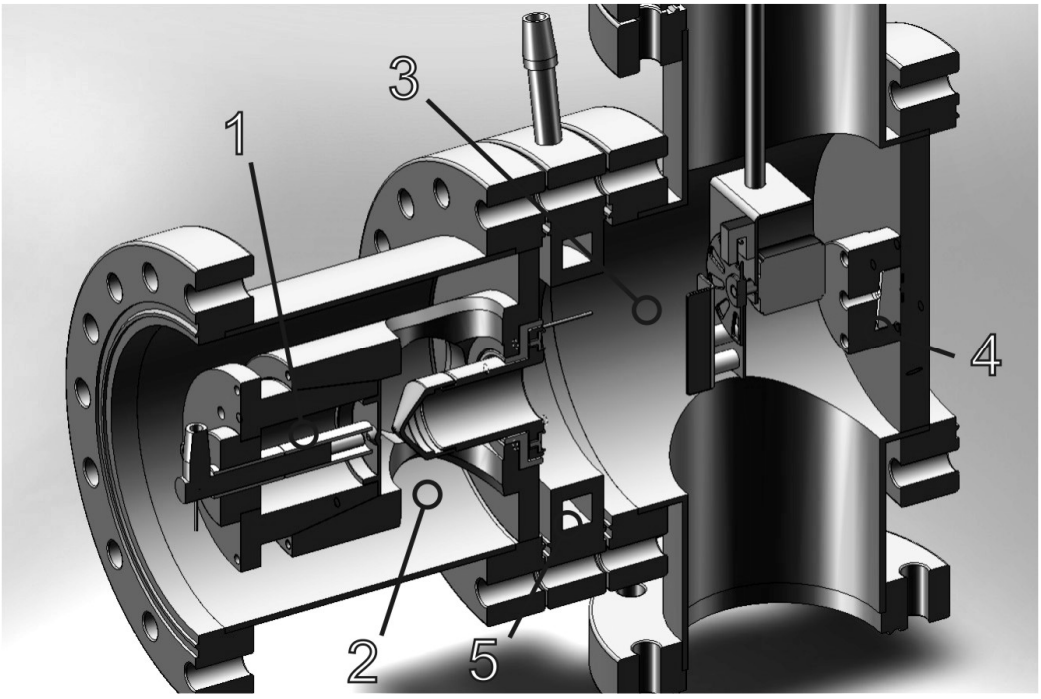

***Figure 2**. Cross-sectional view of the MIES source.*

Figure 3 is a detail view of the discharge region. The tungsten cathode (2) is a tube with 1 mm inner diameter screwed in the He gas feeding stainless steel tube (4) having a diameter of 4 mm. The primary discharge in chamber (1) is ignited between the cathode and a spike of the first skimmer acting as the anode (3). The anode orifice has an exchangeable inner part to install a spark erosion-machined hole with a well-defined diameter of 0.15 to 0.4 mm adaptable to the desired type of discharge. As a voltage is applied between anode and cathode, the cathode holding tube is electrically isolated from the chamber body by the ceramic tube (5). The cathode covered by the ceramic tube a length of 15 mm, whereas the end of the tube positioned close to the anode in order to restrict the discharge region close to the anode orifice. During continued operation of the source, the cathode undergoes erosion and needs to be replaced in intervals of several hundred hours of operation.

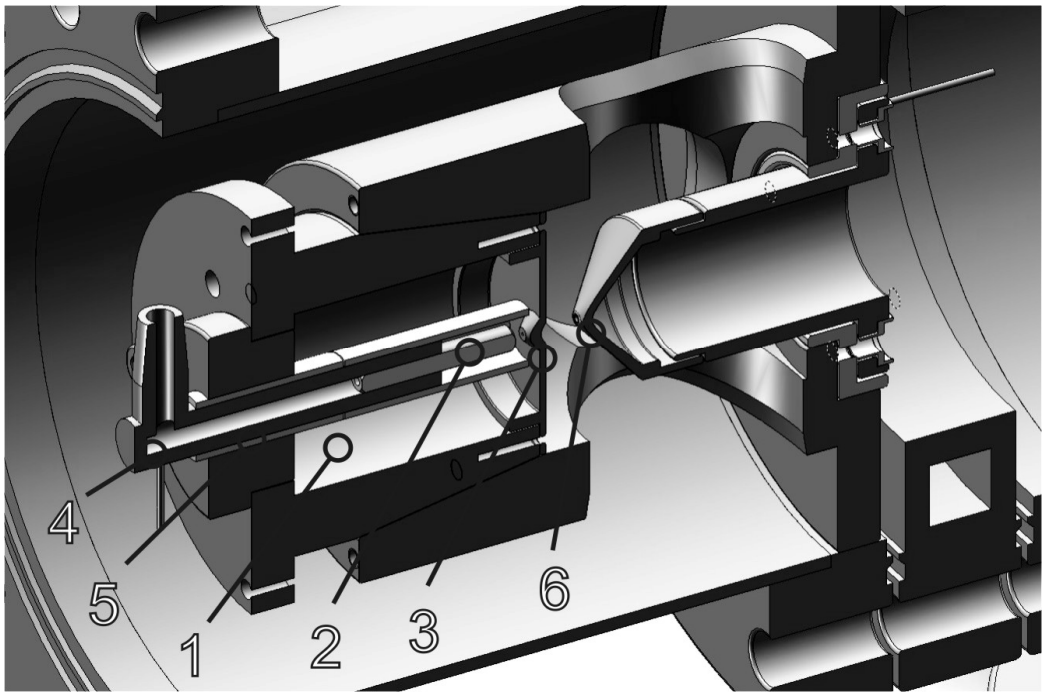

Figure 3. *Detail cross-sectional view of the MIES source discharge region.*

Escaping trough the anode orifice from the discharge chamber (2), He^* atoms and He^+ ions travel to the expansion chamber and a small fraction of them further into the buffer chamber through the second skimmer (6) having an aperture width of 2 mm. The particle beam is still dense in front of the skimmer and contains charged species facilitating the ignition of the secondary discharge between the grounded first skimmer (3) as the cathode (anode of the primary discharge) and the second skimmer (6) as the anode that is electrically isolated from the chamber body.[19]

All distances that are critical for the operation of the source like the one between the cathode and the anode, between the ceramic tube around the cathode and the anode as well as the distance between the anode and the skimmer can be adjusted. The optimum values for the distances specified below are the result of an optimisation for our source and applications; optimum values may be different for another environment.

III. Discharges

Compared to a single discharge MIES source, the coupled discharge operation provides an enhanced flux of metastable atoms and a much higher flux stability. The basic idea for using a double discharge source is to use the high flux of He* from the stable primary high pressure discharge to inject charged particles into the secondary discharge operated at low pressure. The high density in the primary discharge results in strong metastable quenching so that it is not efficient as a high flux and high stability He* source. However, the low density discharge yields a high flux of He* while it is stabilised by the constant flux of particles from the

primary discharge. If required, a high UV photon flux can be achieved by increasing the working pressure for both discharges.

A twin power supply HCD 140M-1250 (FuG Elektronik GmbH, Rosenheim, Germany) is used to provide a stabilised current for the first and the second discharge, respectively. The working pressure in the discharge chamber is typically 100 mbar and the primary discharge current stabilised at 30 to 60 mA yielding a voltage in the 200 to 350 V range. The cathode-anode distance is typically 1.5 mm, the space between the ceramic tube and the anode plate of the first skimmer adjusted to about 1 mm. The distance between the first and the second skimmer controlling the secondary discharge is typically 8 mm and this discharge is also operated at currents of 30 to 60 mA yielding a voltage of 80 to 350 V applied between the first and the second skimmer (6). For standard operation, the voltage and current values are set to 290 V/37.5 mA for the first discharge and to 300 V/40 mA for the second discharge.

It is difficult to estimate the actual pressure in the region of the secondary discharge due to the strong molecular flow close to the anode orifice. After expansion into the primary chamber (1 in Figs. 1 and 2), the measured pressure is typically $1.3 \cdot 10^{-3}$ mbar. The pressure in the expansion chamber (2 in Figs. 1 and 2) depends on the balance between the incoming gas flow and the pumping speed. As we are interested in a high flux of metastable atoms, a reasonable way to obtain appropriate conditions for the secondary discharge is the adjustment of the first skimmer aperture size, however this shifts the gas flow balance. To maintain the pressure conditions described here, we need a pumping speed of 350 to 550 l/s and an anode orifice diameter in the range of 0.15 to 0.4 mm. The orifice diameter typically used is 0.3 mm.

The secondary discharge cannot be ignited or maintained without a constant flow of charged species from the primary discharge. Therefore, the optimisation of both discharges is coupled to each other. To ignite the secondary discharge, a voltage pulse of typically 300 V is applied between the first and the second skimmer and the voltage is then set to a suitable constant voltage maintaining the discharge.

The primary discharge may be classified as a glow discharge;[20] it may remain stable even if the pressure is decreased to 20 mbar. However, to yield optimum conditions for the secondary discharge, the pressure should be at least 60 mbar. Higher pressure values cause a stronger interaction between metastable species and, therefore, a quenching of metastable states yielding a decrease in the overall metastable flux; the flux of UV photons, however, rises with increasing He pressure. The second discharge can hardly be associated to a certain type. Due to the technical construction of the source it is not possible to measure the plasma discharge distribution with a probe; we notice, however, that the voltage rises when the current is increased.

IV. Time-of-flight analysis

The source generates both, metastable atoms and UV photons, both reaching the sample that is in direct line of sight with the discharge regions and both generating electron emission

signals. To separate the signals generated by He^* from those generated by UV photons, we apply a time-of-flight (TOF) separation technique. A chopper wheel is introduced in the path of metastable atoms and photons and by a gated detection synchronised with the chopper, the electron signals for MIES and UPS are separated in respective bins. This set-up allows a quasi-simultaneous detection of MIES and UPS signals with a small cross-talk.

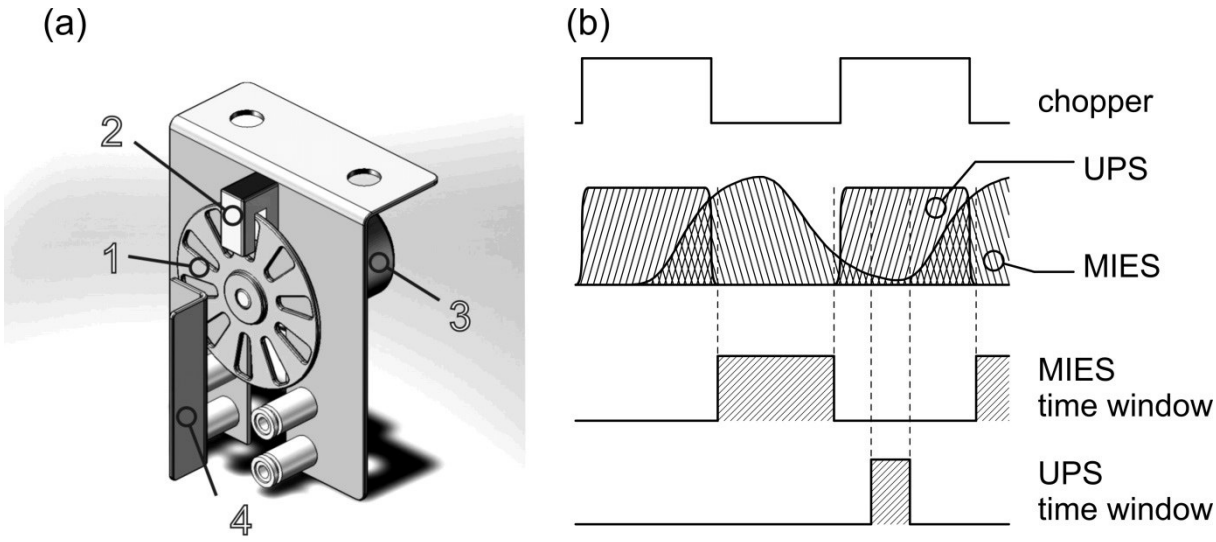

Figure 4. *(a) Technical drawing of the chopper unit. (b) Electron signals for MIES and UPS and their TOF analysis by gates sampling the electron signal in corresponding time windows.*

Figure 4(a) shows the chopper unit that is placed in the buffer chamber (3 in Figs. 1 and 2) close to the valve (4 in Fig. 2) separating this section from the measurement chamber. The chopper wheel (1) is driven by a DC motor (model 1516EO12S, Dr. Fritz Faulhaber GmbH, Schoenaich, Germany) where the position of the chopper wheel with the openings is determined by a forked light barrier (2) positioned opposite to the opening where atoms and photons pass. The rectangular steel sheet mounted close to the chopper blade (4) is kept at a potential of -200 V with respect to ground to act as a deflection plate removing charged species from the beam passing the chopper.

The width of the openings in the chopper blade is equal to the width of the spokes resulting in a duty cycle of one for the periodically interrupted flux of excited atoms and photons. Having passed the chopper, UV photons reach the probe quasi instantaneously, so that the intensity of UPS generated electrons reproduces the chopper profile as schematically shown in Fig. 4(b). The temporal profile of the MIES signal, however, depends on the velocity distribution of the metastable atoms. This distribution deviates from the Maxwell-Boltzmann distribution describing atoms in a thermal equilibrium due to the directed flow of excited atoms through nozzles. The characteristic speed of the distribution is, however, comparable to that of a thermal velocity distribution for a gas in equilibrium at the temperature of the discharge.[11] The directional flow yields a faster decay of the tail of the TOF distribution than it would be

expected from the respective Maxwell-Boltzmann distribution. The maximum of the velocity distribution is found at values ranging from 1600 to 2000 m/s as determined from monitoring the MIES signal for different chopper speed and relating this to the 400 mm distance of travel from the chopper to the sample. Under these circumstances, a chopping frequency of about 2000 s^{-1} allows an optimum separation of MIES and UPS signals with the gating scheme shown in Fig. 4(b). Most of the MIES intensity appears in the period of closed chopper allowing the collection of a strong MIES signal unaffected by the UPS signal. On the other hand, the tail of the MIES signal from one chopper period has not fully decayed to zero upon the start of the next one. Therefore, the UPS signal is always superimposed by some of the MIES signal. To minimise the MIES contribution, the width of the gate selecting the UPS signal is typically not more than 15% of the width of the MIES gate and the UPS gate is positioned at the minimum of the MIES intensity. This reduces the UPS signal but allows limiting the contribution of the MIES signal to a value below 3%. A homebuilt controller electronics is used to generate the chopper control voltage and gating signals for the collection of signals into MIES and UPS bins.

V. Metastable atom flux and flux stability

The intensity of a radiant source is commonly defined as the radiant power emitted per solid angle. However, for a MIES measurement, this parameter cannot be unreservedly accepted as a figure of merit. The most powerful MIES sources are designed for investigations in the gas phase[10] where the interaction between metastable atoms and the target occurs in a collision cell or in a region of crossed beams, namely under conditions where the width of the metastable atom beam does not limit the measurement. However, for a measurement on a solid surface, the width of the beam should be smaller than the surface area in the sample plane. For a beam with large divergence, at least the core region of the beam should cover the sample.

Electron spectra are recorded by a hemispherical electron energy analyser (PHOIBOS 100, Specs GmbH, Berlin, Germany) equipped with an extended range channel electron multiplier (CEM) operated in the fixed retarding analysis mode and the “medium area” lens mode yileding an analyser acceptance area of 2 mm spot size with a pass energy of 5.42 eV. Electrons emitted from the sample surface are collected by the electron analyser optics and retarded or accelerated according to the kinetic energy to be analysed. Electrons having the pass energy of the hemispherical analyser reach the detector that is an array of five CEMs arranged in a row next to each other. The assembly of five CEMs is referred to as a Multi Channel Detector (MCD), where each channel is equipped with a separate preamplifier placed outside of the vacuum chamber. The number of incoming electrons is recorded separately for each channel and is stored and processed separately by the data acquisition unit. The signal we use is always the sum of all CEMs. The analyser WF is defined by the manufacturer and is 4 eV for the PHOIBOS 100. By the sample binding energy (E_B) calculation analyser WF correction is automatically applied by software.

To precisely resolve the low-energy cut-off in the electron spectra and to avoid possible irregularities of the analyser transmission function for electrons with low kinetic energies in valence band spectra, the sample is biased by -15.00 V.

Generally the kinetic energy scale is corrected for this bias voltage and for the analyser work function and E_B is defined by the following calculation:

$$E_B = \mathrm{He}\ (2^3S) + E_{bias} - E_{KR},$$

where E_{KR} is corresponding recorded kinetic energy, the excitation energy He (2^3S) is 19.82 eV and E_{bias} is the bias value of 15.00 eV.

The Fermi edge cut-off energy E_F is determined from electron emission spectra by linearly extrapolating the yield curve and determining the point of intersection with the zero yield intensity towards abscissa axis. The low energy secondary electrons peak cut-off directly yields the sample work function (WF). The time for collecting a spectrum varies between 60 and 100 s. Derived E_B energy values plotted as x – axis towards the corresponding electron yield values on the y – axis.

Estimating the flux of metastable atoms is not straightforward as He^* and UV photons are emitted where their flux and ratio of fluxes varies with the operation parameters of the source. A further complication is the TOF selection separating MIES and UPS signals changing the transmission according to the gating settings. As we can neither directly measure the flux of metastable atoms nor the photon flux, we estimate the emission power of the source from a measurement of the electron yield received from a standard sample under standard conditions. As a standard sample, we use a well prepared diamond surface described in detail below. By recording the total intensity for deactivated TOF separation yielding MIES and UPS electron signals at the same time and comparing results with MIES spectra recorded with activated TOF separation, the MIES intensity can be estimated to be one third of the total electron yield under standard conditions used for most of our measurements. Assuming that MIES and UPS processes have an equal electron yield and that every He^* or UV photon yields one electron, we estimate the total number of the metastable atoms reaching the sample by measuring the sample current that is equal to the current of electrons emitted from the surface. Using a clean stainless steel plate as the sample and deactivating TOF separation yields a current of $4 \cdot 10^{-9}$ A converting to $1 \cdot 10^{10}$ metastable atoms per second impinging on the surface. Further, assuming that the region exposed to He^* is a circle of 3 mm diameter (calculated according to the beam thermal expansion taking into account the diameter of the beam penetration orifice and the distance between this hole and the sample), we obtain as a very rough estimate of the flux of metastable atoms $2 \cdot 10^{14}$ atoms/sr. For operation with TOF selection, we estimate a flux of $2 \cdot 10^{13}$ UV photons/sr what is much smaller than the flux of most commercial UPS sources. However, for all of our applications, we obtain MIES and UPS electron count rates that are high enough to yield well-resolved spectra within a relatively short sampling time.

Due to the optimised design of the source, we yield a high flux of He^* with high overall stability. The short period stability is mainly limited by the properties of the plasma that is a

highly non-linear dynamical system inherently exhibiting fluctuations od different nature. Common phenomena are that the plasma is quenched or, more likely, fluctuations or blinking of the discharge occurs. Such phenomena often result in saw-tooth shaped artefacts in MIES spectra. In our system, we can avoid such phenomena by the dual discharge design of the metastable atom source. As the primary discharge is operated at a relatively high pressure, it exhibits a high stability. However, the number of metastable atoms emitted from this discharge is not more than a few % of the total number of emitted atoms. Therefore, the key factor for flux stability is the secondary discharge being the main generator of metastable species.

To test the stability of the source under conditions of optimised dual discharge operation, we monitor the electron yield in the valence band region of our standard sample for half an hour. The sample is a piece of CVD Ib diamond (Element Six Ltd., Ascot, United Kingdom) with (100) surface orientation and dimensions of 3 x 3 x 0.5 mm^3. As there is only negligible surface degradation of the freshly prepared sample under UHV condition, such kind of sample is a good choice for a long term stability measurement. The surface is prepared and cleaned by procedures described in detail elsewhere to obtain a clean surface with high sp^3 phase purity.[21] After preparation, the sample is heated to a temperature of 450°C and its cleanliness checked by XPS. The MIES spectrum obtained shortly after surface preparation shown in Fig. 5(a) exhibits characteristic features, namely an intense secondary electron peak close to the work function edge at 15.44 eV, a plateau in the band gap region around 8 eV binding energy and an emission with intensity diminishing towards E_F. For the flux stability measurement, the valence band emission intensity is integrated over the energy range from 6 eV to10 eV to reduce statistical fluctuation to a negligible value and the integral value is plotted against the elapsed time as shown in Fig. 5(b). MIES spectra are taken every 53 sec with an overall measurement time of 32 min. The measured values are fitted by the solid line shown in Fig. 5(b) revealing a decrease of 10 % of the initial flux. Short term stability is estimated from the RMS value of the differences between the measured flux and the corresponding value of the fitted curve yielding 1.28 % fluctuation.

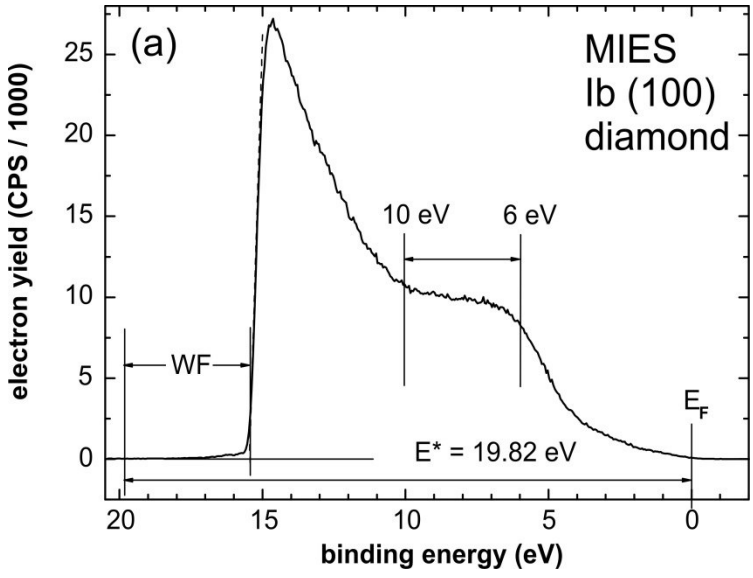

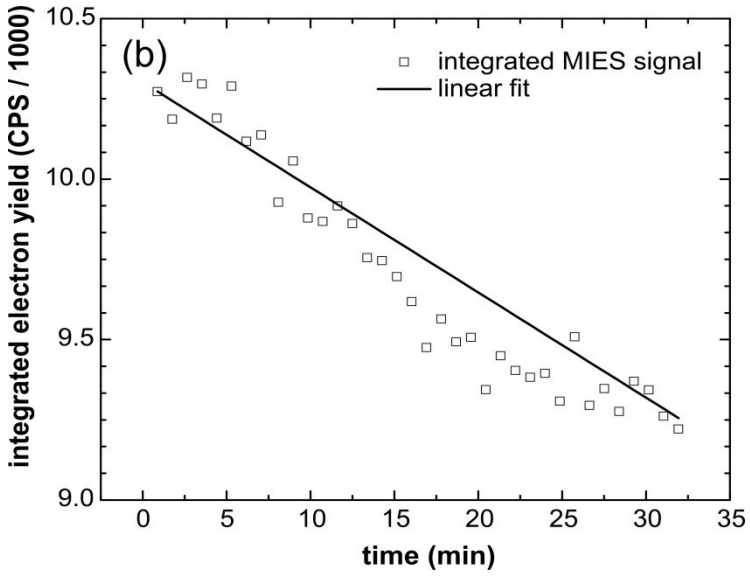

Figure 5. *(a) MIES spectrum of IIb diamond(100) measured shortly after surface preparation. (b) MIES intensity integrated in the region of 6 to 10 eV binding energy measured in intervals of 53 sec plotted as a function of elapsed time. The solid line is a fit curve yielding long term drop of electron yield while a statistical evaluation of differences between the integrated signal and corresponding values of the fit curve yields short term stability.*

VI. Demonstration of MIES processes and instrument capabilities

To demonstrate the capabilities and strength of the MIES technique, we report on measurements performed on clean and sodium covered rutile TiO_2 (110) surfaces. This is a system well suited for this purpose as it reveals certain surface related features that can be precisely determined by MIES operated with a high flux of metastable atoms but not by other surface science techniques. Furthermore, in MIES on this system, different mechanisms of metastable atom de-excitation are active in dependence of the surface state.

The TiO_2 crystal (highest purity, MTI Corporation, Richmond, USA) has dimensions of 10 x 10 x 0.5 mm^3 and its (110) surface is prepared by typically 40 sputter–annealing cycles. This is accomplished by Ar^+ ion sputtering at an energy of 1 keV for 15 min and annealing at a temperature in the range of 525 to 575 °C for several minutes. To avoid the excessive formation of vacancy defects in the bulk, the temperature is strictly kept within these limits and to avoid contamination of the most reactive surface from constituents of the residual gas, it is important to keep the base pressure below $5 \cdot 10^{-11}$ mbar. To maintain such vacuum conditions, the measurement chamber is equipped with a turbo molecular pump HiPace 700 (Pfeiffer Vacuum GmbH, Asslar, Germany), two liquid nitrogen cold traps, a Ti sublimator and a sorption getter pump CapaciTorr D400-2 (SAES Getters S.p.A., Milano, Italy). Further

details of preparation, geometric surface structure, surface defect formation and the impact of surface defects on the work function of clean TiO_2 (110) have been reported previously[7, 22, 23] and references therein. Sodium is evaporated from a commercial alkali source (Type S, Alvatec GmbH, Althofen, Austria) operated with a current in the range of 5.2 to 5.4 A. The alkali surface exposure is controlled by a mechanical shutter and the coverage is calibrated by a quartz crystal microbalance INFICON IC/5 (INFICON, New York, USA). During operation of the electron analyser for collecting MIES/UPS spectra, the current for heating the Na evaporator is switched off to avoid a deterioration of electron spectra due to current-induced magnetic stray fields.

In Figure 6, we show a typical series of MIES/UPS spectra recorded quasi-simultaneously at room temperature on the slightly reduced surface covered with 0 to 2.4 monolayers (ML) of sodium. The bottom spectra (bold lines) are taken on the as-prepared surface. The following spectra up to the middle bold line represent spectra for a sodium coverage increasing by 0.04 ML per spectrum. In the upper half of the series, the deposition rate is adjusted to yield steps of 0.4 ML. The basic MIES features and their interpretation have already been introduced in earlier studies[24]; here we focus on a demonstration of fundamental MIES processes, a comparison of MIES and UPS results and fine details in the spectra pointing to artefacts related to the discharge and detection technique.

The series of measurements shown in Fig. 6(a) is an instructive example for different interactions between metastable helium atoms and the sample surface[6] that are illustrated schematically in Fig. 7. The bottom MIES spectrum reveals almost exclusively the Auger neutralization process (AN) resulting in one peak that is indistinguishable from the secondary electron (SE) peak. Auger neutralization takes place after a resonant transfer (RT) of the excited He2s electron to unoccupied states in the conduction band (CB) of the TiO_2 substrate. With increasing sodium coverage, the WF is lowered what is reflected in the spectra by a shift of the SE cut-off towards higher values on the binding energy scale. The RT is more and more suppressed as the CB moves away from the He2s level that is now in the band gap of TiO_2. Under such conditions, the AN process is substituted by the Auger deexcitation process (AD).

A typical MIES spectrum resulting from the AD process is the one highlighted by the bold line in the middle of Figure 6(a). Such a spectrum directly reflects the surface density of occupied states (SDOS).[25] The extraordinary surface sensitivity of MIES becomes evident by a comparison of MIES and UPS spectra. A characteristic feature of reduced TiO_2 is the presence of Ti^{3+}(3d) states originating from Ti interstitial bulk defects or surface vacancies of bridging oxygen V_{Obr}.[26, 27] The peak related to Ti^{3+}(3d) is weak but clearly present just below the Fermi energy in the UPS spectrum shown in Figure 6(b) but absent in the MIES spectrum shown in Fig. 6(a). On the other hand, alkali atoms are easily ionized by the removal of their outermost electron. As a consequence, upon sub-monolayer alkali adsorption on the TiO_2 surface, alkali atoms are ionized by donating an electron to the substrate where additional Ti^{3+}(3d) states are created,[28] as confirmed in the UPS spectrum by the peak intensity at E_B = 0.9 eV rising with increasing Na deposition. However, no electron emission

is observed in MIES in this energy region for the fully developed AD spectrum (middle heavy line in Fig. 7(a)). The absence of the Ti^{3+}(3d) peak is straightforwardly explained by associating the Ti^{3+}(3d) UPS intensity with bulk Ti^{3+} interstitial states. This is completely in line with calculations for surface O_{br} vacancies, as well as for surfaces reduced by electron doping predicting that electrons localise not on the surface but in the form of reduced sub-surface Ti^{3+}(3d) states located mainly below fivefold-coordinated Ti atoms.[29, 30] Hence, they do not appear in the SDOS measured by MIES.

Upon further Na deposition, the sodium atoms are not fully ionized anymore, which in combination with the low work function (~ 2 eV) opens an additional channel for electronic de-excitation, namely the autodetachment process illustrated in Figure 7. A Na coverage larger than ~ 0.5 ML leads to the distinguishable feature Na(3s) at $E_B = 1.45$ eV. Due to Na exposure the WF decreasing and by the saturation reach a 3.2 eV value. In this process, the MIES sensitivity towards bands close to the Fermi level is significantly enhanced while corresponding UPS spectra do not exhibit any change except for the shift in work function.

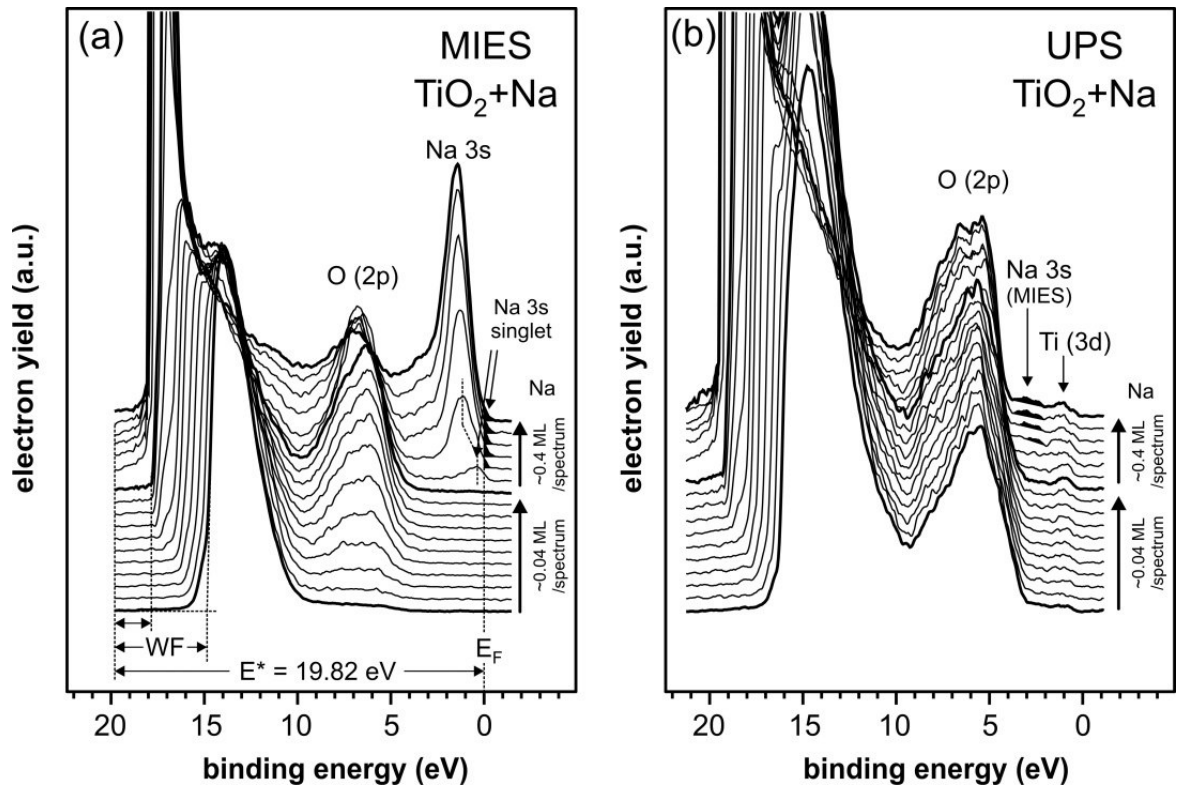

***Figure 6**. MIES (a) and UPS (b) spectra for Na deposition onto clean TiO_2(110).*

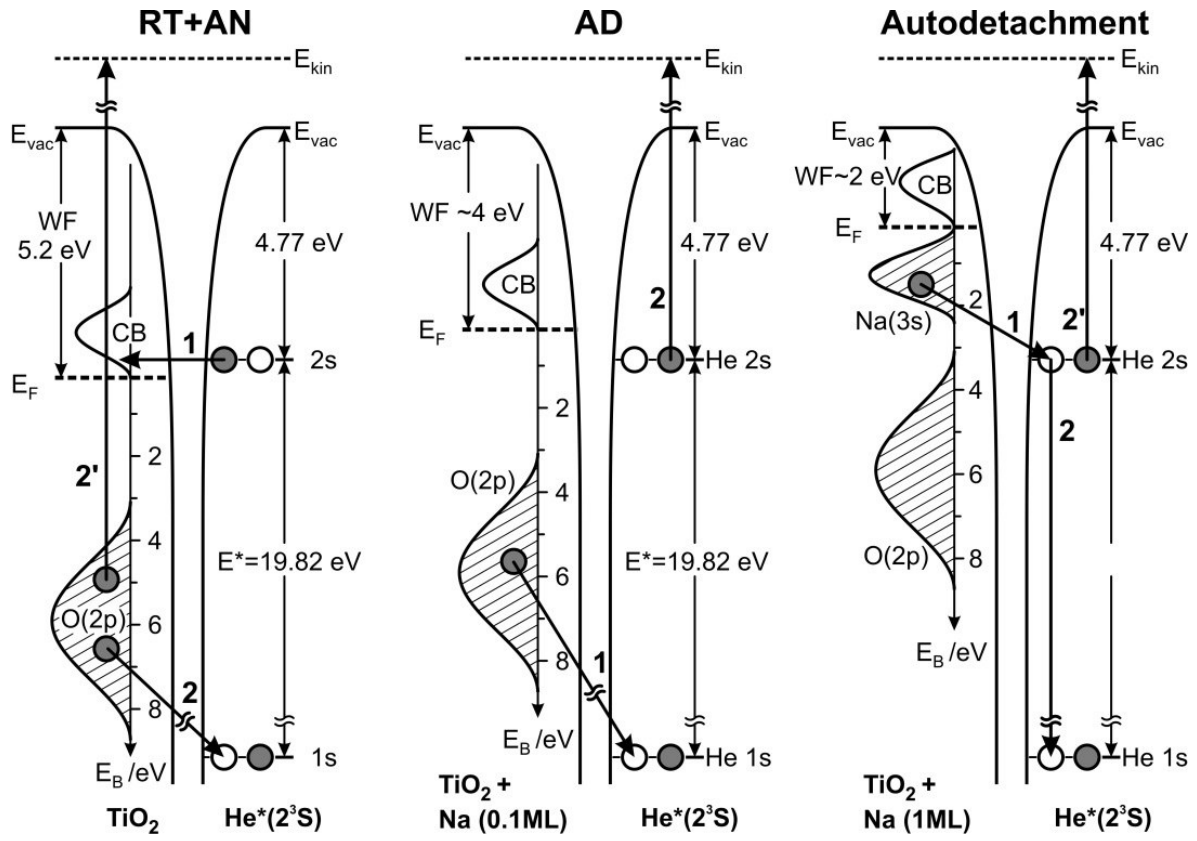

***Figure** 7. Elementary processes of the interaction between metastable He*(2^3S) and TiO_2(110) occurring upon Na deposition resulting in a shift of the work function (WF). Processes depicted are resonant transfer (RT) followed by Auger neutralization (AN), Auger deexcitation (AD) and autodetachment.*

The spectra shown in Fig. 6 further reveal certain artefacts illustrating features of MIES and UPS experiments. The first one refers to the separation of quasi-simultaneously sampled MIES and UPS spectra. The adsorption of alkali atoms producing a high intensity autodetachment peak provides a convenient means of adjusting the UPS window in the TOF unit for minimising the MIES emission that is inevitably present in UPS spectra. The upper four UPS spectra shown in Figure 6(b) exhibit the strongest Na 3s spurious MIES emission as expected from a comparison to the respective traces from Figure 6(a). From an analysis of the hatched areas and a comparison to the MIES spectra, the residual MIES contribution in UPS is estimated to be about 1% of the Na3s intensity in the respective MIES spectra.

The second artefact refers to the observation that two types of metastable atoms are generated in the plasma source, namely singlet He*(2^1S) and triplet He*(2^3S) having an ionization energy of 3.97 eV and 4.77 eV, respectively. This does not play a role for the AN process, as this process is not affected by the excitation energy, but by the ionization potential of the metastable atoms, which is identical for triplet and singlet helium species, namely 24.59 eV. However, in the AD process, a singlet to triplet conversion takes place resulting in indistinguishable spectra originating from He*(2^1S) and He*(2^3S) atoms.[6] Although, it has been observed for several systems that the singlet to triplet conversion may occur before He*

undergoes autodetachment,[31] one can notice that for the alkali/TiO_2 system this is not the case. This is revealed by a closer look on the Na3s peak shown in Fig. 6(a) exhibiting a tail ranging into the region of "negative" binding energy. In fact, this implies that the kinetic energy of respective electrons is above the excitation energy of 19.82 eV and we conclude that He*(2^1S) contributes to the excitation. Knowing the excitation energy of singlet He* (E* = 20.62 eV), we can decompose the Na 3s structure found in the MIES spectrum into two peaks with a separation of 0.8 eV originating from singlet and triplet species, respectively. In this manner, the relative intensity of the spectral features resulting from singlet He* excitation can be quantified to be about 6 %, in agreement with reports from another MIES source.[19]

It is instructional to note that there is a difference of 0.8 eV between the positions for the Na3s peak in the first spectrum revealing AD and in spectra with larger amounts of sodium. In the latter ones, the shifted emission appears as a small addition next to the main peak. Assuming that the empty 2s level in singlet He* is energetically lower than the one of the triplet state, the autodetachment with He*(2^1S) is expected to start at lower binding energy relative the one for He*(2^3S) at lower Na coverage.

Singlet metastable atoms can effectively be eliminated by illumination of the atom beam with light of a wavelength of 58.4 nm as it has been demosntarted elsewhere.[10] Although, our apparatus would easily allow the installation of a He*(2^1S) quenching lamp, we have not implemented this as, so far, spurious emission from He*(2^1S) never hindered the quantitative analysis of MIES spectra.

VII. CONCLUSION

The MIES source introduced here is optimized for the measurements on solid surfaces where the double discharge operation greatly enhances the electron yield for MIES compared to single discharge operation and enables us to collect high resolution spectra within a short time. The compact design combines stable operation with a minimum in effort for maintenance. The beam of metastable atoms consists not only of He*(2^3S) but has a 6% contribution of He*(2^1S) appearing as a spurious signal in spectra. However, this does not affect the quantitative interpretation of MIES results and, if required, it could easily be removed by installing a suitable light source. The discharges, furthermore, generate HeI ultraviolet photons with a flux strong enough to be used for UPS measurements. Installing a time-of-flight module facilitates the quasi-simultaneous collection of MIES and UPS where UPS spectra contain a residual MIES signal that can be minimized to a contribution of 1 to 3% of the MIES intensity.

ACKNOWLEDGMENT

The authors are grateful to the Deutsche Forschungsgemeinschaft for financial support through the project BO 3349/2-1.

References

1. H. Hotop, E. Kolb and J. Lorenzen, J. Electron. Spectrosc. Relat. Phenom. **16**, 213 (1979).
2. S. Kudo, N. Kishimoto and K. Ohno, J Phys Conf **235**, 012012 (2010).
3. H. Morgner, Adv. Atom. Mol. Opt. Phys. **42**, 387 (2000).
4. O. Höfft, U. Kahnert, S. Bahr and V. Kempter, J. Phys. Chem. B **110**, 17115 (2006).
5. O. Höfft, S. Bahr, M. Himmerlich, S. Krischok, J. A. Schaefer and V. Kempter, Langmuir **22**, 7120 (2006).
6. Y. Harada, S. Masuda and H. Ozaki, Chem. Rev. **97**, 1897 (1997).
7. A. Borodin and M. Reichling, Phys. Chem. Chem. Phys. **13**, 15442 (2011).
8. S. Krischok, J. A. Schaefer, O. Hofft and V. Kempter, Surf. Interface Anal. **37**, 83 (2005).
9. W. Maus-Friedrichs, M. Wehrhahn, S. Dieckhoff and V. Kempter, Surf. Sci. **237**, 257 (1990).
10. K. Ohno, T. Takami, K. Mitsuke and T. Ishida, J. Chem. Phys. **94**, 2675 (1991).
11. M. J. Verheijen, H. C. W. Beijerinck, L. H. A. M. van Moll, J. Driessen and N. F. Verster, J. Phys. E Sci. Instrum. **17**, 904 (1984).
12. K. Mitsuke, T. Takami and K. Ohno, J. Chem. Phys. **91**, 1618 (1989).
13. W. Maus-Friedrichs, M. Frerichs, A. Gunhold, S. Krischok, V. Kempter and G. Bihlmayer, Surf. Sci. **515**, 499 (2002).
14. W. Maus-Friedrichs, S. Dieckhoff and V. Kempter, Surf. Sci. **249**, 149 (1991).
15. W. Maus-Friedrichs, S. Dieckhoff, M. Wehrhahn and V. Kempter, Surf. Sci. **253**, 137 (1991).
16. A. Borodin, O. Höfft, U. Kahnert, V. Kempter, S. Krischok and M. O. Abou-Helal, J. Chem. Phys. **120**, 5407 (2004).
17. A. Borodin, O. Höfft, U. Kahnert, V. Kempter and A. Allouche, Vacuum **73**, 15 (2004).
18. A. Borodin, O. Höfft, S. Krischok and V. Kempter, Nucl. Instrum. Meth. B **203**, 205 (2003).
19. H. Ferkel, R. Feltgen and D. Pikorz, Rev. Sci. Instrum. **62**, 2626 (1991).
20. W. S. Taylor, J. G. Dulak and S. N. Ketkar, J. Am. Soc. Mass. Spectrom. **1**, 448 (1990).
21. O. Dyachenko, N. Diek, Y. Shapiro, R. Tamang, W. Harneit, M. Reichling and A. Borodin, Chem. Phys. Lett. **640**, 72 (2015).
22. G. H. Enevoldsen, H. P. Pinto, A. S. Foster, M. C. R. Jensen, A. Kühnle, M. Reichling, W. A. Hofer, J. V. Lauritsen and F. Besenbacher, Phys. Rev. B **78**, 045416 (2008).
23. H. H. Pieper, K. Venkataramani, S. Torbrügge, S. Bahr, J. V. Lauritsen, F. Besenbacher, A. Kühnle and M. Reichling, Phys. Chem. Chem. Phys. **12**, 12436 (2010).
24. S. Krischok, O. Hofft and V. Kempter, Nucl. Instrum. Meth. B **193**, 466 (2002).
25. S. Munnix and M. Schmeits, Phys. Rev. B **30**, 2202 (1984).
26. S. Wendt, P. T. Sprunger, E. Lira, G. K. H. Madsen, Z. S. Li, J. Ø. Hansen, J. Matthiesen, A. Blekinge-Rasmussen, E. Lægsgaard, B. Hammer and F. Besenbacher, Science **320**, 1755 (2008).
27. C. M. Yim, C. L. Pang and G. Thornton, Phys. Rev. Lett. **104**, 036806 (2010).
28. M. Brause, S. Skordas and V. Kempter, Surf. Sci. **445**, 224 (2000).
29. C. Di Valentin, G. Pacchioni and A. Selloni, Phys. Rev. Lett. **97**, 1666803 (2006).
30. C. Di Valentin, G. Pacchioni and A. Selloni, J. Phys. Chem. C **113**, 20543 (2009).

31. S. Hongo, S. Saito, T. Urano and T. Kanaji, Surf. Sci. **287**, 588 (1993).

4.2. Effect of doping diamond on the near- surface electronic structure

In this part experimental results comprises surface spectroscopy studies on different doping types diamond surfaces is presented. Understanding of fundamental principles of the donor and acceptor impurities is crucial for diamond surface studies. However, this hardly could be found in literature accessible in clear comprehensible way and detailed physics explanation usually mixed up or absent.

Samples measured by means of XPS, UPS and MIES spectroscopy reveal the core shell level and band gap structures of nitrogen and boron doped samples, as well as HOPG graphite reference sample. Detailed explanation of the carbon C1s core shell peak shift physics is proposed and the origin of doping effect is introduced.

Effect of doping diamond on the near- surface electronic structure

O. Dyachenko,[a)] M. Reichling,[a)] A. Borodin
Fachbereich Physik, Universität Osnabrück, Barbarastr. 7, 49076 Osnabrück, Germany

XPS surface measurements of differently doped diamond samples, namely with predominant nitrogen doping and predominant boron doping and graphite are reported and discussed in a comparative analysis. This analysis is supplemented by results from UPS and MIES measurements to derive energy band diagrams summarizing all acquired spectroscopy data. As the main feature explaining XPS data, we identify the shift in the Fermi level upon introducing doping atoms in small concentration. Based on the results from the combined surface spectroscopy studies, an indirect method of diamond doping determination and categorization for different diamond doping is suggested.

PACS
81.05.U- carbon/carbon-based materials
68.35.-p solid surfaces and solid-solid interfaces: structure and energetics
79.60.-i photoemission and photoelectron spectra

Keywords:
diamond, C(100), X-ray photoelectron spectroscopy, band structure, XPS, Ultraviolet photoelectron spectroscopy, UPS, Metastable impact electron spectroscopy, MIES, diamond doping, diamond etching, annealing in molecular oxygen, Auger spectroscopy, nitrogen implantation

[a)] Electronic mail: odyachen@uos.de, reichling@uos.de

Nowadays diamond used in many applications due to its remarkable properties. Some of the already demonstrated applications are quantum computing applications [1-3], electrochemical applications [4, 5], bio materials based on detonation nanodimond (ND) and polymers for bone implants [6], drug delivery by surface functionalized ND[7, 8], high power electronic devices [9, 10] and photonic applications [11]. For all of this applications, a fundamental understanding and control of the surface state, doping level and phase purity is of importance. One of the frequently used tools for surface studies is X-ray photoelectron spectroscopy (XPS) allowing to perform in-depth analysis in the range of a few nanometers. XPS provides core shell information, elemental composition and chemical composition by careful core shell peaks analysis, as well as Auger lines information.

Characterization of B-doped and N-doped diamond clean, oxidized and hydrogen terminated surfaces with regard to optical properties,[12] mechanical properties,[13] electrical and thermal conductivity properties[13, 14] as well as surface morphology and topography[15] has been reported in various context. Specifically, there are a number of publications reporting on X-ray photoelectron spectroscopy (XPS)[16-19], low-energy electron diffraction (LEED),[20, 21] high resolution electron energy loss spectroscopy (HREELS),[22] ultraviolet photoelectron spectroscopy (UPS),[23, 24] angle-resolved photoelectron spectroscopy (ARPES)[20] and metastable impact electron spectroscopy (MIES)[25]. However, one of the main features like the carbon C1s peak position determined by XPS analysis on differently doped diamond still appears to be controversial. Kono et al .[26] studied the diamond C1s carbon peak shift for n-type phosphorous doped and p-type boron doped hydrogen terminated reference samples. Theoretical calculations predict a shift of the Fermi energy E_F for different types of diamond doping.[27] It has been demonstrated in theoretical studies that the position of the Fermi level is strongly dependent on the dopant type, for instance, nitrogen (N-doping) or boron doping (B-doping) and their concentration.[28] It is also well known that nitrogen incorporated in diamond acts as a donor, and leads to n-type conductivity while boron acts as an acceptor and results in a p-type conductivity of diamond.

The carbon C1s sp^2 peak position is well known for graphite and amorphous carbon, reported in literature[17, 29, 30] to be in the binding energy (E_B) range 284.4 - 284.8 eV while for diamond, various positions of C1s sp^3 peak have been reported in literature[16, 22, 26, 31-33] covering the wide range from E_B = 284.2 eV to 288.0 eV. Also a C1s peak shift upon nitrogen doping has been demonstrated.[34, 35]

To clarify the ambiguity in the diamond carbon core shell peak position and to elucidate the reason of the ambiguity found in literature, we performed careful XPS studies on different diamond surfaces and on a HOPG graphite surface. This work reports on combined XPS, UPS and MIES measurements on surfaces of different predominant nitrogen doping concentration, predominant boron doping and graphite.

We investigate synthetic IIa diamond, so it is important to mention that during the CVD growth, a small amount of nitrogen will be always present, at least it is in the ppb range. At the same time, we need to be very careful analyzing IIa synthetic CVD and HPHT diamonds, because together with nitrogen, some minor boron concentration will also be present, a fact that has often not been taken care of.

For any study in this field, it is most important to clarify whether the diamond has a predominant boron dopant concentration, or a predominant nitrogen concentration, or both dopants are present in similar concentrations.

Here, we present XPS, UPS and MIES measurements for CVD (100) IIa N-doped diamond having a nitrogen content of 5 ppb, HPHT Ib N-doped diamond having a nitrogen content around 200 ppm, as well as IIb (111) B-doped having a boron concentration of 100ppm in comparison to a HOPG graphite sample. Results of XPS measurements are

compared to each other and supplemented with UPS and MIES measurements yielding work functions and other near surface information.

For this study, we use a type IIa CVD grown electronic grade sample with a dopant content N < 5 ppb and B < 1 ppb, IIa CVD diamond sample with a dopant content N < 1 ppm and B < 0.05 ppm, a size of 3.0 x 3.0 x 0.5 mm^3 and (100) surface orientation as well as Ib HPHT diamond with a dopant content of N < 200 ppm, B < 0.1 ppm a size of 4.5 x 4.5 x 0.3 mm^3, all samples manufactured by E6 (Element Six Ltd., Ascot, United Kingdom). The manufacturer performs mechanical polishing yielding a surface roughness of typically Ra < 30 nm for IIa N < 1 ppm, Ra < 5 nm for IIa N < 5 ppb and Ra < 10 nm for one polished side Ib sample followed by boiling in a strongly oxidizing acid solution composed of H_2SO_4 and KNO_3. The third diamond sample is a boron doped IIb type sample with (111) orientation and a predominant boron concentration of ~ 100 ppm (Fraunhofer, IAF, Freiburg, Germany) with the surface treated by mechanical polishing and boiling in a strongly oxidizing acid solution composed of H_2SO_4 : HNO_3 for 1 hour, 30 minutes at 250° C supplied by IAF. The nitrogen concentration for the IIb type sample is not specified by manufacture, however, as we clearly find a boron Auger line in XPS but the nitrogen line is completely absent, we consider the sample as predominantly boron doped with a negligible concentration of nitrogen. All diamond samples are single crystalline. As a reference for sp^2 binding, we use a standard sample HOPG 0.8° having dimensions of 12.0 x 12.0 x 1.0 mm^3.

After transferring the diamond samples into the UHV chamber having a base pressure below $8 \cdot 10^{-11}$ mbar, the laboratory treatment for diamond samples comprises flashing to a temperature of 790°C for 3 minutes to remove volatile adsorbed species like water and hydrocarbons. The HOPG sample is argon sputtered at 500 eV for 5 minutes and annealed up to about 400°C. All subsequent preparation steps and further measurements are performed in-situ in the UHV.

The samples are analyzed by a XPS apparatus consisting of a X-ray source XR 50 (SPECS Surface Nano Analysis GmbH, Berlin, Germany) and a hemispherical electron energy analyzer PHOIBOS 100 (SPECS Surface Nano Analysis GmbH, Berlin, Germany) equipped with a five channeltron assembly detector maintaining a high detection sensitivity at an energy resolution of 0.2 eV. Photoelectron spectra are taken using non-monochromatic radiation from the Mg K-α line with a photon energy of 1253.6 eV. The source has been calibrated with a clean gold sample and reveals a peak position for Au 4f7 = 84.00 eV. The X-rays are directed onto the sample surface under an angle of 30° while electrons emitted perpendicular from the surface are collected by the transfer optics of the electron analyzer. The setup further equipped with a homebuilt He plasma source, producing photons with an energy of 21.2 eV and metastable helium atoms He*(2^3S) =19.82 eV. The metastable beam consists mostly of triplet He*(2^3S) generating MIES spectra. To improve the performance for collecting very low energy electrons, a bias of -15 V is applied to the sample during MIES and UPS measurements.

To avoid possible charging effects, diamond samples are heated to 350°C during XPS and to 450°C during UPS and MIES measurements as it has been shown earlier that heating above 400°C even on a clean diamond, the surface will gain sufficient conductivity to compensate for the impact related electron current.[31] The absence of charging is checked for each experiment by tracking the positions of the oxygen O1s and the calcium Ca2p peaks where we do not observe any significant peak shift. Survey spectra of all samples after the initial cleaning step are shown in Fig. 1(a).

The presence of the oxygen core-level O 1s peak indicates a partial oxidation of the surface and is associated to a surface chemisorbed oxygen species. The minute signal of the Ta 4d line is due to emission from the Ta sample holder assembly while the origin of a small

Ca signal present in almost all spectra is not clear; we suspect a contamination from trace impurities in surface cleaning agents applied after mechanical polishing.

The most evident feature is a shift of the C1s peak related to the presence of nitrogen or boron at the diamond surface and in sub-surface layers and that we attribute to a shift in the Fermi level relative to the initial carbon peak position.[28] To interpret the XPS spectra, we recall that the energy difference between the valence band (VB) edge and the carbon C1s core shell peak has been reported to be 283.9 ± 0.1 eV in the literature for a single crystal (100) diamond.[36] The carbon C1s peak region for all investigated samples is presented in Fig. 1(b). For the IIa diamond sample N < 1 ppm and B < 0.05 ppm, the carbon peak marked as sp^3 with a binding energy position of E_B = 285.4 eV corresponds to a reported of E_B = 285.5 eV value for pure sp^3 diamond.[33] For the Ib HPHT diamond with doping levels of N < 200 ppm and B < 0.1 ppm marked as N:sp^3, the C1s peak corresponds to E_B = 287.2 eV, for the boron doped B:sp^3 with B ~ 100 ppm, the peak is found at E_B = 284.6 eV and for the HOPG sample, the peak appears at E_B = 284.8 eV. As will be argued in detail below, the different binding energy (E_B) values arise from the shift in E_F from the mid band gap – intrinsic position, due to the doping impact, resulting in the n-type E_F(N) level formation for nitrogen doping and p-type E_F(B) level formation in case of boron doping.

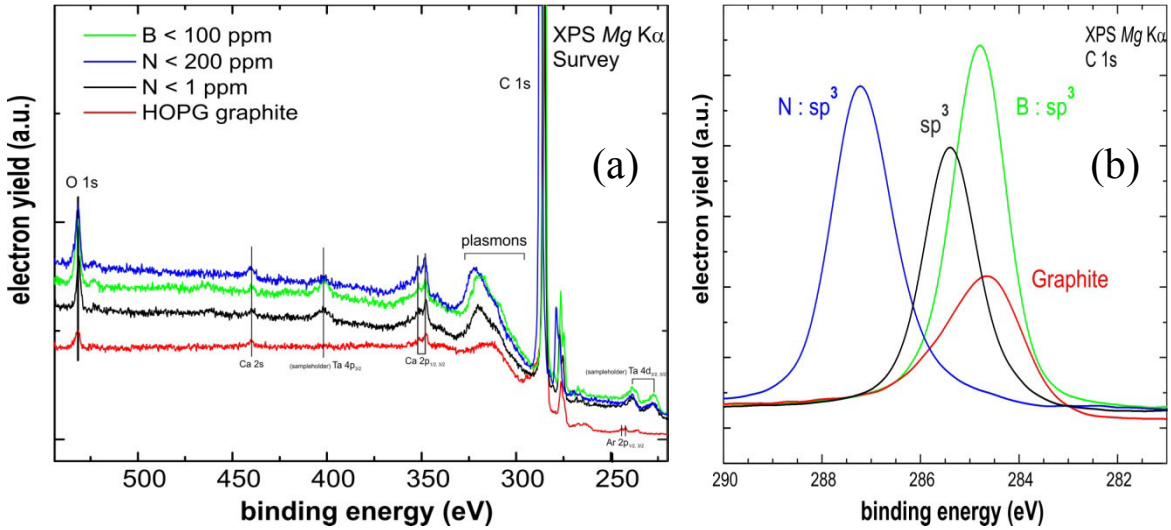

Fig.1 (a) Survey XPS spectra and (b) carbon C1s peak region of nitrogen doped, boron doped and graphite samples.

While the interpretation of XPS result provides the basic framework for describing the electronic structure of doped diamond, more detailed information about the valence band structure and values for the work function (WF) of the systems are needed to develop a complete picture of the surface and near-surface electronic structure. Therefore, we performed complementary ultraviolet photoelectron spectroscopy (UPS) and metastable impact electron spectroscopy (MIES) studies. The combination of the methods allows for probing the electronic structure in different layers; while MIES is sensitive to processes in the very first surface layer, UPS has a larger probing depth that is comparable to the one for the XPS studies. UPS measurements shown in Fig. 2 yield work function values WF_B = 3.72 eV for B-doped diamond, WF_N = 3.72 eV for 200 ppm N-doped diamond and WF_{Ni} = 3.92 eV

for the 1 ppm N-doped diamond. As revealed by the spectra obtained after background substration shown in Fig. 3, the bulk C(2p) state as observed by UPS for 200 ppm nitrogen doped diamond is shifted by 0.72 eV relative to the C(2p) state of the 1 ppm nitrogen doped sample while the boron doped sample exhibits a shift of 0.47 eV. MIES reveals for the WF same values for B-doped and for 200 ppm N-doped diamond samples, namely $WF_N = WF_B =$ 3.76 eV while we find $WF_{Ni} = 3.83$ eV for 1 ppm N-doped diamond. The WF difference between UPS and MIES is very small, thus ,we conclude that there is no significant surface band bending.

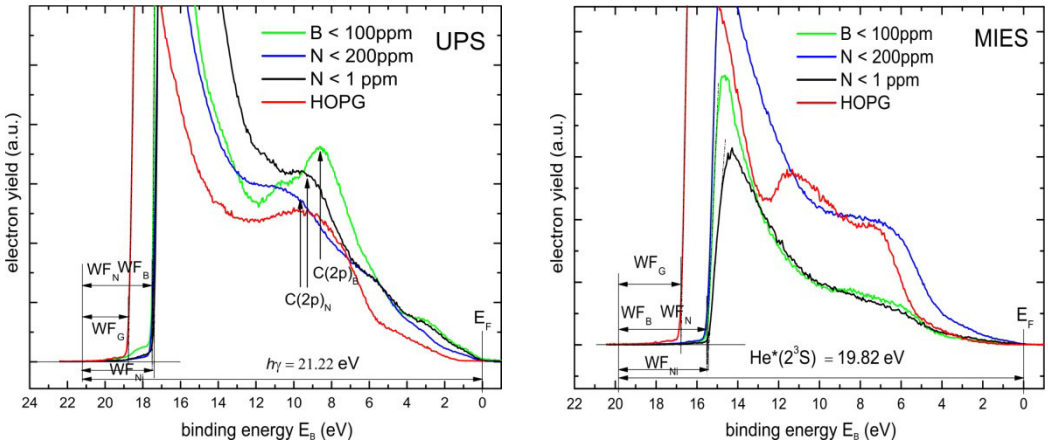

Fig. 2 UPS and MIES of nitrogen doped, boron doped and graphite revealing WF.

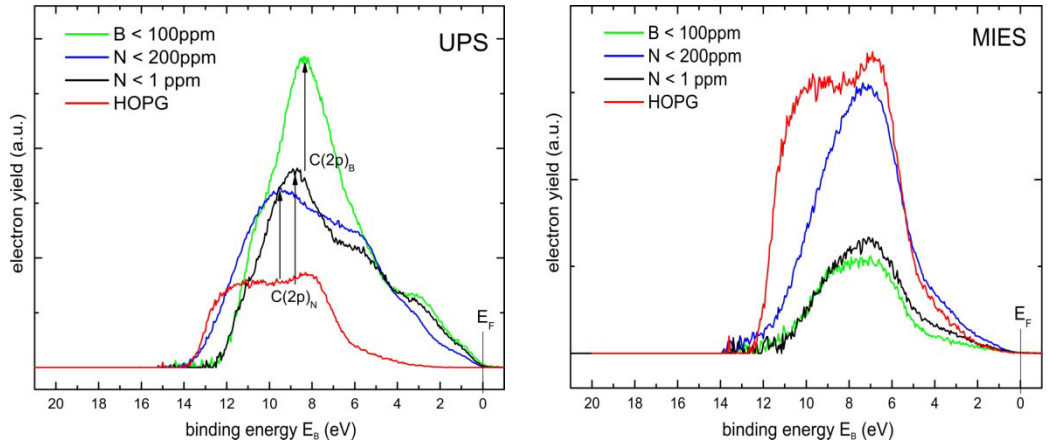

Fig. 3 UPS and MIES background subtracted of nitrogen doped, boron doped and graphite.

Combining results from UPS, MIES and XPS measurements, we draw energy band diagrams shown in Fig. 4 for the B-doped and N-doped diamond surfaces. To draw the band diagrams, we use results of calculations predicting the nitrogen donor level being located

1.7 eV below the conduction band minimum (CBM) and the boron acceptor level being positioned 0.37 eV above the valence band maximum (VBM).[28]

It is important to note that the binding energy levels denoted by E_B are given relative to the Fermi-level (E_F) of the solid, rather than the vacuum level. This is due to the peculiarities of the electron spectroscopic measurement where both, the analyser and the sample are electrically grounded and, therefore, their Fermi levels are aligned. The electron analyser work function has been determined via standard calibration procedures to be WF_{sp} = 4.23 eV by standard procedures described elsewhere.[35] To precisely resolve the low-energy cut-off in the electron spectra and to avoid possible irregularities of the analyser transmission function for electrons with low kinetic energies in valence band spectra, we apply an accelerating bias voltage of Ub = 15.00 V between the sample and the analyser entrance optics. Therefore, E_B is calculated from the known parameters of the experiment and the retarding voltage U_r as

$$E_B = \{E_{exc} + eU_b - WF_{sp} - E_p\} - eU_r$$

where E_{exc} is the excitation energy, either $E(He^*)$ = 19.82 eV for MIES, X-ray *hv* energy, or *hv* (HeI) = 21.2 eV for UPS, while *e* denotes the elementary electron charge. As electron spectra, we plot the electron yield signal as a function of E_B.

Thus, as long EB of the photoelectrons is directly linked to E_F, the shift of the E_F due to the sample doping will lead to the shift of E_B of the photoelectron peaks, namely the carbon C1s peak position in XPS spectra as observed in Fig. 1(b).

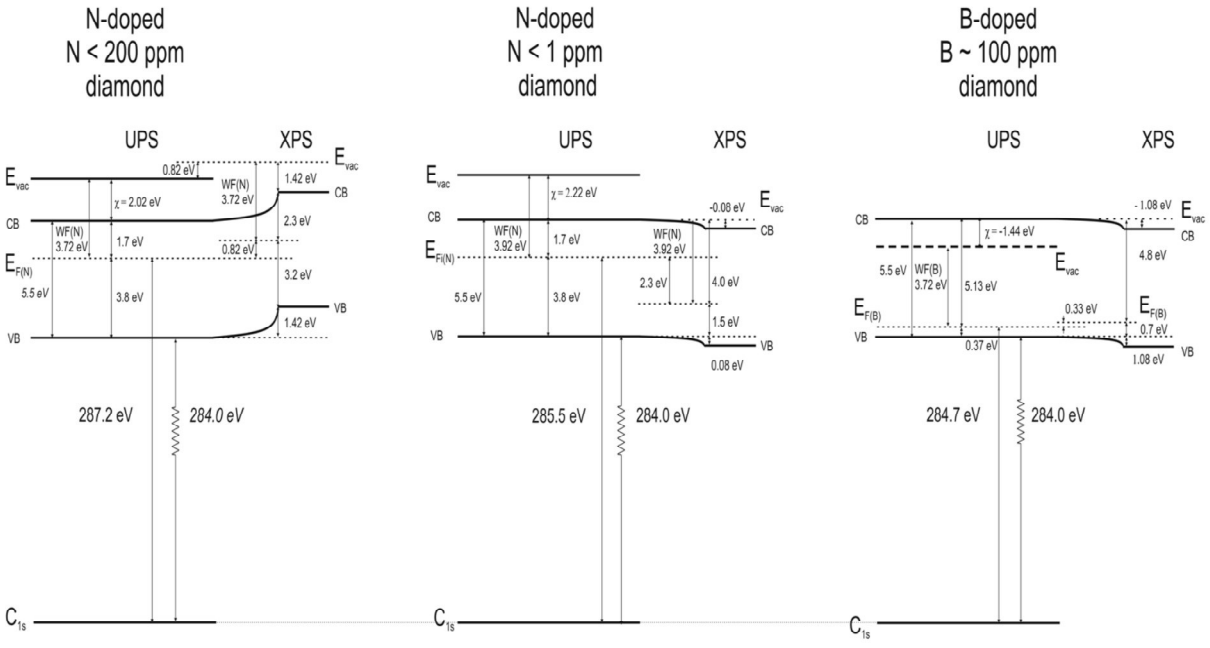

Fig. 4 Band diagram for N-doped 1 ppm, 200 ppm and B-doped 100 ppm diamond.

This insight allows us to interpret earlier measurements where we found that doping of diamond with nitrogen results in a shift of the carbon C1s peak towards higher energies.[35] In the respective work, a IIa type CVD diamond (Element Six Ltd., Ascot, United Kingdom) with the concentrations N < 1 ppm and B < 0.05 ppm was subjected to a cyclic surface preparation comprising initial sample flashing and nitrogen sputtering, using a conventional sputter gun (30 seconds, 500 eV ion energy). Here, we repeat and extend such measurements and track the nitrogen concentration via the nitrogen Auger NKLL line during each step of surface treatment. It should be noticed that nitrogen is implanted in a concentration below 1 at.% but clearly identified from Auger NKLL electron emission. Nitrogen ion sputtering results in nitrogen implantation but also a partial destruction of the surface atomic structure as well as sp^2 bond formation. To remove the graphitic material, the sample is annealed in molecular O_2 oxygen (Messer Griesheim GmbH, Krefeld, Germany, O_2 purity better than 99.998 %) at a pressure of 1.33×10^{-7} mbar in the UHV for overall 27 hours. Finally, the sample is etched in a 1:1:1 acid mixture of H_2SO_4, HNO_3 and $HClO_4$ for 4 hours at a temperature of 360° C and rinsed with Milli-Q water of type I. The sample surface is analysed by XPS after each treatment step. Figure 5 shows XPS measurements of the C1s peak with its initial position at E_B = 285.7 eV. The magenta line demonstrates a strong shift of the main C1s peak position to E_B = 286.9 eV as a result of nitrogen doping, a position that is close to the one found for the HPHT N < 200 ppm diamond sample (see peak position at 287.2 eV in Fig. 1(a)). In the previous paper,[35] a deconvolution procedure of the carbon C1s peak has been developed that allows to extract the main components for the peak apparent for the different sample states. This offers the possibility to extract the relative intensity of the main components and to track them as a function of time or processing steps.
For instance the middle component (magenta line in the Fig. 5) related to undamaged diamond sp^3 component at E_B = 285.5 eV and the lower energy slope related to the sp^2 component at E_B = 284.5 eV, increased due to nitrogen implantation. It is found that after 12 hours annealing in oxygen, the C1s peak position is shifted back to the initial position and the N1s photoelectron peak completely vanishes, clearly indicating the removal of implanted nitrogen. However, even after this very long etching time, there is a residual shift due to nitrogen implantation. The attendant rise of the sp^2 peak is a result of a chemical modification often described as surface amorphisation. Subsequent attempts to remove the residual implanted nitrogen by increasing the annealing temperature result in further amorphization but not the desired removal of nitrogen. The last annealing step at T = 890° C revels an asymmetrical curve shape, similar to the one obtained for HOPG signal indicating complete surface amorphization.

However, the last preparation step of wet chemical treatment in the strongly oxidising acid mixture allows us to completely remove nitrogen and to reconstitute a clean surface with a high sp^3 phase purity. After sample re-transfer to the UHV and flashing to a temperature of 790°C, XPS measurements reveal a nearly perfect C 1s peak at the sp^3 position of E_B = 285.8 eV while the nitrogen Auger NKLL signal is below the detection limit.

To compare effect of nitrogen plasma implantation/sputtering to nitrogen sputtering effects, another sample from the same batch is treated with a usual Ar^+ sputtering procedure. The dashed pink line in the Fig. 5 denotes the result for Ar^+ sputtering for 60 seconds in the unfocused beam at 1 keV ion energy. This initially leads to a split peak representing the initial sp^3 peak at $E_B = 285.5$ eV and the rising sp^2 component at $E_B = 284.5$ eV induced by the argon impact. Due to the large ionic radius of argon molecules, sputtering leads only to surface amorphization but not to implantation in the diamond surface.

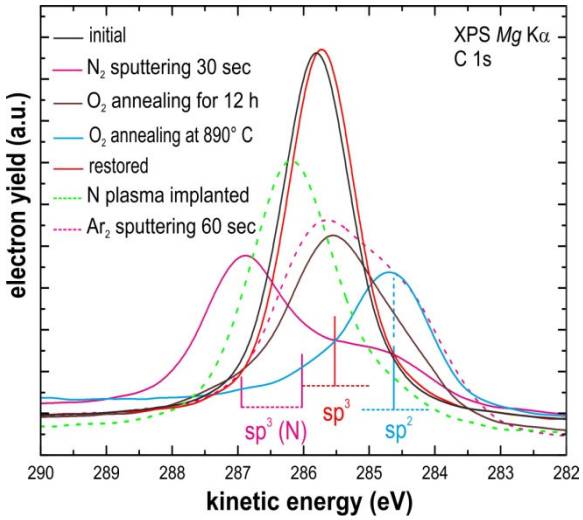

Fig. 5 C1s carbon peak region of nitrogen N < 1 ppm samples nitrogen implanted from a plasma source and after nitrogen and Ar sputtering.

These experiments demonstrate that the C1 s peak position is directly related to the diamond dopant concentration. It is important to note that the shift is coupled to the Fermi level shift and is not a chemical shift what is evident from the very low nitrogen concentration that could barely be noticed as a chemical shift.

The diagram of in Fig. 6 shows the relation between the three main components during d annealing diamond in molecular oxygen. From this diagram, one can follow the development of components versus etching time and deduce diamond surface etching rates.

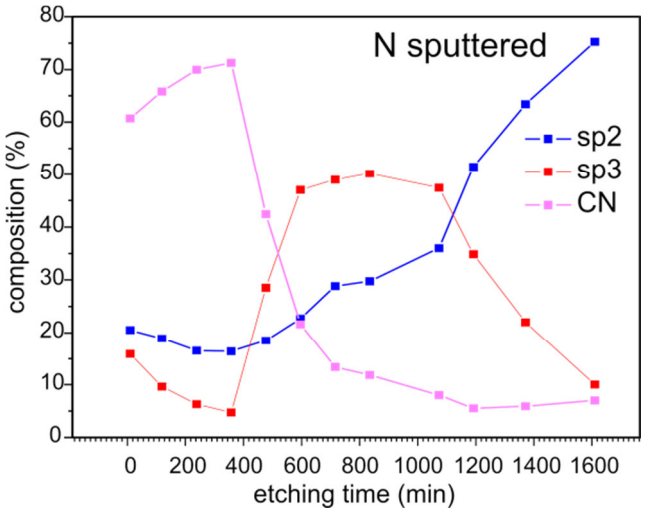

Fig. 6 The diamond surface etching rate during annealing in oxygen.

Combining results from all spectroscopic studies, we develop a general model describing etching of a nitrogen implanted diamond surface via annealing in oxygen as illustrated in Figure 7 illustrating the depth of damaged diamond surface layers. The initial step represents the diamond surface direct after nitrogen implantation. The following annealing in oxygen leads to the removal of the surface top amorphous sp^2 layers. In the Figure 7 state "A" illustrates the surface after 6 h of annealing in oxygen, when the sp^3(N) layer is dominating. Further state "B" reveals removal of the nitrogen implanted layer, but still this component is dominant. After 12 h of treatment, see "C", most part of the implanted nitrogen associated with sp^3(N) component has been removed. This is confirmed by the main peak position shift, related to diamond sp^3 component, and the peak shape. Additional annealing of the diamond at elevated temperature 890° C results only in a rise of the sp^2 intensity, that is interpreted as further amorphization.

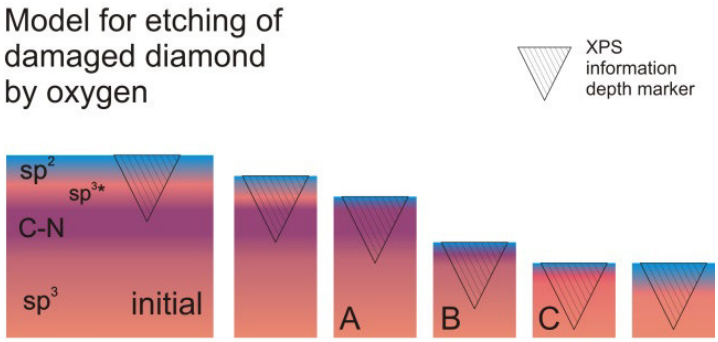

Fig. 7 Diagram illustrating etching of the damaged diamond surface layer by oxygen.

By consecutive acids treatment step, the initial surface state even for strong surface amorphization can be recovered and this allows the re-use the specimen for further implantation experiments. However, even after 12 h annealing in oxygen in UHV, nitrogen containing layers are almost completely etched away.

References

[1] T. D. Ladd, F. Jelezko, R. Laflamme, Y. Nakamura, C. Monroe, and J. L. O'Brien, Nature **464**, 45 (2010).

[2] J. Wrachtrup, and F. Jelezko, J. Phys.: Condens. Matter **18**, S807 (2006).

[3] R. J. Epstein, F. M. Mendoza, Y. K. Kato, and D. D. Awschalom, Nature Physics **1**, 94 (2005).

[4] H. Zanin, P. W. May, D. J. Fermin, D. Plana, S. M. C. Vieira, W. I. Milne, and E. J. Corat, ACS Appl. Mater. Interfaces **6**, 990 (2014).

[5] J. V. Macpherson, Phys. Chem. Chem. Phys. **17**, 2935 (2015).

[6] Z. Xing, T. O. Pedersen, X. J. Wu, Y. Xue, Y. Sun, A. Finne-Wistrand, F. R. Kloss, T. Waag, A. Krueger, D. Steinmuller-Nethl, and K. Mustafa, Tissue Eng. **19**, 1783 (2013).

[7] I. Rehor, J. Slegerova, J. Kucka, V. Proks, V. Petrakova, M. P. Adam, F. Treussart, S. Turner, S. Bals, P. Sacha, M. Ledvina, A. M. Wen, N. F. Steinmetz, and P. Cigler, Small **10**, 1106 (2014).

[8] E. K. Chow, X. Q. Zhang, M. Chen, R. Lam, E. Robinson, H. J. Huang, D. Schaffer, E. Osawa, A. Goga, and D. Ho, Sci. Trans. Med. **3**, 73ra21 (2011).

[9] H. Umezawa, T. Matsumoto, and S. I. Shikata, IEEE Electron Device Lett. **35**, 1112 (2014).

[10] T. Iwasaki, Y. Hoshino, K. Tsuzuki, H. Kato, T. Makino, M. Ogura, D. Takeuchi, T. Matsumoto, H. Okushi, S. Yamasaki, and M. Hatano, Appl. Phys. Express **5**, 091301 (2012).

[11] P. Rath, S. Ummethala, S. Diewald, G. Lewes-Malandrakis, D. Brink, N. Heidrich, C. Nebel, and W. H. P. Pernice, Appl. Phys. Lett. **105**, 251102 (2014).

[12] A. Gruber, A. Drabenstedt, C. Tietz, L. Fleury, J. Wrachtrup, and C. von Borczyskowski, Science **276**, 2012 (1997).

[13] R. S. Sussmann, *CVD Diamond for Electronic Devices and Sensors* (John Wiley & Sons, Ltd, 2009).

[14] J. A. Garrido, T. Heimbeck, and M. Stutzmann, Phys. Rev. B **71**, 245310 (2005).

[15] M. Nimmrich, M. Kittelmann, P. Rahe, A. J. Mayne, G. Dujardin, A. v. Schmidsfeld, M. Reichling, W. Harneit, and A. Kühnle, Phys. Rev. B **81**, 201403R (2010).

[16] V. S. Smentkowski, H. Jänsch, M. A. Henderson, and J. T. Yates, Surf. Sci. **330**, 207 (1995).

[17] F. R. McFeely, S. P. Kowalczy, L. Ley, R. G. Cavell, R. A. Pollak, and D. A. Shirley, Phys. Rev. B **9**, 5268 (1974).

[18] J. F. Morar, F. J. Himpsel, G. Hollinger, J. L. Jordan, G. Hughes, and F. R. Mcfeely, Phys. Rev. B **33**, 1340 (1986).

[19] J. I. B. Wilson, J. S. Walton, and G. Beamson, J. Electron. Spectrosc. Relat. Phenom. **121**, 183 (2001).

[20] F. Maier, R. Graupner, M. Hollering, L. Hammer, J. Ristein, and L. Ley, Surf. Sci. **443**, 177 (1999).

[21] R. Graupner, F. Maier, J. Ristein, L. Ley, and C. Jung, Phys. Rev. B **57**, 12397 (1998).

[22] T. Haensel, J. Uhlig, R. J. Koch, S. I. U. Ahmed, J. A. Garrido, D. Steinmüller-Nethl, M. Stutzmann, and J. A. Schaefer, Phys. Status Solidi A **206**, 2022 (2009).

[23] L. Diederich, O. Küttel, P. Aebi, and L. Schlapbach, Surf. Sci. **418**, 219 (1998).

[24] P. K. Baumann, and R. J. Nemanich, Surf. Sci. **409**, 320 (1998).

[25] S. Dieckhoff, D. Ochs, J. Gunster, and V. Kempter, Surf. Sci. **423**, 53 (1999).

[26] S. Kono, K. Mimochi, G. Takyo, T. Goto, T. Abukawa, and T. Aoyama, New Diamond Front. Carb. Techn. **17**, 231 (2007).
[27] K. Kobashi, Cornell University, Preprint Archive, Materials Science, arXiv:1406.6204 (2014).
[28] A. T. Collins, J. Phys.: Condens. Matter **14**, 3743 (2002).
[29] P. A. Brühwiler, A. J. Maxwell, C. Puglia, A. Nilsson, S. Anderson, and N. Mårtensson, Phys. Rev. Lett. **74**, 614 (1995).
[30] D. N. Belton, and S. J. Schmieg, J. Vac. Sci. Technol. A **8**, 2353 (1990).
[31] L. Diederich, O. M. Küttel, P. Ruffieux, T. Pillo, P. Aebi, and L. Schlapbach, Surf. Sci. **417**, 41 (1998).
[32] S. Ferro, M. Dal Colle, and A. De Battisti, Carbon **43**, 1191 (2005).
[33] J. Chastain, and J. F. Moulder, *Handbook of X-Ray Photoelectron Spectroscopy: A Reference Book of Standard Spectra for Identification and Interpretation of XPS Data* (Physical Electronics Division, Perkin-Elmer Corporation, 1992).
[34] I. Kusunoki, Y. Igari, S. Ishidzuka, T. Takami, T. Takaoka, M. Nishitani-Gamo, and T. Ando, Diam. Relat. Mater. **10**, 1676 (2001).
[35] O. Dyachenko, N. Diek, Y. Shapiro, R. Tamang, W. Harneit, M. Reichling, and A. Borodin, Chem. Phys. Lett. **640**, 72 (2015).
[36] F. Maier, J. Ristein, and L. Ley, Phys. Rev. B **64**, 165411 (2001).

4.3. Cyclic preparation of diamond (100) with perfect phase purity

In terms of the “Quantum computing” project to generate controllable arrays of nitrogen vacancy (NV) centers nitrogen implantation is required. It has been demonstrated in the previous session that “as grown” nitrogen doped diamonds reveal significant shift of the carbon C1s core shell peak. In this part experimental results comprises nitrogen implantation, etching in oxygen and wet chemical etching are presented.

A successful nitrogen doping confirmed by means of XPS. It is demonstrated that the nitrogen flux induce the damage to the diamond surface and further how perfect phase purity diamond (100) surface could be restored repeatedly from one sample by a certain preparation procedure cycle. A deconvolution procedure revealing the coexistence of sp^3 and sp^2 bonding and allowing track of the diamond surface phase purity during the treatment is introduced.

A diamond (100) surface with perfect phase purity

Oleksiy Dyachenko,[1,a)] Nadine Diek,[1,2] Yevgeniy Shapiro,[3] Rajesh Tamang[1], Wolfgang Harneit,[3] Michael Reichling,[1,a)] Andriy Borodin[1]

[1]*Fachbereich Physik, Universität Osnabrück, Barbarastr. 7, 49076 Osnabrück, Germany*
[2]*Institut für Chemie neuer Materialien, Barbarastr. 7, 49076 Osnabrück, Germany*
[3]*Institut für Physikalische Chemie, Johannes Gutenberg Universität Mainz, Duesbergweg 10 – 14, 55099 Mainz, Germany*

Diamond surfaces with (100) orientation and perfect phase purity regarding the coexistence of sp^3 and sp^2 bonding as well as near surface nitrogen implanted layers are repeatedly produced from one sample by a cycle of nitrogen implantation, etching in oxygen and wet chemical etching. Comprehensive surface studies carried out by X-ray photoelectron spectroscopy involving a deconvolution of the C1s peak into contributions of C sp^3, C sp^2 and C sp^3(N) reveal the surface and near-surface phase and stoichiometry. It is demonstrated that efficient etching of nitrogen implanted diamond occurs by high temperature annealing in oxygen and a wet chemical treatment.

PACS

81.05.U-	carbon/carbon-based materials
68.35.-p	solid surfaces and solid-solid interfaces: structure and energetics
79.60.-i	photoemission and photoelectron spectra

Keywords:
diamond, C(100), X-ray photoelectron spectroscopy, XPS, diamond etching, annealing in molecular oxygen, Auger spectroscopy, nitrogen implantation

[a)] Electronic mail: odyachen@uos.de, reichling@uos.de

1. Introduction

Outstanding electrochemical and defect properties of diamond make it an attractive material for a wide range of potential applications like quantum computing[32, 34, 67, 68], electrochemical[36, 69, 70] and biochemical applications[44, 71] where diamond surface properties play a paramount role. Diamond based electronic devices like high-power switching devices and radiation sensors[44, 72] as well as applications where diamond is used as a substrate[73] for subsequent deposition of diamond or another material[74-78] require a full understanding of the surface state and full control over surface chemistry and treatment procedures. Surface functionalization[79] is important for the use of diamond in biomedical applications[80-82] and applications of diamond in quantum computing require a controlled near-surface doping of the sample with nitrogen to couple a spin system to nitrogen vacancy (NV) centres in diamond,[83-85] while water layers and surface graphitization result in a severe degradation of the system functionality.[44, 86]

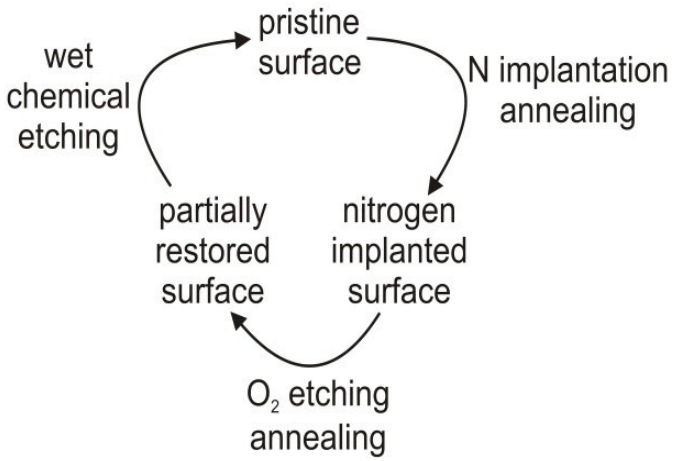

Figure 1 Cycle scheme for repetitive preparation of the diamond surface.

Therefore, the characterization of diamond with regard to surface morphology and topography,[46] optical properties,[43] mechanical properties[44] as well as electrical and thermal conductivity properties[44] has been addressed in various context. Specifically, X-ray photoelectron spectroscopy (XPS) has been applied for the characterization of nitrided,[87] oxidized,[88, 89] etched[90] and clean[62] diamond surfaces and CVD diamond films via annealing in oxygen.[91] Furthermore, it has been shown that high temperature annealing of diamond,[92] argon sputtering[90] and heavy ion bombardment[93] results in diamond surface amorphisation identified in XPS by a rise of the carbon sp^2 signal. Despite these strong efforts, a unified approach for the controlled preparation and characterization of diamond surfaces in different phase states is still missing.

Here, we focus on the precise characterization after different preparation steps to develop an optimum surface treatment procedure for diamond (100) with highest phase purity that can repetitively be prepared from the same crystal. The initial surface treatment is mechanical polishing while the repetitive steps of surface preparation sketched in Fig. 1 comprise three simple physical and chemical treatments, namely ion implantation and annealing in ultra-high vacuum (UHV), annealing in an oxygen atmosphere and wet chemical etching. XPS results show that a phase purity of 88% sp^3 can be achieved. We further demonstrate that relicts from a shallow implantation of nitrogen can completely be removed by the described procedure so that the surface exhibits also an excellent stoichiometric purity.

2. Experimental

We use CVD grown diamond samples with a size of 3 x 3 x 0.5 mm^3 and (100) surface orientation. The nitrogen concentration of the type IIa material is specified by the manufacturer (Element Six Ltd., Ascot, United Kingdom) to be below 1 ppm. Initial steps of surface preparation carried out by the manufacturer comprise mechanical polishing yielding a roughness of typically Ra < 30 nm and boiling in a strongly oxidizing acid solution composed of H_2SO_4 and KNO_3. The laboratory treatment starts with rinsing the surface with HPLC grade ethanol and dry wiping with an optical paper. After transferring the sample into the UHV chamber having a base pressure below $8 \cdot 10^{-11}$ mbar, it is flashed to a temperature of 790 °C for 3 minutes to remove volatile adsorbates like water and hydrocarbons. All subsequent preparation steps and further measurements are performed in-situ in the UHV environment except for the final step of wet chemical etching. The surface analysis after wet chemical etching is performed after re-transferring the sample into the UHV and is preceded by the same thermal treatment as used for initial surface cleaning.

To implant nitrogen and to create defects in a surface layer, the diamond sample is exposed for 60 seconds to a beam of nitrogen ions having 500 eV kinetic energy provided by a conventional sputter cleaning ion source, namely the Dual Filament Gun Model 981-2043 (Varian, Palo Alto, CA, USA) and flashed to a temperature of 790 °C to stabilize a certain concentration of nitrogen defect centres. Sample heating is accomplished by electron bombardment of a piece of Ta sheet metal attached to the diamond sample back side; the temperature is measured by a type K thermocouple attached to the Ta plate near the sample. The following step is annealing the sample in molecular oxygen (Messer Griesheim GmbH, Krefeld, Germany, O_2 purity better than 99.998 %) at a pressure of $1.33 \cdot 10^{-7}$ mbar. The sample is annealed in oxygen in many steps of 2 hours duration to track changes induced by this treatment; the total annealing time is 27 hours. The final step of preparation is wet chemical etching in a 1:1:1 acid mixture of H_2SO_4, HNO_3 and $HClO_4$ for 4 hours at a temperature of 359±2 °C and rinsing in Type I purified laboratory water (Arium 611UV, Sartorius AG, Goettingen, Germany).

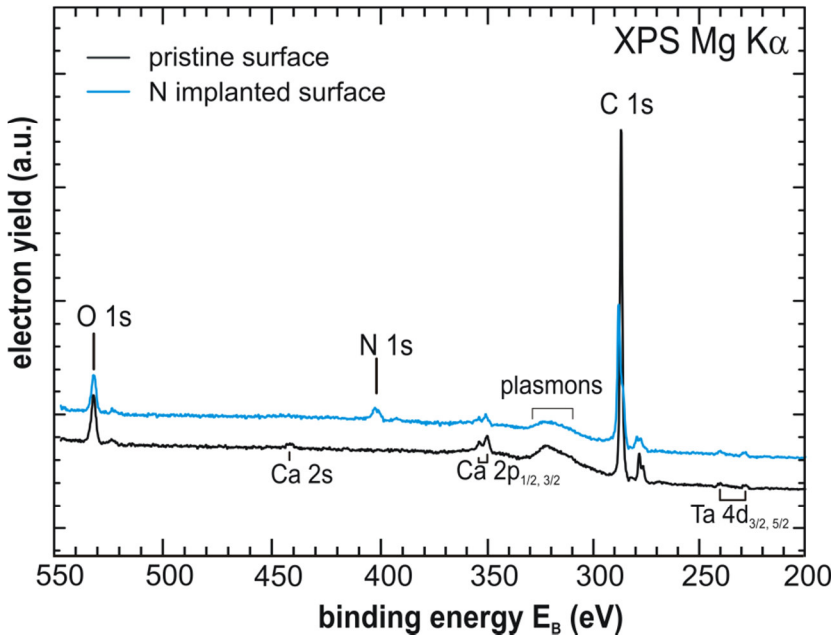

Figure 2 XPS survey spectra of the diamond surface in two states of preparation. The black curve shows a typical result for the pristine surface while the blue curve represents the result

after nitrogen implantation. The minute signal of the Ta 4d line is due to emission from the Ta sample holder assembly while the origin of a small Ca signal present in almost all spectra is not clear; we suspect a contamination from trace impurities in surface cleaning agents applied after mechanical polishing.

After each treatment and annealing step, the sample is analysed by XPS performed with a setup consisting of a X-ray source XR 50 (SPECS Surface Nano Analysis GmbH, Berlin, Germany) and a hemispherical electron energy analyser PHOIBOS 100 (SPECS Surface Nano Analysis GmbH, Berlin, Germany) equipped with a five channeltron assembly detector maintaining a high detection sensitivity at an energy resolution of 0.2 eV. Photoelectron spectra are taken using non-monochromatic radiation from the Al K-α and Mg K-α lines with photon energies of 1486.6 eV and 1253.6 eV, respectively. The X-rays are directed onto the sample under an angle of 30° while electrons emitted perpendicular from the surface are collected by the transfer optics of the electron analyser. Electrons are collected from an area having a diameter of 2 mm while the XPS sampling depth is about 3 nm (for Mg K-α radiation) yielding a sampling volume of about 10000 μm^3. The sample is heated to a temperature of 350 °C during XPS measurements to yield some electrical conductivity avoiding surface charging. A typical survey spectrum obtained after the initial cleaning step yielding the pristine surface is shown as the black line in Fig. 2. The main features are the C 1s and O 1s lines, the former having satellite and plasmon side bands. The presence of the oxygen core-level peak O 1s indicates partial oxidation of the surface and is associated to a surface chemisorbed oxygen species. It is important to note that the O1s peak at a binding energy of 532.2 eV decreases after flashing to 790 °C, however, the main part of the O 1s emission at 531.2 eV remains.

3. Results and discussion

To damage the surface and near surface layers in a controlled way and to study effects of nitrogen doping, the sample is exposed to nitrogen ions as described above. The resulting XPS survey spectrum shown as the blue curve in Fig. 2 exhibits a small but verifiable N 1s signal indicating nitrogen implantation. To further explore the impact of nitrogen bombardment, two spectral regions of the photoemission spectrum are investigated in detail with results shown in Fig. 3 and Fig. 4. The comparison of spectra shown in Fig. 3 is a confirmation of the nitrogen implantation evidenced by the presence of significant N KLL Auger lines.

The analysis of Auger lines allows for a much more sensitive detection of nitrogen than analysing the XPS spectrum and here yields clear evidence that we are able to completely remove the nitrogen implanted layer by etching the surface in an oxygen atmosphere (in the following preparation step). The surface damage is evident from a detailed analysis of the diamond and graphite plasmon regions as shown in Fig. 4. We find that a significant π- π^* transition loss peak appears after nitrogen implantation.[61] As this peak results from inelastic processes related to unoccupied π^* states at the surface, we attribute the peak to the formation of sp^2 carbon, for instance, amorphous carbon in the surface layer. The peak associated with the diamond bulk plasmon is due to a loss of energy from the departing core electrons to the bulk valence band and is shifted by 34 eV while the diamond surface plasmon is shifted by 22 eV relative to the C 1s peak.[50] The apparent drop of the intensity for the diamond bulk plasmon occurring upon nitrogen implantation yields further evidence for the transformation of diamond into sp^2 carbon.

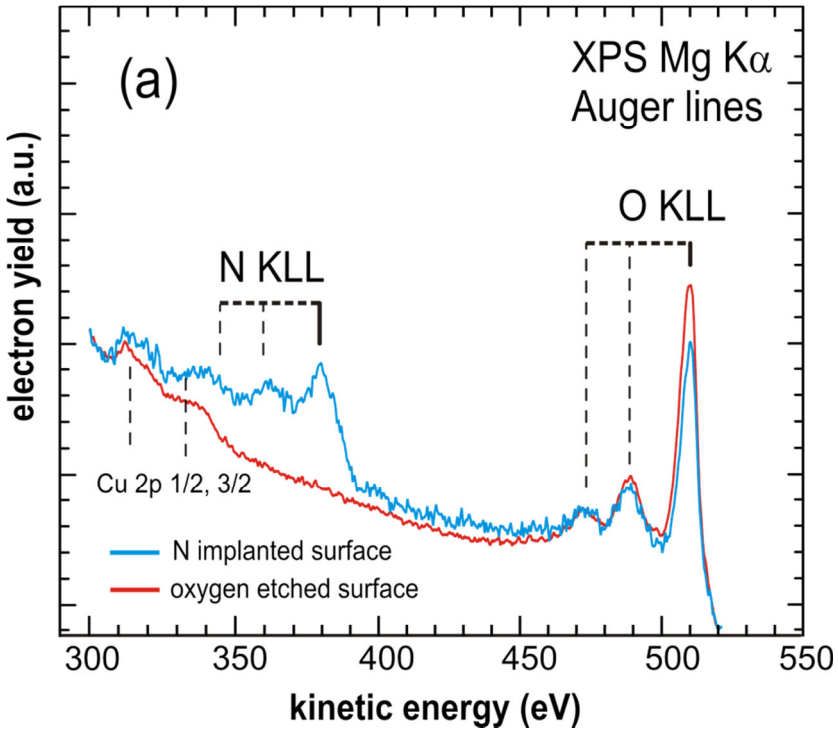

Figure 3 XPS Auger line analysis in the region of the N KLL and O KLL lines. The blue curve shows the result for the nitrogen implanted surface while the red curve demonstrates the complete removal of nitrogen after 27 hours of etching in oxygen. The small Cu signal is ascribed to stray electrons emitted from parts made of copper at the nose of the X-ray source.

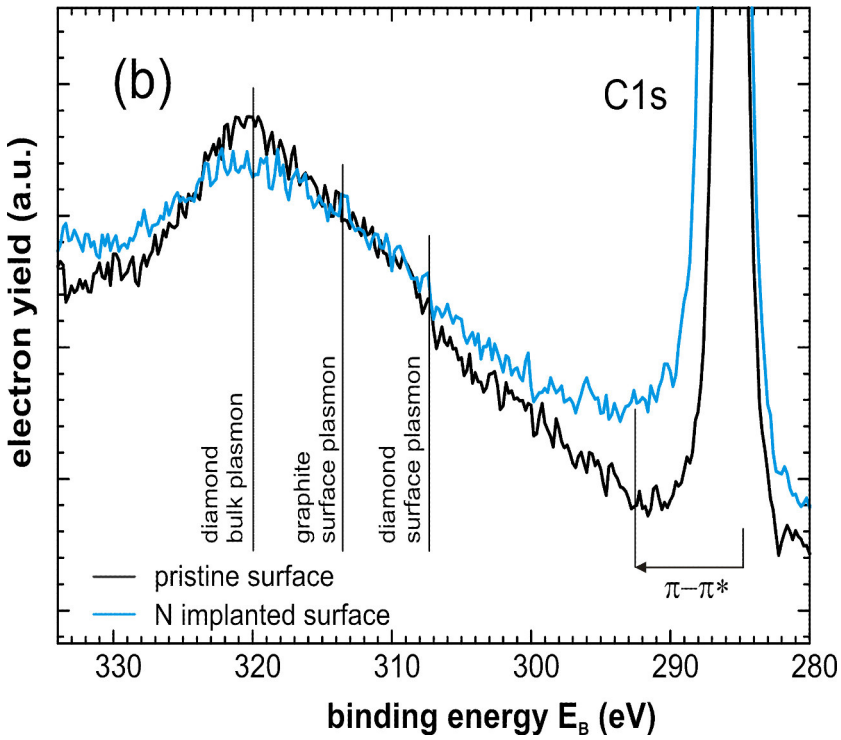

Figure 4 XPS detail spectrum in the vicinity of the C 1s peak. The black curve shows the result for the pristine surface while the blue curve represents the result after nitrogen implantation.

The major conclusions drawn from the work reported here are based on a line shape analysis of the C 1s peak allowing for an identification of different spectral components in each state of preparation as shown in Fig. 5. The analysis comprises the identification of a chemical shift due to the conversion of sp^3 to sp^2 carbon but also a shift of the sp^3 peak due to the presence of nitrogen further on denoted as sp^3(N). It is important to note that the sp^3 and sp^3(N) peaks coexist in certain steps of preparation due to inhomogeneity within the XPS sampling volume.

The basic step of the spectral deconvolution is the standard Shirley background subtraction. For fitting the C 1s line, the following single peak Gaussian/Lorentzian sum formula [61, 94, 95]

$$SPGL(E) = y_0 \left\{ \frac{m}{1+\frac{(E-E_0)^2}{\Delta E^2}} + (1-m)\exp\left[-\ln 2 \left(\frac{(E-E_0)^2}{\Delta E^2} \right) \right] \right\}$$

is used for each spectral component with centre energy E_0, width ΔE and maximum yield y_0. As the natural line width of the C 1s component is large, for our instrumentation in the current working mode, a line shape GL (30) with m = 0.7 yields the best fitting results. The starting values for the width ΔE and position E_0 are determined differently. For the peak width of the sp^3 component, a value derived from the initial untreated diamond surface is used while for fitting the sp^2 component, the width of the C line in spectra measured in our system on a clean graphite sample is used. For the sp^3(N) component, a larger peak width is used to account for a spread in local properties. The energetic position of sp^3 carbon depends on the doping of diamond where values ranging from 284 eV to 286.7 eV are reported in the literature;[62, 63] we start our fit with 285.7 eV, the position found for the pristine diamond sample. The position of the sp^3(N) peak depends on the nitrogen doping level and varies between about 284.2 eV to 288.5 eV,[64] we start with a value of 286.9 eV yielding the best fit for the preparation state with most implanted nitrogen present. The sp^2 carbon peak positions reported in literature [48, 60] vary from 284.4 eV to 284.7 eV; we adopt a starting value of 284.7 eV measured for graphite in our system. When performing the fit, we fix the distance between sp^3 and sp^2 peak positions to 1 eV to reduce the number of free parameters. The fit procedure is based on routines from the CasaXPS software and we obtained best results by a manual variation of fit parameters. The final peak positions yielded by the fit exhibit only insignificant variations from the starting values and the same values are found for the surface in all states of preparation. This indicates the robustness of the experiments against charging and the integrity of data analysis.

As a further check, we consider three additional spectral components, namely oxidation related peaks C-O (1), C-O (2) and the tail of the π- π* loss energy peak. Peaks related to either C=O or C-O-C bridge bonding[96] appear at 287.5 eV and 288.5 eV, while the feature related to the π- π* transition is shifted by about 6 eV relative to the sp^2 peak.[47, 48, 60, 97] However, none of the many trials in improving the fit by the inclusion of additional components yields a significant contribution and the clear conclusion is that the additional peaks contribute only by 1 to 2 % to the total intensity. Therefore, they are not shown in the spectra.

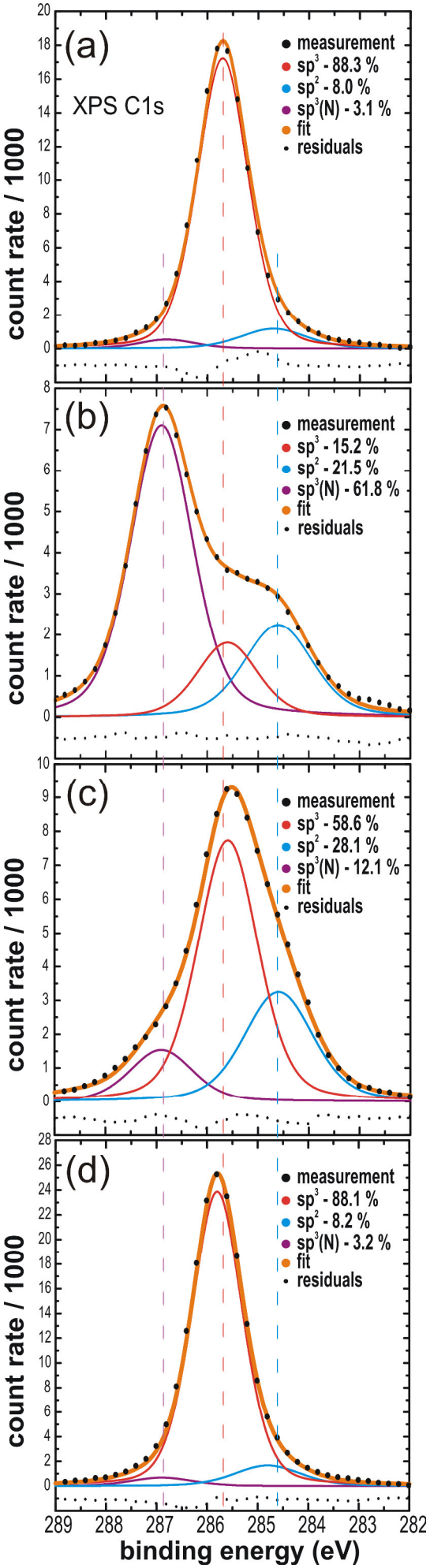

Figure 5 XPS C1s peak deconvolution for the diamond sample in different preparation states. The energies given are the peak positions for the three most important spectral contributions as obtained by the fit, including residuals revealing difference between measured and fit data points. (a) Pristine surface – sp^2 284.7 eV, sp^3 285.7 eV, sp^3(N) 286.9 eV; (b) Nitrogen implanted surface – sp^2 284.6 eV, sp^3 285.6 eV, sp^3(N) 286.9 eV; (c) Surface after etching in oxygen for 12 hours at 790 °C sp^2 284.6 eV, sp^3 285.6 eV, sp^3(N) 286.9 eV; (d) Surface after wet chemical etching and flashing to 790 °C – sp^2 284.8 eV, sp^3 285.8 eV, sp^3(N) 286.9 eV.

The deconvolution result for the C 1s peak of the pristine surface is shown in Fig. 5(a) and yields a strong contribution from sp^3 (88 %), a ten times smaller contribution of sp^2 (8 %) and a minute amount of sp^3(N) (3 %) as expected for a high quality diamond sample with a well-prepared surface. The dramatic impact of nitrogen ion implantation is seen in the C 1s line shape analysis shown in Fig. 5(b). The dominating peak is now the sp^3(N) component at 286.9 eV (62 %), however, also the sp^3 peak presumably originating from deeper layers exhibits a significant intensity (15 %). Surface damage due to the ion impact as discussed above is here evident from the strongly increased sp^2 peak (22 %).

To remove the implanted nitrogen, the sample is etched in oxygen at a partial pressure of $1.33 \cdot 10^{-7}$ mbar while the sample is kept at a temperature of 790 °C. Etching is accomplished in many steps of 2 hours with an overall annealing time of 27 hours. After 20 hours, the temperature is increased to 830 °C and for the last two hours, the temperature is set to 890 °C. Fig. 5(c) shows the C1s peak measured after 12 hours of etching in oxygen. The main feature is again the sp^3 peak (59 %) at 285.6 eV while the sp^3(N) contribution is dramatically decreased (12 %). The increased intensity of the sp^2 peak (28) % points to a further degradation of the surface by the oxygen etching procedure. Further annealing in oxygen yields the expected complete removal of nitrogen and a complete conversion of sp^3 to sp^2 bonding within the XPS sampling depth (result not shown). In several further experiments with a variation of the oxygen partial pressure and annealing temperatures, we never succeeded in maintaining a high fraction of sp^3 bonding while effectively etching the surface.

To restore the surface with a high sp^3 phase purity, we apply the final step of wet chemical etching with respective XPS results for C 1s shown in Fig. 5(d). The peak position and shape is identical within the experimental and fit errors to the result of the pristine surface shown in Fig. 5(a); we recover the surface in perfect phase purity and cleanliness.

4. Conclusions

Our results demonstrate the repetitive preparation of a diamond (100) surface with highest phase purity from the same diamond crystal. The surface stoichiometry is dominated by partial oxidation due to the final step of treatment in oxidising acids. However, this termination could be changed by further treatment in other acids or by a plasma treatment. The study further demonstrates efficient etching of the surface in an oxygen atmosphere with the sample kept at an elevated temperature. We point out, however, that etching is demonstrated here for a surface that has been heavily damaged by a bombardment with energetic ions at a high flux; the etching efficiency may be different for a less damaged surface. The results presented here and further experiments we performed show that it is not possible to maintain a high level of sp^3 phase purity for a surface treatment involving annealing in vacuum or in an oxygen atmosphere. The high sp^3 content of the pristine diamond crystal can be, however, fully restored by wet chemical etching. By re-inserting into the vacuum and cleaning by mild heating, a clean diamond surface with perfect phase purity can be prepared.

Acknowledgement

The authors gratefully acknowledge financial support from the VolkswagenStiftung through the project Az. 86392 in the framework program "Integration of molecular components in functional macroscopic systems".

References

[1] H. Hotop, E. Kolb, and J. Lorenzen, J. Electron. Spectrosc. Relat. Phenom. **16**, 213 (1979).
[2] S. Kudo, N. Kishimoto, and K. Ohno, J Phys Conf **235**, 012012 (2010).
[3] H. Morgner, Adv. Atom. Mol. Opt. Phys. **42**, 387 (2000).
[4] O. Höfft *et al.*, J. Phys. Chem. B **110**, 17115 (2006).
[5] O. Höfft *et al.*, Langmuir **22**, 7120 (2006).
[6] Y. Harada, S. Masuda, and H. Ozaki, Chem. Rev. **97**, 1897 (1997).
[7] A. Borodin, and M. Reichling, Phys. Chem. Chem. Phys. **13**, 15442 (2011).
[8] S. Krischok *et al.*, Surf. Interface Anal. **37**, 83 (2005).
[9] W. Maus-Friedrichs *et al.*, Surf. Sci. **237**, 257 (1990).
[10] K. Ohno *et al.*, J. Chem. Phys. **94**, 2675 (1991).
[11] M. J. Verheijen *et al.*, J. Phys. E Sci. Instrum. **17**, 904 (1984).
[12] K. Mitsuke, T. Takami, and K. Ohno, J. Chem. Phys. **91**, 1618 (1989).
[13] W. Maus-Friedrichs *et al.*, Surf. Sci. **515**, 499 (2002).
[14] W. Maus-Friedrichs, S. Dieckhoff, and V. Kempter, Surf. Sci. **249**, 149 (1991).
[15] W. Maus-Friedrichs *et al.*, Surf. Sci. **253**, 137 (1991).
[16] A. Borodin *et al.*, J. Chem. Phys. **120**, 5407 (2004).
[17] A. Borodin *et al.*, Vacuum **73**, 15 (2004).
[18] A. Borodin *et al.*, Nucl. Instrum. Meth. B **203**, 205 (2003).
[19] H. Ferkel, R. Feltgen, and D. Pikorz, Rev. Sci. Instrum. **62**, 2626 (1991).
[20] W. S. Taylor, J. G. Dulak, and S. N. Ketkar, J. Am. Soc. Mass. Spectrom. **1**, 448 (1990).
[21] O. Dyachenko *et al.*, Chem. Phys. Lett. **640**, 72 (2015).
[22] G. H. Enevoldsen *et al.*, Phys. Rev. B **78**, 045416 (2008).
[23] H. H. Pieper *et al.*, Phys. Chem. Chem. Phys. **12**, 12436 (2010).
[24] S. Krischok, O. Hofft, and V. Kempter, Nucl. Instrum. Meth. B **193**, 466 (2002).
[25] S. Munnix, and M. Schmeits, Phys. Rev. B **30**, 2202 (1984).
[26] S. Wendt *et al.*, Science **320**, 1755 (2008).
[27] C. M. Yim, C. L. Pang, and G. Thornton, Phys. Rev. Lett. **104**, 036806 (2010).
[28] M. Brause, S. Skordas, and V. Kempter, Surf. Sci. **445**, 224 (2000).
[29] C. Di Valentin, G. Pacchioni, and A. Selloni, Phys. Rev. Lett. **97**, 1666803 (2006).
[30] C. Di Valentin, G. Pacchioni, and A. Selloni, J. Phys. Chem. C **113**, 20543 (2009).
[31] S. Hongo *et al.*, Surf. Sci. **287**, 588 (1993).
[32] T. D. Ladd *et al.*, Nature **464**, 45 (2010).
[33] J. Wrachtrup, and F. Jelezko, J. Phys.: Condens. Matter **18**, S807 (2006).
[34] R. J. Epstein *et al.*, Nature Physics **1**, 94 (2005).
[35] H. Zanin *et al.*, ACS Appl. Mater. Interfaces **6**, 990 (2014).
[36] J. V. Macpherson, Phys. Chem. Chem. Phys. **17**, 2935 (2015).
[37] Z. Xing *et al.*, Tissue Eng. **19**, 1783 (2013).
[38] I. Rehor *et al.*, Small **10**, 1106 (2014).
[39] E. K. Chow *et al.*, Sci. Trans. Med. **3**, 73ra21 (2011).
[40] H. Umezawa, T. Matsumoto, and S. I. Shikata, IEEE Electron Device Lett. **35**, 1112 (2014).
[41] T. Iwasaki *et al.*, Appl. Phys. Express **5**, 091301 (2012).
[42] P. Rath *et al.*, Appl. Phys. Lett. **105**, 251102 (2014).
[43] A. Gruber *et al.*, Science **276**, 2012 (1997).
[44] R. S. Sussmann, *CVD Diamond for Electronic Devices and Sensors* (John Wiley & Sons, Ltd, 2009).

[45] J. A. Garrido, T. Heimbeck, and M. Stutzmann, Phys. Rev. B **71**, 245310 (2005).
[46] M. Nimmrich *et al.*, Phys. Rev. B **81**, 201403R (2010).
[47] V. S. Smentkowski *et al.*, Surf. Sci. **330**, 207 (1995).
[48] F. R. McFeely *et al.*, Phys. Rev. B **9**, 5268 (1974).
[49] J. F. Morar *et al.*, Phys. Rev. B **33**, 1340 (1986).
[50] J. I. B. Wilson, J. S. Walton, and G. Beamson, J. Electron. Spectrosc. Relat. Phenom. **121**, 183 (2001).
[51] F. Maier *et al.*, Surf. Sci. **443**, 177 (1999).
[52] R. Graupner *et al.*, Phys. Rev. B **57**, 12397 (1998).
[53] T. Haensel *et al.*, Phys. Status Solidi A **206**, 2022 (2009).
[54] L. Diederich *et al.*, Surf. Sci. **418**, 219 (1998).
[55] P. K. Baumann, and R. J. Nemanich, Surf. Sci. **409**, 320 (1998).
[56] S. Dieckhoff *et al.*, Surf. Sci. **423**, 53 (1999).
[57] S. Kono *et al.*, New Diamond Front. Carb. Techn. **17**, 231 (2007).
[58] K. Kobashi, Cornell University, Preprint Archive, Materials Science, arXiv:1406.6204 (2014).
[59] A. T. Collins, J. Phys.: Condens. Matter **14**, 3743 (2002).
[60] P. A. Brühwiler *et al.*, Phys. Rev. Lett. **74**, 614 (1995).
[61] D. N. Belton, and S. J. Schmieg, J. Vac. Sci. Technol. A **8**, 2353 (1990).
[62] L. Diederich *et al.*, Surf. Sci. **417**, 41 (1998).
[63] S. Ferro, M. Dal Colle, and A. De Battisti, Carbon **43**, 1191 (2005).
[64] J. Chastain, and J. F. Moulder, *Handbook of X-Ray Photoelectron Spectroscopy: A Reference Book of Standard Spectra for Identification and Interpretation of XPS Data* (Physical Electronics Division, Perkin-Elmer Corporation, 1992).
[65] I. Kusunoki *et al.*, Diam. Relat. Mater. **10**, 1676 (2001).
[66] F. Maier, J. Ristein, and L. Ley, Phys. Rev. B **64**, 165411 (2001).
[67] J. Wrachtrup, PNAS **107**, 9479 (2010).
[68] R. Chapman, and T. Plakhotnik, Chemical Physics Letters **507**, 190 (2011).
[69] K. B. Holt, Phys. Chem. Chem. Phys. **12**, 2048 (2010).
[70] S. Orlanducci *et al.*, Chemical Physics Letters **549**, 51 (2012).
[71] J. A. Garrido *et al.*, Appl. Phys. Lett. **86**, 073504 (2005).
[72] W. Dexters *et al.*, Phys. Chem. Chem. Phys. **17**, 9619 (2015).
[73] Q. Yu *et al.*, Chemical Physics Letters **539**, 74 (2012).
[74] S. A. O. Russell *et al.*, IEEE Electron Device Lett. **33**, 1471 (2012).
[75] D. A. J. Moran *et al.*, IEEE Electron Device Lett. **32**, 599 (2011).
[76] M. Y. Liao *et al.*, Phys. Rev. B **81**, 033304 (2010).
[77] T. Teraji *et al.*, J. Appl. Phys. **105**, 126109 (2009).
[78] K. Haenen *et al.*, J. Phys.: Condens. Matter **21**, 364204 (2009).
[79] H. A. Girard *et al.*, Phys. Chem. Chem. Phys. **13**, 11517 (2011).
[80] V. N. Mochalin *et al.*, Nature Nanotech. **7**, 11 (2012).
[81] A. Alhaddad *et al.*, Small **7**, 3087 (2011).
[82] K. V. Purtov *et al.*, Nanoscale Res. Lett. **5**, 631 (2010).
[83] S. Schaefer *et al.*, Solid State Sci **10**, 1314 (2008).
[84] W. Harneit *et al.*, Phys. Status Solidi B **233**, 453 (2002).
[85] W. Harneit, Phys. Rev. A **65**, 032322 (2002).
[86] R. Kalish, in *Quantum Information Processing with Diamond: Principles and Applications* (Woodhead Publishing, 2014).
[87] I. Kusunoki *et al.*, Surf. Sci. **492**, 315 (2001).
[88] W. Deferme *et al.*, Diam. Relat. Mater. **15**, 687 (2006).
[89] K. Bobrov *et al.*, Appl. Surf. Sci. **196**, 173 (2002).

[90] Y. Kawabata, J. Taniguchi, and I. Miyamoto, Diam. Relat. Mater. **13**, 93 (2004).
[91] P. John *et al.*, Diam. Relat. Mater. **11**, 861 (2002).
[92] H. Estrade-Szwarckopf, Carbon **42**, 1713 (2004).
[93] S. Pezzagna *et al.*, New J. Phys. **13**, 035024 (2011).
[94] S. Kaciulis, Surf. Interface Anal. **44**, 1155 (2012).
[95] S. Evans, Surf. Interface Anal. **17**, 85 (1991).
[96] S. Skokov, B. Weiner, and M. Frenklach, Phys. Rev. B **49**, 11374 (1994).
[97] R. Graupner *et al.*, Diam. Relat. Mater. **3**, 891 (1994).

4.4. Influence of wet and dry etching, Ar sputtering and shallow nitrogen implantation on diamond surfaces

Several additional different studies aiming at restoring of the diamond surface have been performed. These treatment experiments comprise ion implantation, argon sputtering, annealing, annealing in an oxygen atmosphere in ultra-high vacuum (UHV) and wet chemical etching. In this study the oxidizing acid treatment and surface processing via annealing in oxygen under UHV conditions has been compared. It is demonstrated that an optimal surface treatment procedure for diamond (100) requires annealing in an oxygen atmosphere in order to fully remove the damage induced by the nitrogen implantation.

In this experimental series implantation performed by means of PCS ECR plasma source (SPECS Surface Nano Analysis GmbH, Berlin, Germany). Plasma implantation allows more accurate dose, energy and thus precise dopant in depth location control.

It has been demonstrated how nitrogen implantation could be detected by surface spectroscopy analysis. It was shown that Ar sputtering (Chapter 4.2. Fig. 5a,b and Fig. 39) as well as annealing oxygen at the temperature above 830 °C (see Fig. 40) lead to surface graphitization. Here is demonstrated how diamond surface phase state could be restored after Ar sputtering or nitrogen implantation by means of the same dry etching annealing in oxygen in UHV described in the Chapter 4.3. Furthermore it has been shown that nitrogen implantation could be fully removed by our treatment procedure, what is confirmed by direct monitoring of the Auger NKLL and C1s carbon peak energy position.

4.4.1. Recovery of the perfect phase purity diamond (100) surface after Ar sputtering induced damage

Results have been obtained on a CVD grown diamond sample (Sample # 41) with a size of 3 x 3 x 0.5 mm^3 and (100) surface orientation. The nitrogen concentration of the type IIa material is specified by the manufacturer (Element Six Ltd., Ascot, United Kingdom) to be below 1 ppm. Initial steps of surface preparation carried out by the manufacturer comprise mechanical polishing yielding a roughness of typically Ra < 30 nm and boiling in a strongly oxidizing acid solution composed of H_2SO_4 and KNO_3. The laboratory treatment starts with rinsing the surface with HPLC grade ethanol and dry wiping with an optical paper. After transferring the sample into the UHV chamber having a base pressure below $8 \cdot 10^{-11}$ mbar samples are flashed to a temperature of 790 °C for 3 m to remove volatile adsorbates like water and hydrocarbons. All subsequent preparation steps and further measurements are performed in-situ in the UHV environment except for the wet chemical etching. The surface analysis after wet chemical etching is performed when the sample was re-transferred into the UHV and is processed by the same thermal treatment used for initial surface cleaning.

The sample is examined by XPS using same instrumentation, namely an X-ray source XR 50 (SPECS Surface Nano Analysis GmbH, Berlin, Germany) and a HSA PHOIBOS 100 (SPECS Surface Nano Analysis GmbH, Berlin, Germany) with a five MCDs yielding resolution of 0.2 eV. Photoelectron spectra are taken using non-monochromatic radiation from the Mg K-α lines with photon 1253.6 eV. Heating of 450° C is applied during the measurements.

First "as received" sample after short flashing at 790 °C for 3 m has been measured by means of XPS. The initial C1s peak position of the sample # 41 differs from our standard 1 ppm samples, exhibiting the C1s peak position E_B = 285.5 eV, and is shifted towards higher binding energy to E_B = 285.8 eV (Fig. 39). The higher initial nitrogen content or very strong surface oxidation cause this abnormality shift is supposed. Following the same deconvolution approach of the C1s peak, described in details in the Chapter 4.3, main components have been defined, revealing 89.5 % for sp^3, 6.7 % for sp^2 and 3.7 % for sp^3 (N) correspondingly. There are also three additional minor deconvolution components, namely oxidation related peaks C-O (1), C-O (2) and the tail of the π- π^* loss energy peak. Peaks related to either C=O or C-O-C bridge bonding appear at 287.5 eV and 288.5 eV, while the feature related to the π - π^* transition is shifted by about 6 eV relative to the sp^2 peak. However, none of these components contribute significantly in improving the fit and these additional peaks reveal only 1 to 2 % to the total intensity. Therefore, they are not shown in the spectra.

Next sample exposed to Ar sputtering energy of 1 keV defocused beam produced by Dual Filament Gun Model 981-2043 (Varian, Palo Alto, CA, USA). The Ar sputtering performed in a two steps each of a 1 m time. A Fig. 39 demonstrates XPS spectra of a carbon C1s after flashing (red line) and after 2 m of Ar sputtering by 1 keV energy defocused beam (dark yellow line). It should be noticed that after sputtering procedure C1s peak shift occur only due to significant broadening caused by the argon induced damage and thus surface amorphization. This amorphization effect is conducted by appearance of the distinct sp^2 component at the E_B = 284.5 eV.

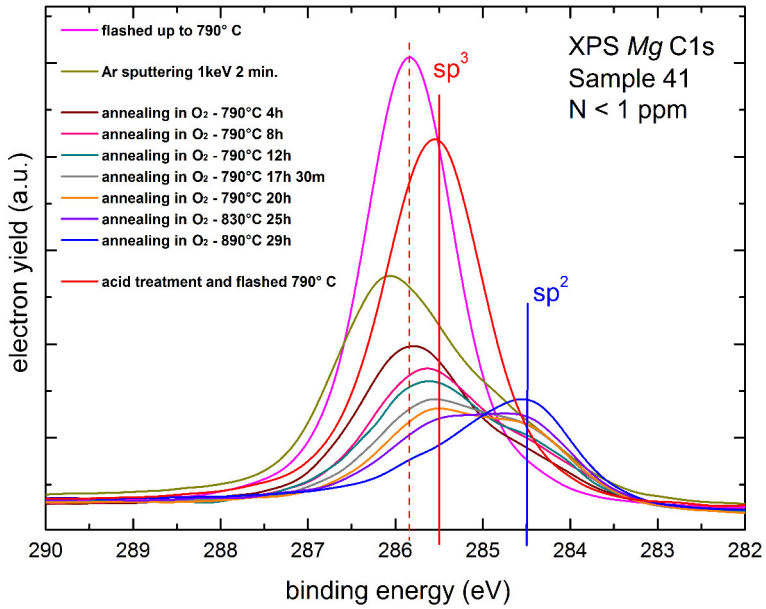

Fig. 39 XPS spectra of a carbon C1s shift after Ar sputtering, dry etching and acid treatment.

The following treatment step is a same dry etching procedure performed by annealing the sample in molecular oxygen (Messer Griesheim GmbH, Krefeld, Germany, O_2 purity better than 99.998 %) at a pressure of $1.33 \cdot 10^{-7}$ mbar described in the Chapter 4.3. The sample is annealed in oxygen in steps of 2 hours duration to track changes induced by this treatment; the total annealing time is 29 hours. The dry etching generally divided into three temperature modes, first sample annealed at 790° C for 20 h, in the second step temperature set to 830° C with 5 h annealing time, in the last third step temperature increased to 890° C with a 4 h annealing time (Fig. 39). All steps of the dry etching treatment tracked by XPS and are presented in the Fig. 40. Increasing of the annealing temperature above 800° C leads to the complete surface amorphization and final spectra reveals asymmetrical C1s peak shifted to the E_B = 284.5 eV and predominant sp^2 component (blue line).

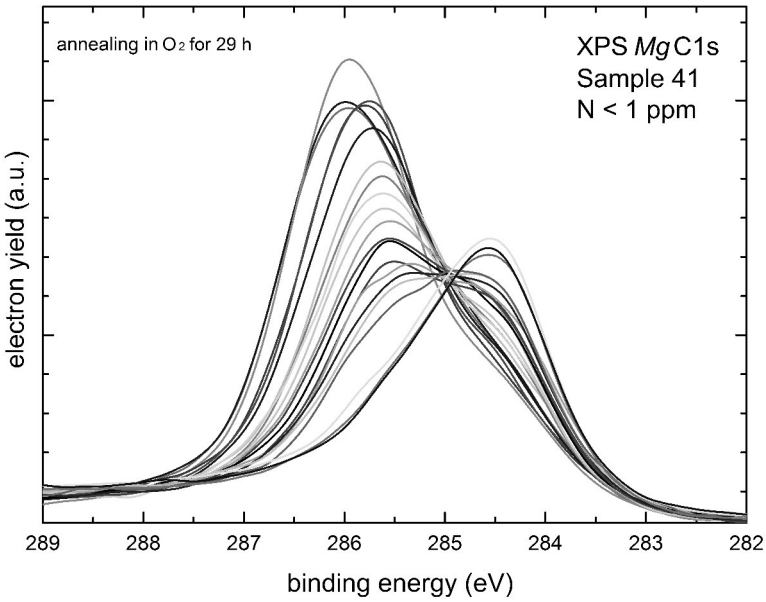

Fig. 40 All steps of the dry etching treatment via annealing in O_2 for 29 h.

The final step of preparation is wet chemical etching in a 1:1:1 acid mixture of H_2SO_4, HNO_3 and $HClO_4$ for 4 hours at a temperature of 359 ± 2 °C and rinsing in Type I purified laboratory water (Arium 611UV, Sartorius AG, Goettingen, Germany). After retransferring sample back into the UHV spectroscopy chamber sample flashed 790 °C for 3 m and XPS spectra revealing C1s peak recorded (a red line on the Fig. 39). XPS reveals carbon peak with a symmetrical shape situated at the EB = 285.5 eV corresponding to the sp3 diamond state. The deconvolution yields 88.2 % for sp^3, 6.6 % for sp^2 and 4.4 % for sp^3 (N) correspondingly.

Conclusion

It has been demonstrated that Ar sputtering leads to the surface amorphization, observed shift of the C1s peak related to the peak broadening and not the chemical shift due to the surface nitrogen doping.

Same dry etching procedure, described in the Chapter 4.3.1., could be applied in order to restore completely surface phase state after damage induced by Ar sputtering. Surface phase state has been improved after treatment cycle and reveals C1s of E_B = 285.5 eV.

4.4.2. Influence of a wet and dry etching, Ar sputtering and shallow nitrogen implantation via plasma source on a diamond surface

The CVD grown diamond sample (Sample # 32) with a size of 3 x 3 x 0.5 mm^3 and (100) surface orientation has been used. The nitrogen concentration of the type IIa material is specified by the manufacturer (Element Six Ltd., Ascot, United Kingdom) to be below 1 ppm. Initial steps of surface preparation carried out by the manufacturer comprise mechanical polishing yielding a roughness of typically Ra < 30 nm and boiling in a strongly oxidizing acid solution composed of H_2SO_4 and KNO_3. After transferring the sample into the UHV chamber having a base pressure below $8 \cdot 10^{-11}$ mbar samples are flashed to a temperature of 790 °C for 3 m to remove volatile adsorbates like water and hydrocarbons. All subsequent preparation steps and further measurements are performed in-situ in the UHV environment except for the implantation procedure and the step of wet chemical etching. The surface analysis after implantation and wet chemical etching is performed when the sample was re-transferred into the UHV and is processed by the same thermal treatment used for initial surface cleaning.

The sample is examined by XPS using same instrumentation, namely an X-ray source XR 50 (SPECS Surface Nano Analysis GmbH, Berlin, Germany) and a HSA PHOIBOS 100 (SPECS Surface Nano Analysis GmbH, Berlin, Germany) with a five MCDs yielding resolution of 0.2 eV. Photoelectron spectra are taken using non-monochromatic radiation from the Mg K-α lines with photon 1253.6 eV. Heating of 450° C is applied during the measurements.

First sample was boiled in a wet chemical 1:1:1 acid mixture of H_2SO_4, HNO_3 and $HClO_4$ for 4 hours according to our standard procedure (please see Chapter 3.8). Than has been measured by means of XPS, whereas spectra revealing C1s carbon peak at E_B = 285.6 eV is presented in the Fig. 41 black line. Also XPS region of the Auger NKLL line is tracked (Fig. 42).

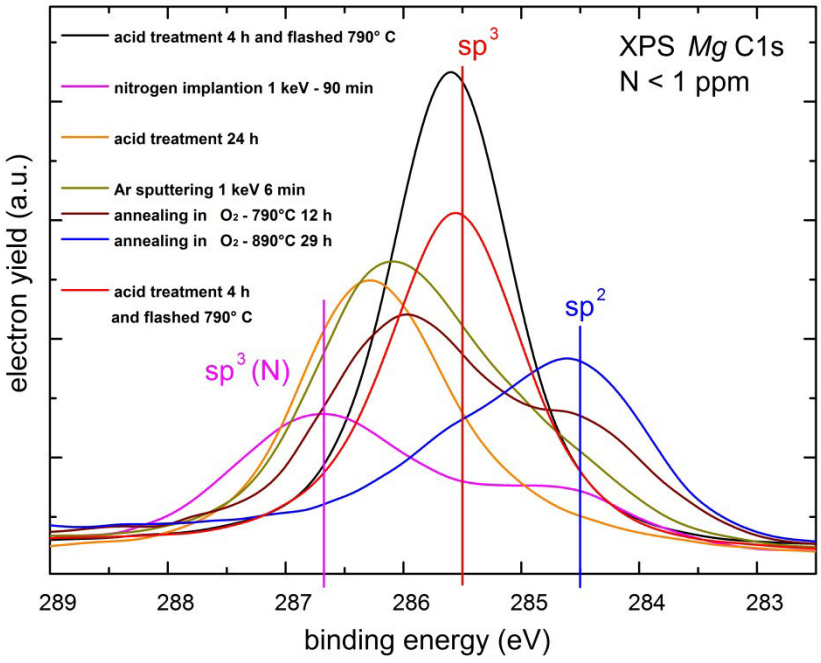

Fig. 41 Sample 32 Carbon C1s peak shift.

To implant nitrogen and to create defects in a surface layer, the diamond sample is exposed to ion beam flux of 1 keV energy for 90 min produced by the PCS ECR plasma source (SPECS Surface Nano Analysis GmbH, Berlin, Germany). After re-transferring sample into the spectroscopy chamber and flashing 790 °C for 3 m. XPS spectra disclose noticeable NKLL Auger signal. At the same time no evident growth of the N1s peak could be resolved. Also strong carbon C1s peak shift towards E_B = 286.7 eV detected, due to surface doping.

In this experiment I try to remove implanted nitrogen and to recover surface initial phase state by means of wet chemical etching. Sample was boiled three times in a wet chemical 1:1:1 acid mixture of H_2SO_4, HNO_3 and $HClO_4$ for 8 hours according to our standard procedure (Chapter 3.8.). However, after 24 h of acid treatment, the C1s peak is still shifted towards higher binding energy and positioned at E_B = 286.3 eV. At the same time NKLL Auger peak signal disappear completely after 8 h of acid treatment.

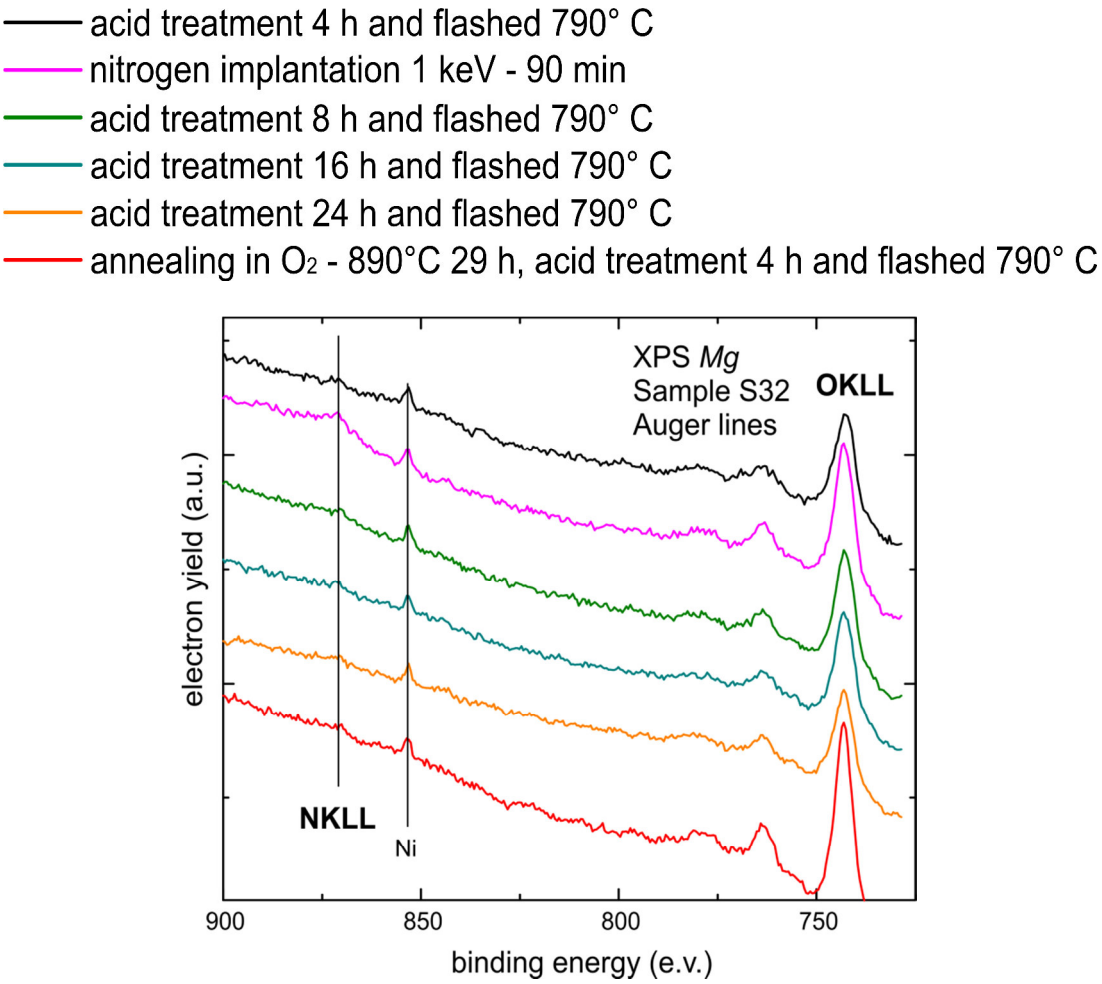

Fig. 42 Sample # 32 XPS spectra Auger lines region.

In order to remove nitrogen doped layers and to restore initial surface phase state completely sample is exposed to defocused Ar beam of 1 keV energy sputtering and the same dry etching treatment, described earlier (Chapter 4.3 and 4.4.1), via annealing in molecular oxygen in UHV. In the Fig. 41 wine line presents XPS of the diamond surface after 12 h of annealing in oxygen. The dry etching was again performed in the three temperature modes, first sample annealed at 790°C for 20 h, in the second step annealing 5 h at 830°C, in the third step 4 h at 890°C. Increasing of the annealing temperature above to 800°C leads to the

complete surface graphitization and revealing C1s peak shift to the E_B = 284.5 eV and predominant sp^2 component.

Additionally diamond plasmon region has been analyzed. In the Fig. 43 could be seen, that diamond bulk and surface plasmons structure shape similar for initial surface and final restored surface, with little bit more prominent signal for initial state of diamond bulk plasmon. Figure 43 (blue line) shows noticeable rise of the π-π* feature after last step of annealing in oxygen 4 h at 890° C, also minor π-π* feature increase after nitrogen implantation and Ar sputtering can be observed.

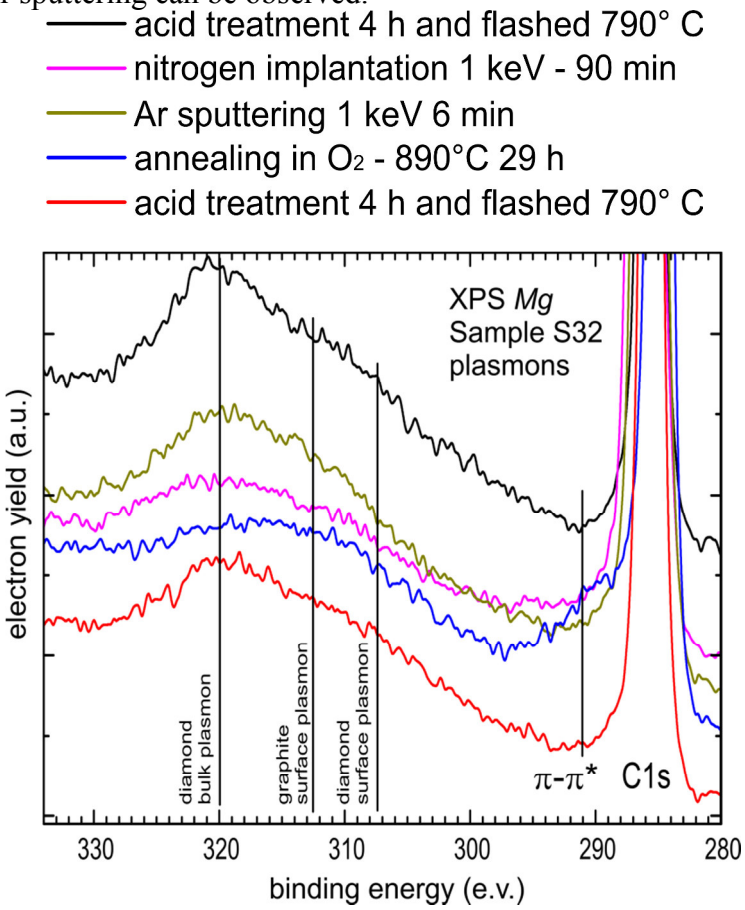

Fig. 43 Sample # 32 XPS spectra plasmon region.

The final step of preparation again was standard (Chapter 3.8) wet chemical etching. After retransferring sample back into the UHV spectroscopy chamber sample flashed 790 °C for 3 m and XPS spectra revealing C1s peak recorded (Fig. 41 red line). XPS reveals a symmetrical shape and complete restoring of the initial sp^3 peak position at EB = 285.6 eV. Thus successful surface recovery after dry etching and following wet etching processing is concluded.

Conclusion

In this experiment wet and dry treatments efficiency has been compared. It has been demonstrated despite NKLL Auger line vanishes after long acid treatment, the C1s peak as an indirect marker still not fully restored. Thus only additional dry etching processing can fully remove the nitrogen implantation damage and restore the E_B = 285.6 eV carbon peak position. Same dry etching procedure, please see Chapter 4.3.1, is also applicable for completely surface phase state restoring after 1 keV plasma nitrogen implantation.

4.5. NV centers production in nitrogen implanted diamond

The goal in terms of the "Quantum computing" project to establish a well controllable, clear and effective nitrogen vacancies creation procedure. This section comprises experimental results of nitrogen implantation via plasma source and following creation of NV centres by annealing in UHV.

First this task involves detection of implanted nitrogen that could be implemented by means of XPS. It has been demonstrate here that nitrogen doping could be defined by direct photoelectron N1s peak and Auger NKLL peak measurements, at low nitrogen concentration. However, as an indirect marker the C1s peak shift measurements could be used. It has been demonstrated in the previous session that "as grown" nitrogen doped diamonds reveal significant shift of the carbon C1s core shell peak (Chapter 4.2) and that nitrogen implantation leads to even stronger C1s peak shift depending on the implantation dose (Chapter 4.3 and 4.4.3).

Secondary, successfulness of the NV^- formation after nitrogen plasma implantation is confirmed by optical fluorescence spectroscopy and ODMR measurements.

4.5.1. Features of nitrogen detection by XPS

To be able to confirm a nitrogen implantation from the plasma source XPS has been used to detect amount of implanted nitrogen in the diamond samples. It is quite challenging to detect low nitrogen concentrations $\leq$ 1.5 At%, because of the small photoelectron cross sections, photoelectron peak could not be resolved. However, I found that nitrogen Auger line is more sensitive and could be detected even at low nitrogen concentrations.

The CVD grown diamond Sample # 10 a size of 3 x 3 x 0.5 mm^3 and (100) surface orientation has been used. The nitrogen concentration of the type IIa material is specified by the manufacturer (Element Six Ltd., Ascot, United Kingdom) to be below 1 ppm. Initial steps of surface preparation carried out by the manufacturer comprise mechanical polishing yielding a roughness of typically Ra < 30 nm and boiling in a strongly oxidizing acid solution mixture of H_2SO_4 and KNO_3. The laboratory treatment encloses rinsing the surface with HPLC grade ethanol and dry wiping with an optical paper.

After transferring sample into the implantation chamber it was annealed at 400° C for 1 h to remove volatile adsorbates like water and hydrocarbons. Next it was implanted at energy of 1 keV for 40 min by the PCS ECR plasma source (SPECS Surface Nano Analysis GmbH, Berlin, Germany), and annealed at 820° C for 2 h to form NV centers.

After transferring the sample into the UHV spectroscopy chamber (a base pressure below $8 \cdot 10^{11}$ mbar), it was flashed to a temperature of 790 °C for 3 minutes for adsorbates cleaning purposes. The sample is examined by XPS using same instrumentation, namely an X-ray source XR 50 (SPECS Surface Nano Analysis GmbH, Berlin, Germany) and a HSA PHOIBOS 100 (SPECS Surface Nano Analysis GmbH, Berlin, Germany) with a five MCDs yielding resolution of 0.2 eV. Photoelectron spectra are taken using non-monochromatic radiation from the Mg K-α lines with photon 1253.6 eV. Heating of 350° C is applied during the measurements.

XPS measurements of the carbon C1s photoelectron peak after nitrogen implantation and subsequent 790 °C flashing for 3 m shown on Fig. 44. The C1s peak exhibit shift towards higher binding energy due to the nitrogen doping. Also an amorphization is induced by the

nitrogen ion flux leading to the growth of the sp^2 component. A same deconvolution procedure, described in the Chapter 4.3., applied to extract main components, yielding 9.2 % for sp^3, 24.0 % for sp^2 and 63.6 % for sp^3(N) correspondingly (Fig. 44).

Fig. 45 shows XPS spectra region corresponded to the NKLL Auger line. The minute signal of the Cu is due to the copper presence in the XPS assembly part, while the origin of a Ca signal is not clear; a contamination from trace impurities in surface cleaning agents applied after mechanical polishing is suspect. It is important to mention that photoelectron peak N1s is not resolved after implantation.

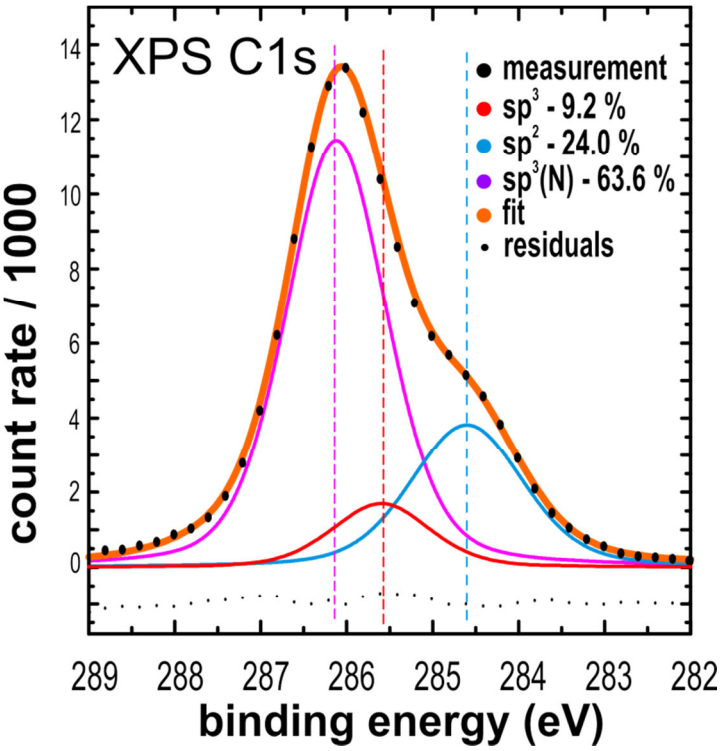

Fig. 44 Deconvolution of the C1s peak after implantation and flashing 790 °C for 3 m.

Taking into account sensitivity of the Mg anode to nitrogen 2.85 and oxygen 4.26 the value of the nitrogen concentration relative oxygen could be extracted from the spectra. These are for oxygen a 4.4 At % and for nitrogen is estimated to be a 1.5 At %. A comparison of N KLL peak and O KLL peak intensities ten times increased presented on the Fig. 44.

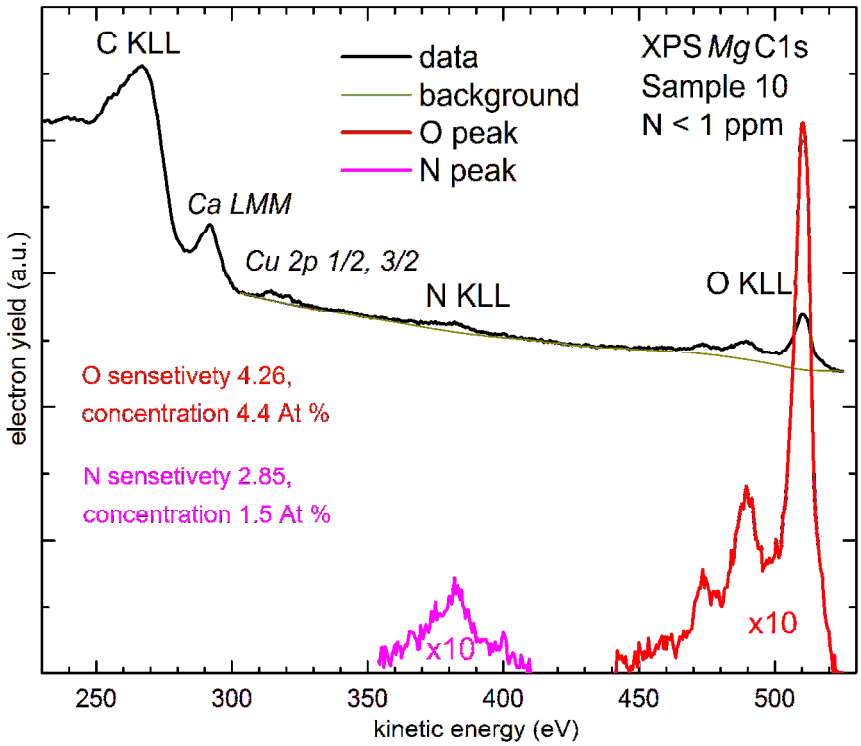

Fig. 45 XPS spectra region with the corresponding NKLL and OKLL Auger lines.

Thus in order to monitor nitrogen doping by XPS it is important to track precisely NKLL Auger line intensity after nitrogen implantation and after dry etching treatment via annealing in oxygen in UHV chamber. However by a higher doping dose, it is better to monitor both photoelectron peak N1s and NKLL line during the measurements.

Conclusion

It has been shown how nitrogen doping level could be measured and tracked by means of X-ray photoelectron spectroscopy. Implementation of the X-ray induced Auger lines analysis reveals low concentration of nitrogen namely 1.5 At %, whereas photoelectron peak N1s could not be resolved.

4.5.2. Shallow NV centers production

For production of the NV centres ultrapure diamond required, in order to have the possible lowest nitrogen concentration and no or minimum NVs content in the "as grown" sample.[1] Particularly for a low energy shallow implantation the quality of a sample surface is crucial.[2]

The CVD grown diamond electronic grade (EL) sample # MZ15 a size of 3 x 3 x 0.5 mm^3 and (100) surface orientation has been. The nitrogen concentration of the type IIa material is specified by the manufacturer (Element Six Ltd., Ascot, United Kingdom) to be below 5 ppb and boron concentration below 1 ppb. Initial steps of surface preparation carried out by the manufacturer comprise mechanical polishing yielding a roughness of typically Ra < 5 nm. Previous to the implantation sample has been boiled in a strongly oxidizing acid solution mixture of H_2SO_4, HNO_3 and $HClO_4$ a 1:1:1 acid mixture of for 4 h at a temperature of 359±2 °C and rinsed in Type I purified laboratory water (Arium 611UV, Sartorius AG).

Sample MZ15 was fixed with a hard tantalum mask on the tantalum table, equipped with tungsten heating wire under the table (right in Fig. 17). Temperature controlled by two thermocouples, one attached with a molybdenum screw on top of the tantalum mask fixing sample on the table, another attached to massive sample holding construction (left in Fig. 17).

After transferring into the implantation chamber sample annealed up to 500° C in cleaning purposes for 1 hour in the implantation chamber (base pressure of $1x10^{-9}$ mbar). Nitrogen implantation has been performed by SPECS PCS-ESR microwave plasma source (Chapter 3.6.) with two-grid set configuration in the hybrid-atom source mode.

According to SRIM modelling implanted nitrogen atoms mean depth at 1 keV energy will be in the range from 2 - 3 nm (SRIM2011 Fig. 46). Left in the Fig. 46 present the ion trajectories simulation result and left ion penetration range corresponded to the 500 eV implantation energy. The ion beam consists mainly of molecular $^{14}N^{2+}$ ions also beam contains a few percent of other kinds of ions, which are mainly atomic $^{14}N^{+}$. It should be noticed that 1 keV acceleration is energy applied, however when molecular $^{14}N^{2+}$ ion hit the surface it is spited in a two atomic $^{14}N^{+}$.

First when plasma ignited and acceleration potential applied I wait for a 20 min before implantation in order to stabilize ion beam. At this time sample is closed by mechanical shutter to avoid implantation. Than sample # MZ15 was implanted by nitrogen purity 99.99% (Air Liquid, Düsseldorf, Germany) at 1 keV with the dose 4.78 x 10^{13} ions / cm^2 for 90 min. Implantation followed by electron bombardment thermal annealing in vacuum (10^{-8} mbar) at 820° C for 2 hours to form NV centres. In order to avoid uncontrollable vacancies creation sample has not been measured by XPS.

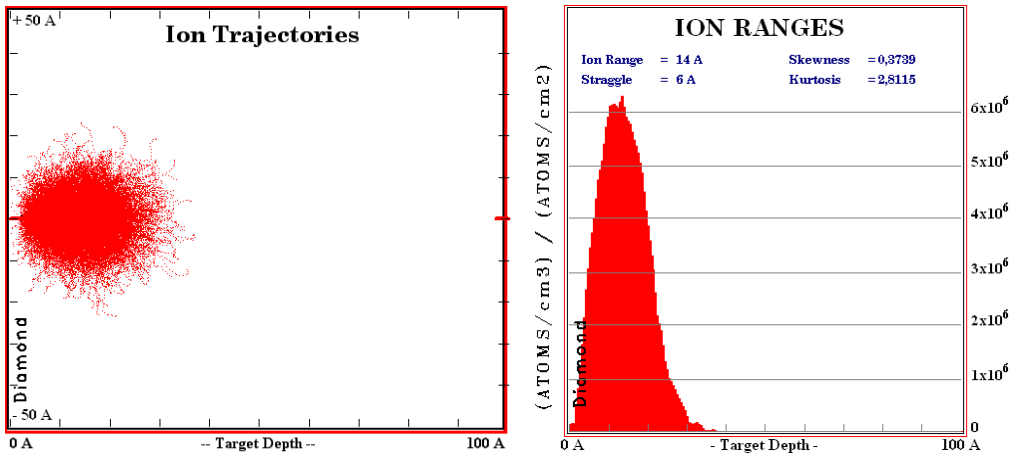

Fig. 46 Results of SRIM modeling for N_2 implantation energy of 1 keV.

4.5.3. Optical measurements, detection of NV^- centers

In order to confirm formation of NV centres after implantation optical measurements are performed with a confocal microscope before and after implantation (Fig. 47). This measurements are executed by our project collaborate from the Mainz University in terms of the "Quantum computing" project. Measurements performed by Dr. Yevgeniy Shapiro using original confocal fluorescence microscopy setup introduced in the Chapter 3.5. More details about the setup could be found in the dissertation work of Dr. Yevgeniy Shapiro.[3]

Optical measurements on the sample MZ15 reveals typical XZ depth profile with bulk at $z > 40$ µm and air at $z < 40$ µm. Laser power of 200 mW applied during the measurements. The weak signal at $z = 40$ µm seen before implantation is due to spurious fluorescence from the surface. The right fluorescence measurements figure taken after implantation reveals a typical XZ depth profile with diamond at $z > 50$ µm, air at $z < 50$ µm and a stripe of NV^- centers near the surface.

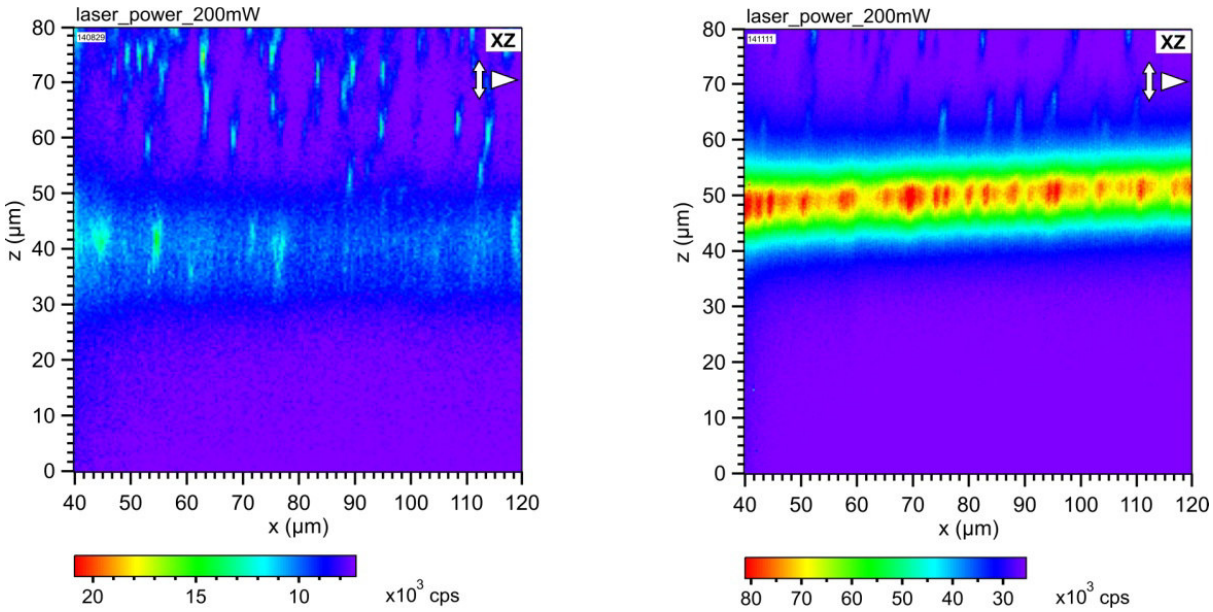

Fig. 47 Sample # MZ15 CVD EL grade fluorescence before and after 1 keV N_2 implantation.

CW (unmodulated, constant wave) ODMR measurements reveals presence of NV^- clusters. According to rough statistical estimation the concentration was increased by a factor of 1000 to 0.15% to N. The T1 polarisation decay and Rabi-Nutation measurements at 2.875 GHz MW antenna power confirm NV^- centres clusters signal. Optical measurements report no photoactivation or photobleaching observed during all measurements. For more details on fluorescence and ODMR measurements please refer to the the dissertation of Dr. Yevgeniy Shapiro (Chapter 5.4).[3]

Conclusion

Successful generation of the shallow NV centres by means of low energy plasma implantation has been demonstrated. Fluorescent measurements confirm clear formation of the NV clusters, what is also proved by additional ODMR, revealing presence of the NV^- centers.

4.5.4. Effect of X-ray irradiation on the near- surface electronic structure

For production of the NV centres ultrapure diamond required, in order to have the possible lowest nitrogen concentration and no or minimum NVs content in the "as grown" sample.

The CVD electronic grade (EL) diamond sample # DS7 a size of 3.5 x 3.5 x 0.5 mm^3 and (100) surface orientation has been used. The nitrogen concentration of the type IIa material is specified by the manufacturer (Element Six Ltd., Ascot, United Kingdom) to be below 5 ppb and boron concentration below 1 ppb. Initial steps of surface preparation carried out by the manufacturer comprise mechanical polishing yielding a roughness of typically Ra < 5 nm. Previous to the implantation sample has been boiled in a strongly oxidizing acid solution mixture of H_2SO_4, HNO_3 and $HClO_4$ a 1:1:1 acid mixture of for 4 h at a temperature of 359±2 °C and rinsed in Type I purified laboratory water (Arium 611UV, Sartorius AG, Goettingen, Germany).

Sample DS7 was fixed with a hard tantalum mask on the tantalum table, equipped with tungsten heating wire under the table (right in Fig. 17). Temperature controlled by two thermocouples, one attached with a molybdenum screw on top of the tantalum mask fixing sample on the table, another attached to massive sample holding construction (left in Fig. 17).

The sample is examined by XPS using same instrumentation, namely an X-ray source XR 50 (SPECS Surface Nano Analysis GmbH, Berlin, Germany) and a HSA PHOIBOS 100 (SPECS Surface Nano Analysis GmbH, Berlin, Germany) with a five MCDs yielding resolution of 0.2 eV. Photoelectron spectra are taken using non-monochromatic radiation from the Mg K-α line with photon 1253.6 eV. Heating of 350° C is applied during the measurements.

First sample measured by means of the optical spectroscopy and ODMR. These studies performed by Dr. Yevgeniy Shapiro using original confocal fluorescence microscopy setup introduced in the Chapter 3.5. More details about the setup could be found in the dissertation work of Dr. Yevgeniy Shapiro.[3] Figure 48a presented a fluorescent measurement of sample initial state. Optical measurements on the sample DS7 reveals typical XZ depth profile with a surface at z > 27 μm. Laser power of 200 mW applied during the measurements.

Next sample has been boiled again in a wet chemical 1:1:1 acid mixture of H_2SO_4, HNO_3 and $HClO_4$ for 4 hours according to our standard procedure (please see Chapter 3.8).

After re-transferring the sample into the UHV spectroscopy chamber (a base pressure below $8 \cdot 10^{11}$ mbar), it was flashed to a temperature of 790 °C for 3 minutes for adsorbates cleaning purposes. It should be mentioned that during XPS measurements a very long Auger NKLL line scan performed. That means sample has been exposed to X-ray irradiation a photon of 1253.6 eV for 6 hours. Than sample # DS7 annealed by electron bombardment in vacuum ($8 \cdot 10^{11}$ mbar) at 820° C for 2 hours to form NV centres.

After sample was again extracted from the chamber and measured by optical spectroscopy, and ODMR. In the Fig. 48b presented fluorescent measurement after annealing at 820° C for 2 hours. Optical measurements on the sample DS7 reveals XZ depth profile with a surface at z > 22 μm. Laser power of 200 mW applied during the measurements. Remarkably strong intensity region (white colour) appears in the fluorescent scan after sample treatment presented in the Fig. 48 as a comparison of fluorescence intensity.

As for instance a number of samples have been prepared using our standard acid treatment procedure, but such an effect has been never observed. The creation of strong intensity region is an effect of a long X-ray irradiation and following high temperature annealing steps is supposed. Figure 49 shows optical measurement, performed by Rajesh Tamang, of the DS7 sample before and after treatment.

Spectra recorded after irradiation and annealing reveals the intensity from the combined peak consisting of Raman line at 573 nm and the NV^0 center at 575 nm. At the same time NV^- is absent in the spectra and no ODMR effect reported from bright layer in the Fig. 48.

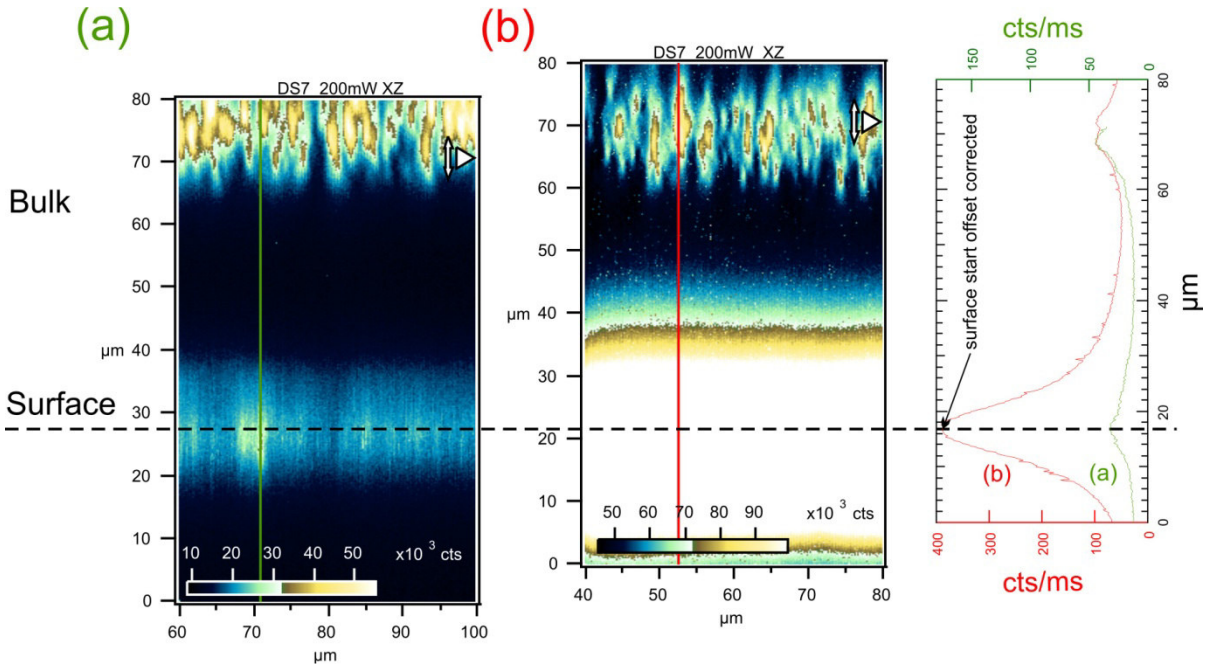

Fig. 48 Fluorescent measurement before a) and b) after irradiation and following annealing in UHV at 820° C for 2 hours, and a comparison of fluorescence intensity.

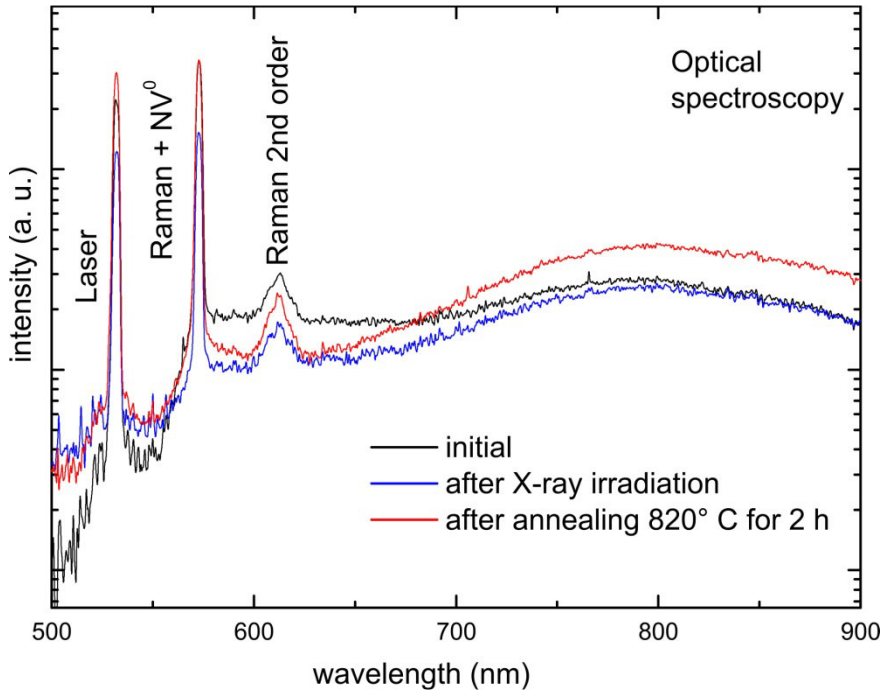

Fig. 49 Optical spectroscopy measurement of the DS7 sample after irradiation and annealing.

The treatment modifies the crystalline nature of the sample, possibly contributing to NV^0 centers stating from the fact that NV^0 center has its maximum phonon side band (PSB) at ~570 nm. The maxima at ~800 nm are possibly due to others vacancy related defect complexes.

Photoelectron effect due to X-ray irradiation accompanied with an electron ejection from a sample and creation of an additional vacancy (Fig.20 in Chapter 3.3.). In metals this additional vacancy will be fast filled with another electron, but in the semiconductor such as diamond that is not so straight forward and one end up with the situation when more and more vacancies would be generated upon the X-ray exposure time. Especially considering the pure electronic grade diamond sample, that has no or a very weak bulk conductivity comparing to the p- or n- doped diamonds. Thus the long X-ray exposure and long high temperature annealing possibly contributing to NV^0 centers or others vacancy related defect complexes generation is supposed.

Conclusion

The impact of prolonged X-ray irradiation followed by annealing on the surface of an electronic-grade IIa CVD (100) N < 5 ppb diamond, which results in a significant increase of the fluorescence signal, possibly contributing to NV^0 centers or others vacancy related defect complexes formation, has been reported.

4.6. Effect of the oxidation and hydrogen termination on the diamond surface

It has been shown already that stabilization of NV^- centers requires additional step of surface oxidation. It is also known that the diamond surface termination strongly influences the balance between NV^- and NV^0 centers by charge state conversion.[4-6] As it was demonstrated, for instance the oxidation of bulk diamond as well as of nano-diamond favors NV^- centres.[7, 8]

Oxidative treatment usually performed by means of oxygen plasma. However it is not always accessible and convenient to use plasma treatment comparing to extensively used wet acid chemical treatment methods. Here several alternatives to plasma treatment chemical oxidation methods have been presented and compared in order to reveal oxidation efficiency for all of them.

It is reported in the literature that hydrogen terminated surface reveals remarkable photoelectron emission properties[9, 10] due to negative electron affinity (NEA)[11]. Also some applications[12] and measurements like noncontact atomic force microscopy (NC-AFM)[13], Kelvin force microscopy (KFM)[14] or scanning tunneling microscopy (STM)[15] where diamond used as substrate require good surface conductivity. This could be achieved by means of surface hydrogen termination.[16] However, hydrogen termination supress significantly the luminescence of NV centres.[17] Here comparison between standard hydrogen termination by hydrogen plasma and wet acid treatment has been present.

4.6.1. Diamond surface oxidation

The CVD grown diamond samples (Sample # 34, Sample # 44) with a size of 3 x 3 x 0.5 mm^3 and (100) surface orientation have been used. The nitrogen concentration of the type IIa material is specified by the manufacturer (Element Six Ltd., Ascot, United Kingdom) to be below 1 ppm. Initial steps of surface preparation carried out by the manufacturer comprise mechanical polishing yielding a roughness of typically Ra < 30 nm.

The combination of two measurements technics has been used to evaluate surface oxygen termination of diamond sample. First is XPS, that allow to get atomic percentage (At%) concentration of oxygen defined by the O1s peak. Second is WCA measurements that are executed to evaluate the hydrophilicity of the diamond surface.

According to the literature oxygenated diamond surface reveals WCA angles 10° – 30°.[5, 17-19] WCA measurements reveal wetting effect, which shows surface hydrophilic or hydrophobic properties and how strong they are (Chapter 3.7.). The WCA measurements performed by the setup Drop Shape Analyzer – DSA100 (KRÜSS GmbH, Hamburg, Germany) and water droplet of 1 ml of Type I purified laboratory (Arium 611UV, Sartorius AG, Goettingen, Germany) has been used.

After oxidative treatments samples transferred the sample into the UHV spectroscopy chamber (a base pressure below $8 \cdot 10^{11}$ mbar. The sample is examined by XPS using our standard instrumentation, namely an X-ray source XR 50 (SPECS Surface Nano Analysis GmbH, Berlin, Germany) and a HSA PHOIBOS 100 (SPECS Surface Nano Analysis GmbH, Berlin, Germany) with a five MCDs yielding resolution of 0.2 eV. Photoelectron spectra are taken using non-monochromatic radiation from the Mg K-α lines with photon 1253.6 eV.).
It has been reported in the literature oxygen desorption occur in the range 480 – 600° C.[20] Thus prior to the measurements for cleaning purposes in order to remove physisorbed adsorbates samples heating performed only at temperature of 450° C.

Surface oxidation is accomplished by two acid treatment procedures. The sample 44 is either boiled in a mixture of H_2SO_4 /HNO_3 /$HClO_4$ acids for 4 hours according to our standard procedure (Chapter 3.8.). This type of termination gives O1s peak value of 5.5 At%, and WCA around 57° determined by the Young–Laplace (Y-L) method (Fig. X).

In order to increase the oxidation efficiency another wet chemical oxidation has been proposed. Sample 44 was treated with H_2SO_4 / $KMnO_4$ at 50° C for 30 min, which give higher values of oxygen O1s peak concentration is 15.4 At% and WCA value 54° (Y-L) (Fig. 50). The drawback of this method is sample contamination with metals, minor intensity of Mn and Fe peaks has been detected by XPS.

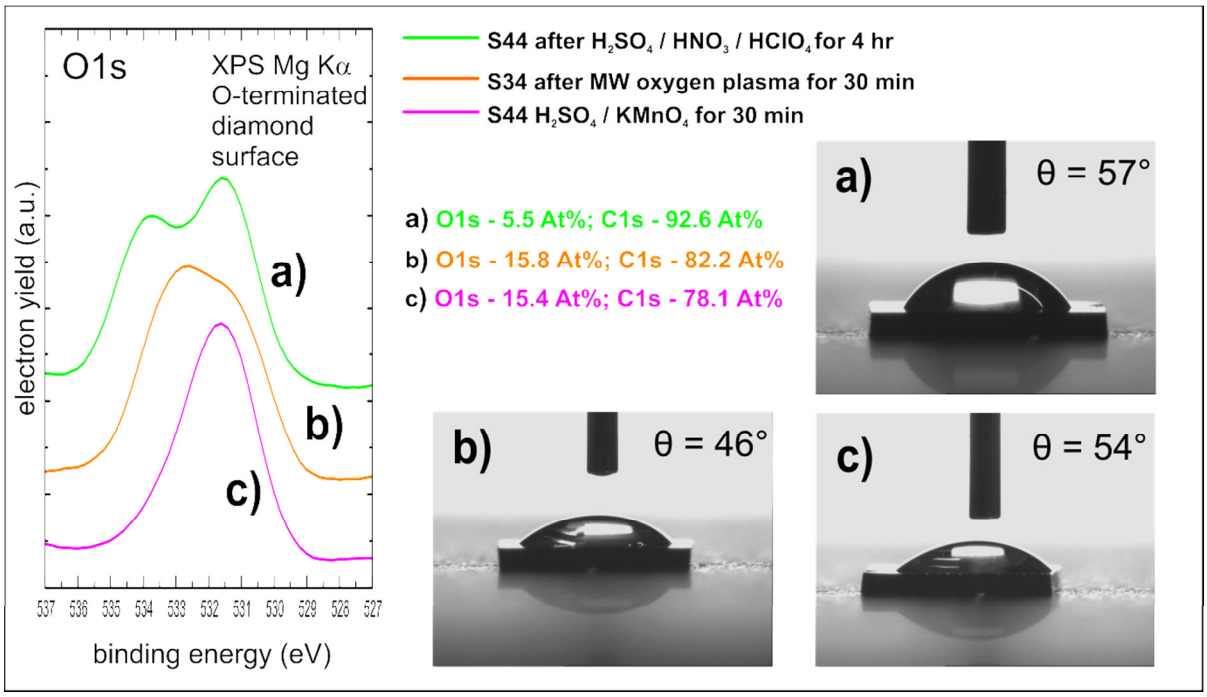

Fig. 50 XPS spectra of O1s peak and WCA measurements for O-terminated diamonds

Another widely used method for oxygen termination is the oxygen plasma treatment. Same type of diamond sample # 34 has been terminated by a microwave plasma (MW) reactor a power of 250 W with molecular oxygen gas inlet P(O_2) = 55 sccm and chamber pressure P = 0.2 torr for 20 min. According to XPS measurements oxygen concentration is about 15.8 At% and WCA value is 46.5° by Y-L method. All results are has been summarized in the Table 4.

Sample. #	Treatment	Contact angle θ	Oxygen concentration O1s peak
44	H_2SO_4 /HNO_3 /$HClO_4$	57.7°	5.5 At %
44	H_2SO_4 / $KMnO_4$	54.0°	15.4 At %
34	MW oxygen plasma	46.5°	15.8 At %

Table 4 Oxidation results for different treatment types

Oxygen treatment WCA give slightly higher contact angle values comparing to the literature values. This could explained by the dependence of surface tension from the purified Type I water used in the experiment, which is used to be highly deionized water. WCA values could be also improved by longer sample exposure times to the oxygen plasma or increasing plasma power.

Conclusion

The process of oxygen treatment has been analyzed via XPS spectroscopy and WCA measurements. The measurements show results of three different oxygen termination procedures, two wet chemical treatment procedures and the oxygen plasma treatment. The best diamond surface oxidation has been achieved via plasma treatment and reveals close to the literature values. At the same time wet chemical treatment could be used as alternative treatment procedure, or for surface cleaning purpose. It gives reasonable oxidation efficiency values and may be implemented for surface diamond preparation, depending on the final surface state requirements.

4.6.2. Diamond surface hydrogen passivation

The CVD grown diamond samples # 4 and # 33 a size of 3 x 3 x 0.5 mm^3 and (100) surface orientation for the hydrogenation experiments have been used. The nitrogen concentration of the type IIa material is specified by the manufacturer (Element Six Ltd., Ascot, United Kingdom) to be below 1 ppm. Initial steps of surface preparation carried out by the manufacturer comprise mechanical polishing yielding a roughness of typically Ra < 30 nm.

The combination of two measurements technics has been used to evaluate surface oxygen termination of diamond sample. First is WCA measurements executed to evaluate the hydrophobicity of the diamond surface. Second is XPS, that allow to get atomic percentage (At%) concentration of oxygen defined by the O1s peak.

According to the literature hydrogenated diamond surface reveals WCA angles 80° – 90°.[17, 18, 21, 22] WCA measurements disclose wetting effect, which shows surface hydrophilic or hydrophobic properties and how strong they are (Chapter 3.7.). The WCA measurements performed by the setup Drop Shape Analyzer – DSA100 (KRÜSS GmbH, Hamburg, Germany) and droplet of 1 ml of Type I purified laboratory water (Arium 611UV, Sartorius AG, Goettingen, Germany) has been used.

After hydrogen termination samples were transferred into the UHV spectroscopy chamber (a base pressure below $8 \cdot 10^{11}$ mbar). The samples were examined by XPS using our standard instrumentation, namely an X-ray source XR 50 (SPECS Surface Nano Analysis GmbH, Berlin, Germany) and a HSA PHOIBOS 100 (SPECS Surface Nano Analysis GmbH, Berlin, Germany) with a five MCDs yielding resolution of 0.2 eV. Photoelectron spectra are taken using non-monochromatic radiation from the Mg K-α lines with photon 1253.6 eV. Heating of 350° C is applied during the measurements.

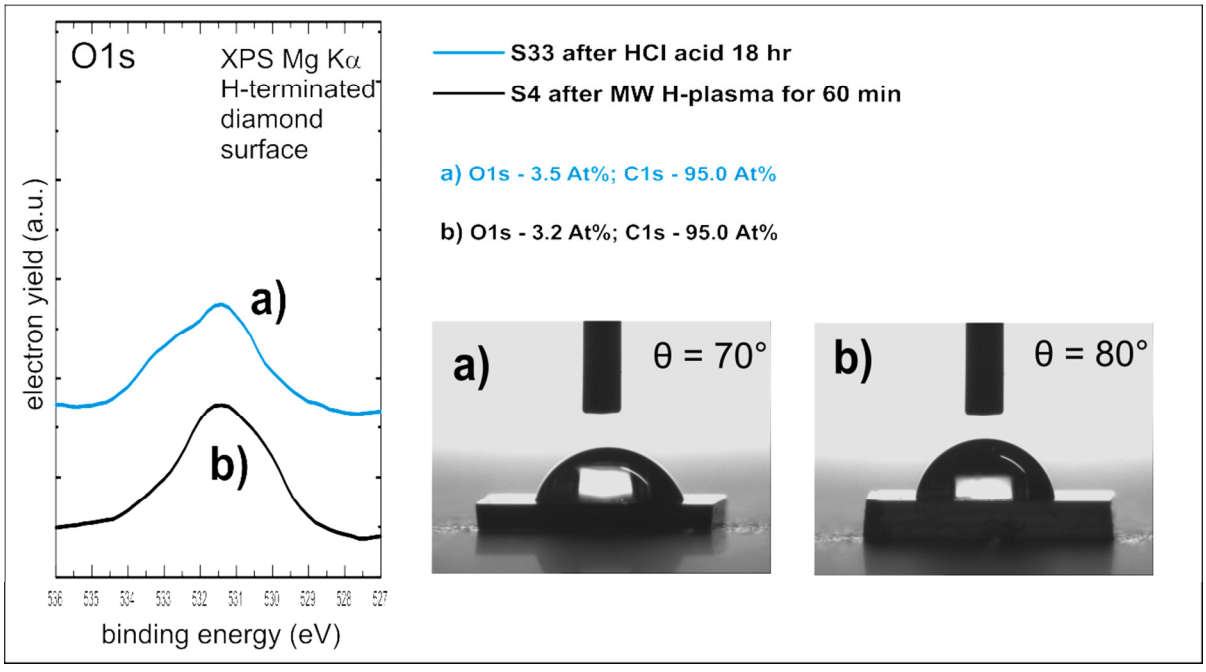

Fig. 51 XPS spectra of O1s peak and WCA measurements for H-terminated diamonds

Plasma termination has been performed by our colleagues in Paris. The microwave plasma (MW) reactor with a maximum power of 2200 W was used. The sample treated with plasma a power of 700 W temperature hold in the range of 780 - 820° C hydrogen pressure

1.5 x 10^6 mbar for 60 minutes. Afterwards the probe cooled down for a 2 hours before removing from the reactor.

The wet treatment performed in our lab by HCl acid purity of 99.999% (Sigma-Aldrich, St. Louis, USA). Sample # 33 was immersed in the HCl acid at RT for 18 hours, after extraction from the acid sample rinsed extensively by Type I purified laboratory water and dried.

It has been reported in the literature hydrogen desorption occur at a high temperatures in the range of 726 – 1126° C.[23, 24] Thus after transferring samples in the UHV chamber prior to the measurements for cleaning purposes in order to remove physisorbed adsorbates samples flashed shortly at lower temperature of 680° C for 3 m.

In the Fig. 51 the XPS spectra of O1s peak is shown. Samples have been flashed shortly up to 680 °C, however the oxygen could be still resolved, revealing 3.2 At% concentration for the for plasma terminated sample and 3.5 At% for the acid treated sample. As other samples these two also reflect Ca contamination, presumably induced by polishing procedure. Thus small detected amount of oxygen is related to calcium-oxygen bonding, e.g. calcite or other is supposed. Treatment results are summarized in the Table 5.

Sample #	Treatment	Contact angle θ	Oxygen concentration O1s peak (At %)
5	Hydrogen plasma	82.9°	3.2
33	HCl acid RT for 18 h	70.5°	3.5

Table 5 Hydrogenation results for different treatment types.

Hydrogen treatment WCA give slightly lower contact angle values comparing to the literature values. This could be explained by the dependence of surface tension from the purified Type I water used in the experiment, which is used to be highly deionized water. WCA values could be improved by longer sample exposure times to the hydrogen plasma or increasing plasma power.

Conclusion

The process of hydrogen treatment has been analysed via XPS spectroscopy and WCA measurements. The measurements show higher contact angle values for hydrogen plasma treated sample and thus better hydrophobicity. However HCl acid treatment considered to be a good solution for fast hydrogenation of the diamond surface. It gives reasonable hydrogenation efficiency value and may be implemented for surface diamond preparation, depending on the final surface state requirements.

4.7. Hydrogen terminated diamond surface

Investigation of the hydrogen terminated diamond surfaces attracted high interest in the research community due to its unique properties. In the previous Chapter 4.6 and 4.6.2 exemplified why the hydrogen terminated surface is so important. Also WCA measurements presented, revealing H plasma and HCl acid treatment efficiency. Here same type of hydrogen surface preparation characterized by means of XPS, MIES and UPS spectroscopy presented.

The same CVD grown diamond samples # 4 and # 33 a size of 3 x 3 x 0.5 mm^3 and (100) surface orientation for the studies have been used. The nitrogen concentration of the type IIa material is specified by the manufacturer (Element Six Ltd., Ascot, United Kingdom) to be below 1 ppm. Initial steps of surface preparation carried out by the manufacturer comprise mechanical polishing yielding a roughness of typically Ra < 30 nm.

The sample is examined by XPS using same instrumentation, namely an X-ray source XR 50 (SPECS Surface Nano Analysis GmbH, Berlin, Germany) and a HSA PHOIBOS 100 (SPECS Surface Nano Analysis GmbH, Berlin, Germany) with a five MCDs yielding resolution of 0.2 eV. Photoelectron spectra are taken using non-monochromatic radiation from the Mg K-α lines with photon 1253.6 eV. Heating of 350° C is applied during the measurements.

For UPS and MIES measurements used a helium double discharge plasma source presented in the Chapter 4.1. For UPS analysis photons energy of 21.2 eV and for MIES metastable helium atoms energy of He*(2^3S) = 19.82 eV were used. During measurements the sample is biased by -15.00 V. Work function calculated by the same formula presented in the Chapter 4.1. using the photons energy or metastables correspondently.

Plasma termination has been performed by our colleagues in Paris. The microwave plasma (MW) reactor with a maximum power of 2200 W was used. The sample treated with plasma a power of 700 W temperature hold in the range of 780 - 820° C hydrogen pressure 1.5 x 10^6 mbar for 60 minutes. Afterwards the probe cooled down for a 2 hours before removing from the reactor. The wet treatment performed in our lab by HCl acid. Sample # 33 was immersed in the HCl acid at RT for 18 hours, after extraction from the acid sample rinsed extensively by Type I purified laboratory water and dried.

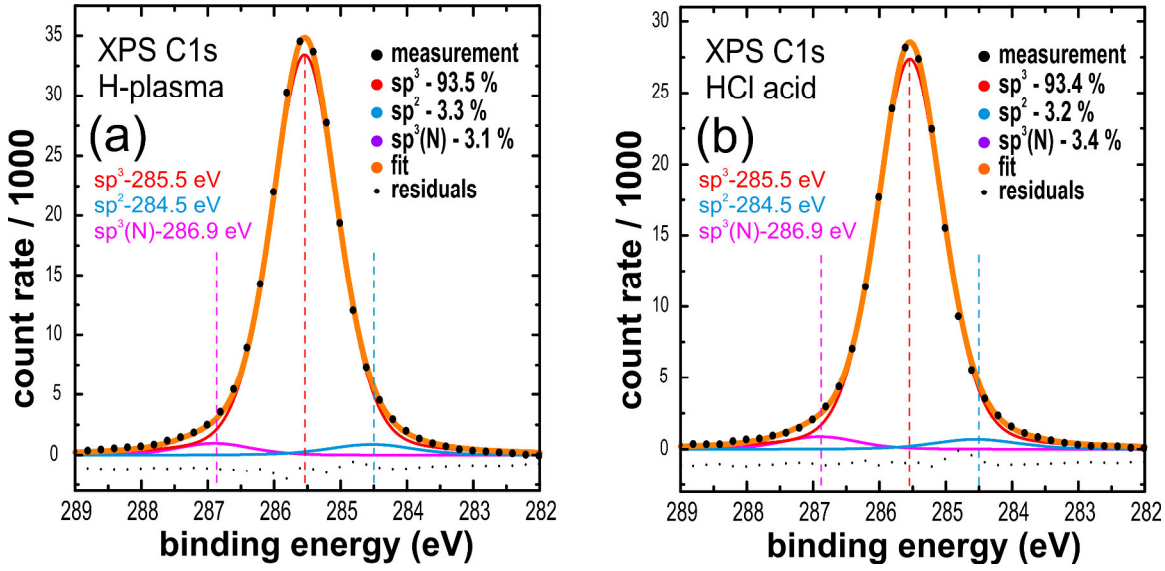

Fig. 52 XPS C1s peak deconvolution components for a) Sample 33 HCl acid treated 12h and 790° C flashed and b) Sample 5 treated with hydrogen plasma and flashed 790° C.

After re-transferring the sample into the UHV spectroscopy chamber (a base pressure below $8 \cdot 10^{11}$ mbar), it was flashed to a temperature of 790 °C for 1 minute for cleaning purposes.

Following the same deconvolution approach of the C1s peak, described in details in the Chapter 4.3, main components have been defined. There are also three additional minor deconvolution components, namely oxidation related peaks C-O (1), C-O (2) and the tail of the π- π* loss energy peak. Peaks related to either C=O or C-O-C bridge bonding appear at 287.5 eV and 288.5 eV, while the feature related to the π-π* transition is shifted by about 6 eV relative to the sp^2 peak. However, none of these components contribute significantly in improving the fit and these additional peaks reveal only 1 to 2 % to the total intensity. Therefore, they are not shown in the spectra.

In the Fig. 52a presented a deconvolution of the C1s carbon peak of sample # 4 revealing 93.5 % for sp^3, 3.3 % for sp^2 and 3.1 % for sp^3 (N) correspondingly. Deconvolution results for the sample # 33 are 93.4 % for sp^3, 3.2 % for sp^2 and 3.4 % for sp^3 (N). The XPS C1s peak full width half maximum (FWHM) of the HCl treated sample # 4 reveal the value of 1.16 and for the plasma treated sample # 4 the FWHM value is 1.18.

Fig. 53 shows results of the UPS (left) and MIES (right) surface spectroscopy for the HCl treated sample # 33 (blue line) and the H-plasma terminated sample # 4 (red line). In the UPS and MIES both samples spectra has similar shape, however the UPS spectra of the H-plasma treated sample have a slightly higher intensity in the valence band (VB). UPS measurements for reveal same position of the bulk $C(2p)_N$ states for both samples.

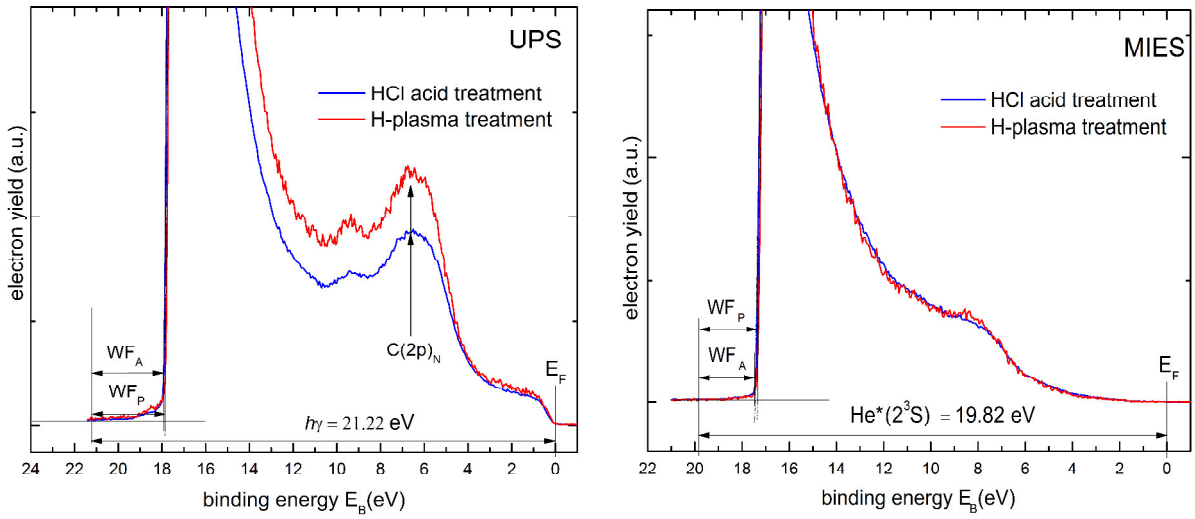

Fig. 53 UPS (left) and MIES (right) spectra of H-plasma and HCl acid treated samples.

According to UPS the work function WF_A = 3.3 eV for HCl acid treated sample and for H-plasma treated sample WF_P = 3.36 eV. The MIES spectra reveals work function WF_A = 2.37 eV for HCl acid treated sample and for H-plasma treated sample WF_P = 2.48 eV.

Conclusion

The process of hydrogen treatment has been analysed via XPS, UPS and MIES spectroscopy. The measurements show very close FWHM of C1s as well as deconvolution analysis values. However the UPS and MIES reveal slightly lower WF values of the HCl treated sample. It can be concluded that the HCl acid treatment gives the same spectroscopy values as H-plasma treated sample and WF values are in a good agree with literature.[25]

4.8. Fullerene molecule C_{60} deposition on diamond surface

According to the proposed diamond computing concept $N@C_{60}$ molecules should be positioned on the top of the diamond surface with the enclosed NV^- vacancies[26] (Chapter 1.1.). The MIES and UPS measurements on fullerene molecule C_{60} deposition on the clean diamond surface reported in this chapter.

For this initial experiment C_{60} molecule instead of $N@C_{60}$ has been used, because the production of the nitrogen doped fullerene molecules is quite hard and long-lasting process, so for a preliminary experiments could C_{60} molecule be used. Fullerene C_{60} molecule studies has been already reported by AFM studies.[27]

For this study, the CVD grown diamond sample # 21 with a size of 4.5 x 4.5 x 0.5 mm^3 and (100) surface orientation has been used. The nitrogen concentration of the type IIa material is specified by the manufacturer (Element Six Ltd., Ascot, United Kingdom) to be below 1 ppm. Initial steps of surface preparation carried out by the manufacturer comprise mechanical polishing yielding a roughness of typically Ra < 30 nm and boiling in a strongly oxidizing acid solution composed of H_2SO_4 and KNO_3. The laboratory treatment starts with rinsing the surface with HPLC grade ethanol and dry wiping with an optical paper. After transferring the sample into the UHV chamber having a base pressure below $8 \cdot 10^{11}$ mbar, it is flashed to a temperature of 790°C for 3 minutes to remove volatile adsorbed species like water and hydrocarbons. All subsequent preparation steps and further measurements are performed in situ in the UHV environment except for the final step of wet chemical etching.

For UPS and MIES measurements used a helium double discharge plasma source presented in the Chapter 4.1. For UPS analysis photons energy of 21.2 eV and for MIES metastable helium atoms energy of $He^*(2^3S)$ = 19.82 eV were used. During measurements the sample is biased by -15.00 V. During operation of the electron analyser for collecting MIES/UPS spectra, the current for heating the C_{60} evaporator is switched off to avoid a deterioration of electron spectra due to current-induced magnetic stray fields.

For the deposition C_{60} purity of 99.5% (Sigma Aldrich, St. Louis, USA) powder has been used. The quartz tube used for the evaporation is supplemented with heating wire and the K-type thermocouple positioned at the about 45° angle towards the sample and a distance around 10 cm.

After charging the sample into the UHV spectroscopy chamber (a base pressure below $8 \cdot 10^{11}$ mbar), it was flashed to a temperature of 790 °C for 3 minutes for adsorbates cleaning purposes.

Next C_{60} molecules RT deposited on the clean diamond surface. The MIES and UPS measurements of the C_{60} multilayer, deposited on the diamond surface, are shown in the Fig. 54. Both UPS – black line and MIES – blue line measurements present the Tougaard method subtracted background spectra. Experimental data is compared to the valance band theoretical calculation for the fullerene molecule orbitals.[28-30] The UPS data values perfectly fit theoretical DOS calculations, corrected by 2.49 eV. Applied correction most likely originated from the difference between the calculated DOS and the measured surface DOS (SDOS). After small 0.25 eV shift MIES data is also in the good agreement with the theoretical calculations. This shift could be explained by the difference in the theoretical calculations for bulk the bulk density of stated (DOS) and the surface density of stated (SDOS). As long as theoretical values used in the comparison relates to bulk DOS and the MIES measurements basically probes the utmost surface states, and reveal SDOS. Thus the correlation between theoretical calculations and the MIES measurements are in a very good agreement.

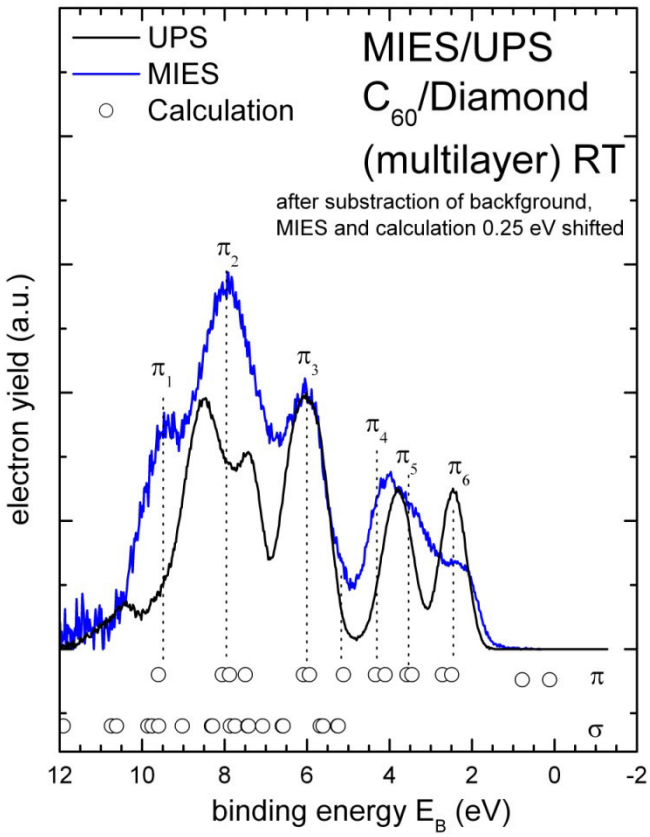

Fig. 54 MIES and UPS spectra comparison of C_{60} multilayer deposited on CVD diamond surface and a C_{60} theoretical DOS calculations.

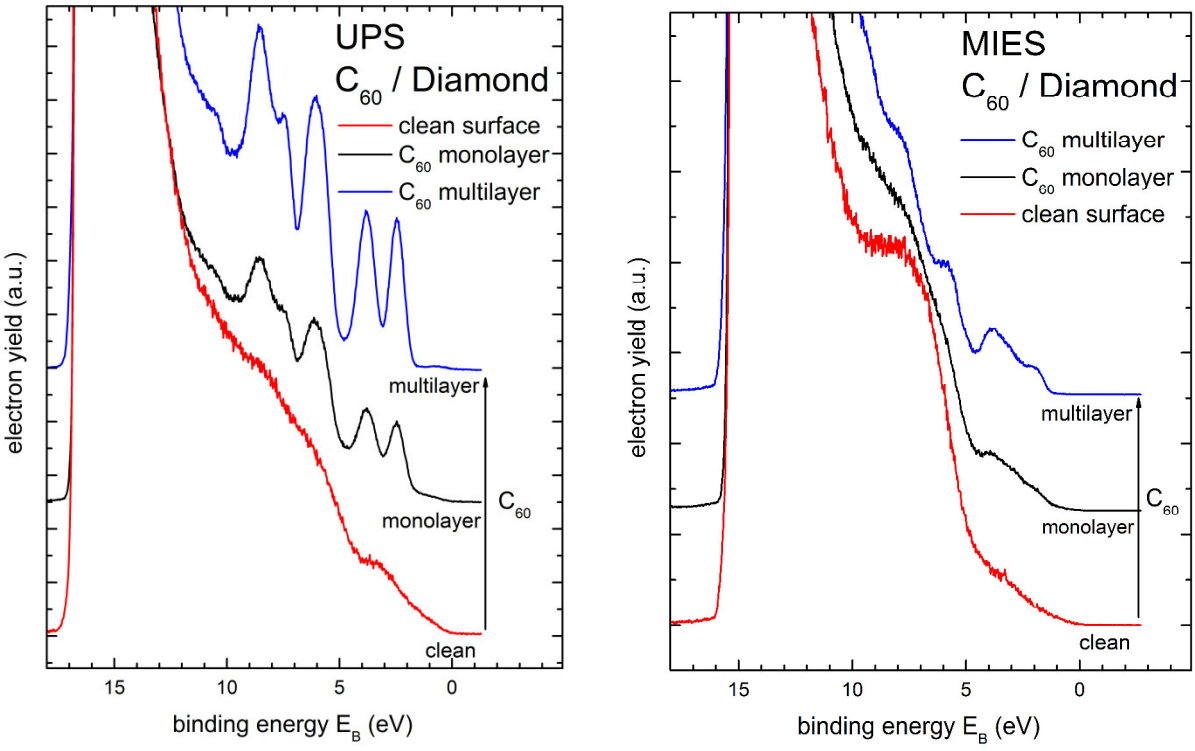

Fig. 55 UPS and MIES spectra comparison of C_{60} multilayer, C_{60} monolayer and a clean C_{60} free diamond surface.

It has been reported in the literature that physical vapor deposition (PVD) of the C_{60} molecules at the elevated temperature ~200° C (473 K) surface results in a one C_{60} monolayer (1 ML) deposition.[31, 32]

After C_{60} multilayer deposition, sample flashed at 890° C and shown in the Fig. 55 (red line). Next fullerene evaporation performed at 205° C (478 K) in order to obtain 1 ML of C_{60} molecules (Fig. 55 black line). Multilayer of the C_{60} molecules marked with a blue line in the Fig. 55. Both UPS (left) and MIES (right) spectroscopy measurements of clean, C_{60} monolayer and C_{60} multilayer are shown in the Fig. 55.

Conclusion

UPS and MIES measurements allow to implement the fullerene molecule deposition control on the diamond surface and to distinguish between the multilayer and monolayer of the C_{60} molecules. This knowledge could be implemented in the following experiments for the deposition of the $N@C_{60}$ on the diamond surface with the enclosed NV^- vacancies.

Chapter V

5. Instrumentation calibration

5.1. XPS calibration

The sample is examined by XPS using an X-ray source XR 50 (SPECS Surface Nano Analysis GmbH, Berlin, Germany) and a HSA PHOIBOS 100 (SPECS Surface Nano Analysis GmbH, Berlin, Germany) with a five MCDs yielding resolution of 0.2 eV. Photoelectron spectra are taken using non-monochromatic radiation from the Mg K-α line with photon energy of 1253.6 eV.

For the XPS calibration reference sample gold Au (111) on glass was used. Below the XPS spectra revealing Au $4f_{7/2}$ peak binding energy position of E_B = 84.0 eV. Background subtracted by Shirley method. Measurements performed at RT.

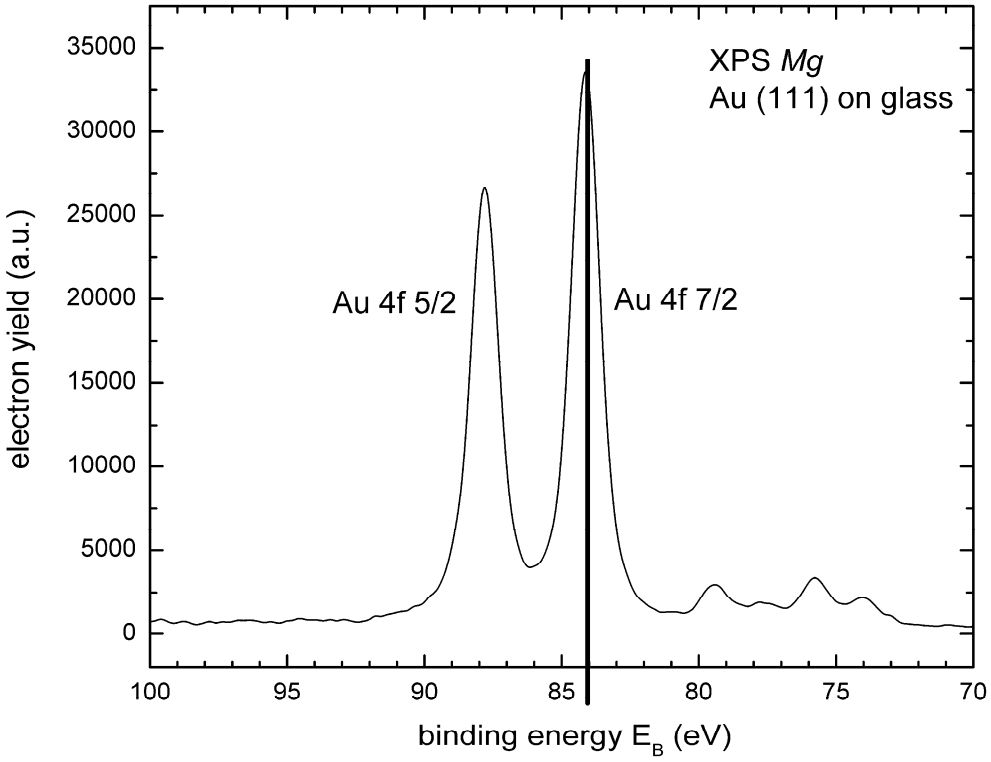

XPS spectra of gold Au (111) on glass Au $4f_{7/2}$ peak.

5.2. Temperature calibration

Our removable sample holder plate has additional construction for electron bombardment heating up to a 900° C and a K-type thermocouple attached near the sample position. In order to obtain accurate temperature measurement values calibration of the sample holder performed.

First standard K-type thermocouple T1 attached under the sample mask, this thermocouple is used during the measurements. Additionally K-type thermocouple T2 spot welded to the copper plate size 3 x 3 mm, located in the sample position. Two thermocouple meters VOLTCRAFT K204 (Conrad Electronic SE, Hirschau, Germany) attached to each thermocouple to track temperatures simultaneously. Than a stepwise annealing up to 920° C performed.

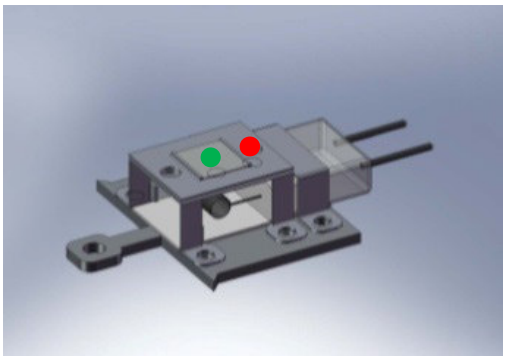

Removable sample holder plate with a heating option and K-type thermocouple. The red spot place where T1 thermocouple attached and the green spot at sample position where T2 thermocouple attached during calibration.

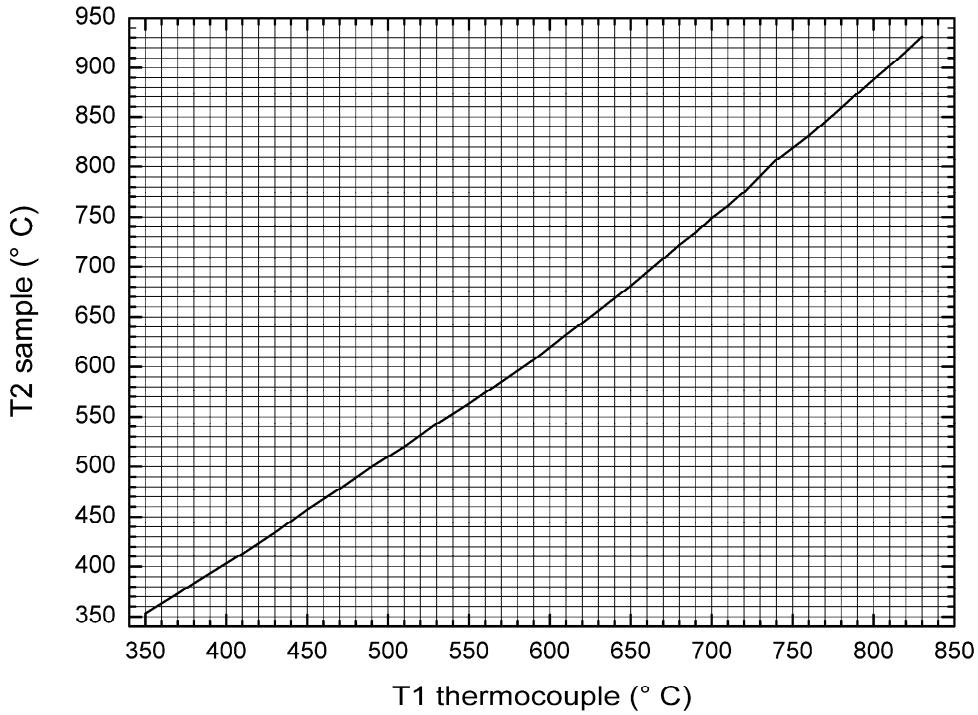

Calibration curve shows relation between T1 and T2, so that exact temperature value of the sample could be estimated.

5.3. Plasma source calibration

In order to control implantation and to perform precise implantation, the calibration procedure of our plasma source PCS ECR (SPECS Surface Nano Analysis GmbH, Berlin, Germany) performed. For measurement I took a piece of comparable to our standard diamond samples size 3 x 3 mm and isolate it from the sample holder. Wires connected to the plate were also isolate and attached to the feedthrough CF flange with output contacts outside the UHV chamber. A low current electrometer MODEL connected to the UHV CF flange feedthrough used to monitor beam currents. The plasma ignited and nitrogen gas pressure and as well as plasma source power has been tuned, and beam current has been tracked.

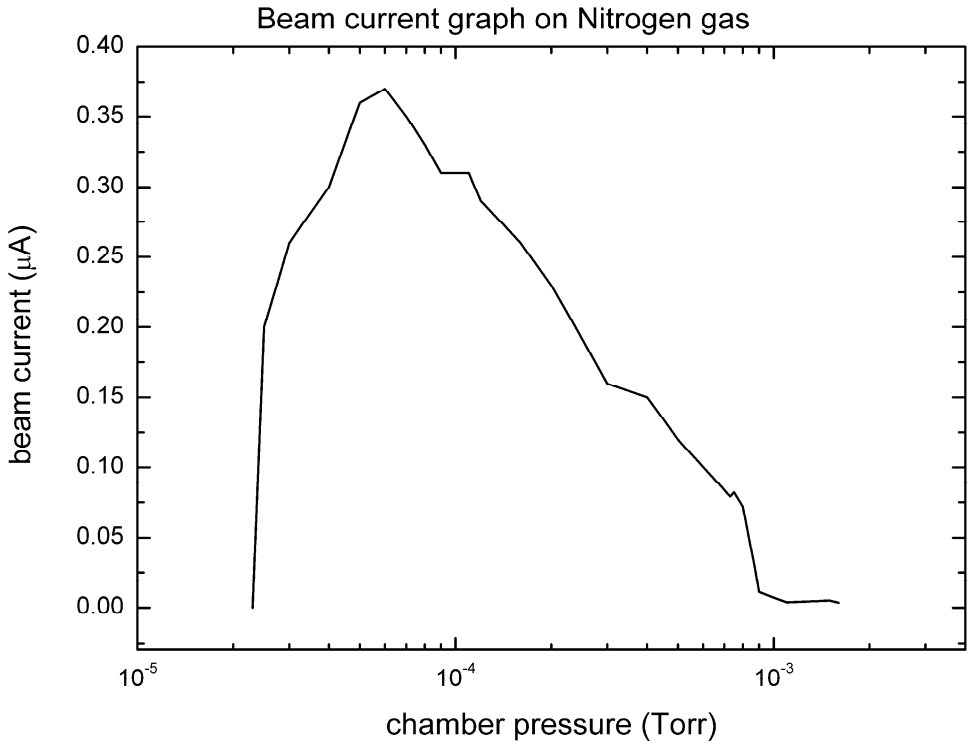

In the graph presented relation between beam current and chamber pressure in the logarithmic scale. The plasma source maximum beam current corresponds to the nitrogen gas pressure between 5 – 8 x 10^{-5} torr.

6. Summary

The core of this work is an attentive, precise characterization of CVD and HPHT diamond surface properties and establishing a method for nitrogen shallow implantation of diamond. In terms of the related project on diamond based quantum computing, the electronic and chemical properties have been analyzed by means of surface spectroscopy techniques. Techniques yielding a sampling depth of a few nm are X-ray photoelectron spectroscopy (XPS) and ultraviolet photoelectron spectroscopy (UPS) while the top surface layer has been probed by metastable impact electron spectroscopy (MIES). MIES has been introduced as a unique non-destructive surface spectroscopy technique with its instrumentation design in very detail and the strength and advantages of the MIES were illustrated by measurement examples on CVD diamond but also the rutile TiO2(110) surface.

It has been shown how the level of nitrogen doping in diamond can be measured and tracked by means of XPS and X-ray induced Auger lines analysis even for nitrogen concentrations as low as 1.5 At %, when the photoelectron peak N1s cannot be resolved. This has been an important development for the characterization of samples with shallow nitrogen implantation in small concentration.

This work also comprised studies revealing the diamond surface physics for different concentrations of nitrogen and boron doping, and showed how doping is reflected in the core shell analysis, valance band structure and work function values. It has been demonstrated that nitrogen doping shifts the carbon C1s core shell peak towards higher binding energy, whereas electronic grade and low nitrogen content (below 1 ppm) diamond samples reveal the intrinsic diamond sp3 position for the carbon C1s peak at EB = 285.5 ± 0.2 eV. An important result is, however, that the shift observed in the XPS spectrum is not a chemical shift but stems from a shift in the sample Fermi level upon doping. Consequently, a shift in the opposite direction is found for a boron doped diamond sample. When comparing UPS and MIES spectra, only minor band bending between sub-surface and top surface layers is found. However, the comparison of UPS and XPS exhibit a much stronger bend bending effect pointing to the different sampling depth of the methods. Based on the results from the combined surface spectroscopy studies, an indirect method of diamond doping determination and the categorization for different diamond doping scenarios has been suggested.

Besides controlling shallow implantation, the precise control of the outermost diamond surface state is crucial for the sub-system interface of the quantum computing assembly. Therefore, I carefully checked how the perfect phase purity of a diamond surface can be restored reproducibly after nitrogen implantation and further how clean, oxidized and hydrogen terminated surfaces can be prepared in a controllable way. I have shown that annealing of nitrogen implanted CVD (100) diamond at high temperature in oxygen leads to sample etching and amorphization. By consecutive acids treatment, the initial surface state even after strong surface amorphization can be recovered. A deconvolution of the XPS C1s component into several components has been performed and a comprehensive picture of the phases present at differently treated diamond surfaces has been developed based on the deconvolution results.

The second important issue addressed in this work was the controllable creation of nitrogen-vacancy (NV) centers accompanied by comprehensive surface spectroscopy studies. The generation of the shallow NV centers by means of 1 keV energy plasma implantation in an electronic grade IIa CVD diamond has been demonstrated. Fluorescence measurements and ODMR measurements performed by fellow scientists clearly confirmed the formation of NV^- centers near the surface for the prepared sample. Moreover, the effect of extended X-ray irradiation on an electronic grade IIa CVD diamond surface, which leads to a significant increase of the fluorescence signal possibly related to NV^0 centers or others vacancy defect

complexes has been observed. However, this conspicuous effect requires further detailed consideration.

With respect to diamond surface preparation, an alternative chemical method for the diamond surface oxidation has been proposed and compared to the standard oxygen plasma termination. The best diamond surface oxidation, revealed by water contact angle (WCA) measurements, has been achieved via MW plasma treatment. At the same time acid wet chemical treatment yielded reasonable oxidation efficiency and can be implemented for a diamond surface oxidation as an alternative treatment procedure, or for surface cleaning purposes.

Hydrogen terminated diamond surfaces produced by HCl acid for 18 h and by hydrogen plasma for 1 h treatment have been compared. Spectroscopy results demonstrate similar C1s peak full width half maximum (FWHM) and work function values for both hydrogenation methods, however, the WCA measurements revealed larger contact angle values and, thus, better hydrophobicity for the hydrogen plasma treated sample.

As a related aspect to the proposed diamond computing concept of $N@C_{60}$ molecules positioned on a diamond surface containing NV^- centers, I studied C_{60} molecules deposited on diamond. The deposition of C_{60} molecules on the diamond surface has been monitored by UPS and MIES spectroscopies. The fullerene multilayer and monolayer molecule deposition on the diamond surface was implemented and it has been demonstrated that measurements are in a good agreement with the theoretical DOS calculations for the C_{60} molecular layer. This study is preparatory work for following $N@C_{60}$ deposition experiments on the diamond surface prepared with NV^- centers.

References

1. J. Meijer, B. Burchard, M. Domhan, C. Wittmann, T. Gaebel, I. Popa, F. Jelezko and J. Wrachtrup, Appl. Phys. Lett. **87**, 261909 (2005).
2. S. Pezzagna, D. Rogalla, D. Wildanger, J. Meijer and A. Zaitsev, New J. Phys. **13**, 035024 (2011).
3. Y. Shapiro, Johannes Gutenberg-Universität Mainz, 2015.
4. S. Y. Cui and E. L. Hu, Appl. Phys. Lett. **103**, 051603 (2013).
5. K. M. C. Fu, C. Santori, P. E. Barclay and R. G. Beausoleil, Appl. Phys. Lett. **96**, 121907 (2010).
6. B. Grotz, M. V. Hauf, M. Dankerl, B. Naydenov, S. Pezzagna, J. Meijer, F. Jelezko, J. Wrachtrup, M. Stutzmann, F. Reinhard and J. A. Garrido, Nat. Comm. **3**, 729 (2012).
7. M. V. Hauf, B. Grotz, B. Naydenov, M. Dankerl, S. Pezzagna, J. Meijer, F. Jelezko, J. Wrachtrup, M. Stutzmann, F. Reinhard and J. A. Garrido, Phys. Rev. B **83**, 081304(R) (2011).
8. L. Rondin, G. Dantelle, A. Slablab, F. Grosshans, F. Treussart, P. Bergonzo, S. Perruchas, T. Gacoin, M. Chaigneau, H. C. Chang, V. Jacques and J. F. Roch, Phys. Rev. B **82**, 115449 (2010).
9. F. Maier, M. Riedel, B. Mantel, J. Ristein and L. Ley, Phys. Rev. Lett. **85**, 3472 (2000).
10. D. Takeuchi, M. Riedel, J. Ristein and L. Ley, Phys. Rev. B **68**, 041304 (2003).
11. L. Diederich, O. M. Küttel, P. Ruffieux, T. Pillo, P. Aebi and L. Schlapbach, Surf. Sci. **417**, 41 (1998).
12. C. E. Nebel, B. Rezek, D. Shin and H. Watanabe, Phys. Status Solidi A **203**, 3273 (2006).
13. M. Nimmrich, M. Kittelmann, P. Rahe, A. J. Mayne, G. Dujardin, A. v. Schmidsfeld, M. Reichling, W. Harneit and A. Kühnle, Phys. Rev. B **81**, 201403R (2010).
14. B. Rezek, New Diamond Front. Carb. Techn. **15**, 275 (2005).
15. R. E. Stallcup, II and J. M. Perez, Phys. Rev. Lett. **86**, 3368 (2001).
16. J. A. Garrido, T. Heimbeck and M. Stutzmann, Phys. Rev. B **71**, 245310 (2005).
17. V. Petrakova, M. Nesladek, A. Taylor, F. Fendrych, P. Cigler, M. Ledvina, J. Vacik, J. Stursa and J. Kucka, Phys. Status Solidi A **208**, 2051 (2011).
18. V. Seshan, D. Ullien, A. Castellanos-Gomez, S. Sachdeva, D. H. K. Murthy, T. J. Savenije, H. A. Ahmad, T. S. Nunney, S. D. Janssens, K. Haenen, M. Nesládek, H. S. J. van der Zant, E. J. R. Sudhölter and L. C. P. M. de Smet, J. Chem. Phys. **138**, 234707 (2013).
19. M. Geisler and T. Hugel, Adv. Mater. **22**, 398 (2010).
20. T. Ando, K. Yamamoto, M. Ishii, M. Kamo and Y. Sato, J. Chem. Soc., Faraday Trans. **89**, 3635 (1993).
21. M. Dankerl, A. Lippert, S. Birner, E. U. Stützel, M. Stutzmann and J. A. Garrido, Phys. Rev. Lett. **106**, 196103 (2011).
22. F. Fizzotti, A. Lo Giudice, C. Manfredotti, C. Manfredotti, M. Castellino and E. Vittone, Diam. Relat. Mater. **16**, 836 (2007).
23. C. Su and J. C. Lin, Surf. Sci. **406**, 149 (1998).
24. T. Yamada, T. J. Chuang, H. Seki and Y. Mitsuda, Mol. Phys. **76**, 887 (1992).
25. L. Diederich, O. Küttel, P. Aebi and L. Schlapbach, Surf. Sci. **418**, 219 (1998).
26. D. D. Awschalom, R. Epstein and R. Hanson, Sci. Am. **297**, 84 (2007).
27. M. Nimmrich, M. Kittelmann, P. Rahe, W. Harneit, A. J. Mayne, G. Dujardin and A. Kühnle, Phys. Rev. B **85**, 035420 (2012).
28. N. Troullier and J. L. Martins, Phys. Rev. B **46**, 1754 (1992).

29. J. L. Martins, N. Troullier and J. H. Weaver, Chem. Phys. Lett. **180**, 457 (1991).
30. J. H. Weaver, J. L. Martins, T. Komeda, Y. Chen, T. R. Ohno, G. H. Kroll, N. Troullier, R. E. Haufler and R. E. Smalley, Phys. Rev. Lett. **66**, 1741 (1991).
31. M. S. Dresselhaus, G. Dresselhaus and P. C. Eklund, *Science of Fullerenes and Carbon Nanotubes*. (Academic Press, 1996).
32. E. A. Katz, D. Faiman, S. Shtutina and A. Isakina, Thin Solid Films **368**, 49 (2000).

Curriculum Vitae

Oleksiy Dyachenko

Curriculum Vitae

Ziegelstr. 29
49074 Osnabrück
Telephone: +49(0)176 - 76555204
E-mail: oleksiydyachenko@gmail.com

Personal information

Date of birth	10.09.1984, Barvinkove, Kharkiv, Ukraine
Family status	Married

Education summary

Higher education

PhD study

02.2011– present	Osnabrück University, Physics department, AG Nanoscience
Subject	Applied experimental physics, Surface physics
Specialization	Molecules and nanostructures, semiconductor, metallic and dielectric materials, surface spectroscopy

Master degree

06.03.2009	Master's degree with honours
09.2007 – 03.2009	V.N. Karazin Kharkiv National University, Kharkiv, Ukraine
Subject	Applied physics
Specialization	Nanotechnology, thin films und nanostructures

Bachelor degree

03.07.2007	Bachelor’s degree
09.2003 – 07.2007	V.N. Karazin Kharkiv National University, Kharkiv, Ukraine
Subject	Applied physics
Specialization	Nanotechnology, thin films und nanostructures

School

08.2003	Secondary school certificate
09.1993 – 08.2003	Kharkiv secondary School # 62 with advanced study of English, Kharkiv, Ukraine

Professional experience

04.2009 – 10.2010	Institute for Scintillation Materials National Academy of Sciences of Ukraine, Kharkiv, Ukraine
Position	Lead engineer in department of single crystals growth technology
12.2008	Institute for Scintillation Materials National Academy of Sciences of Ukraine, Kharkiv, Ukraine
Position	Lead engineer in the scintillation crystals materials science and engineering department

Conferences and publications

Hasselt Diamond Workshop 2016 SBDD XXI 2016
Poster: “Effects of wet and dry etching on the phase purity of N-implanted CVD diamond surfaces”

Hasselt Diamond Workshop 2015 SBDD XX
Poster: "Controlled surface preparation, doping and shallow nitrogen implantation of diamond"

Hasselt Diamond Workshop 2014 SBDD XIX
Poster: "A cycle for producing perfectly stoichiometric and nitrogen doped surfaces of CVD diamond"

2nd International Symposium on Integration of Molecular Components in Functional Macroscopic Systems of the Volkswagen Foundation, Hannover 2014
Poster: "Preparing perfectly stoichiometric, hydrogen passivated and nitrogen doped diamond (100) surfaces"

Hasselt Diamond Workshop 2013 SBDD XVIII
Poster: "XPS, UPS and MIES investigations on nitrogen doped diamond after various surface treatments"

Article: *O. Dyachenko*, N. Diek, Y. Shapiro, R. Tamang W. Harneit, M. Reichling and A. Borodin / "A cycle for the repetitive preparation of diamond (100) with perfect phase purity"// Chem. Phys. Lett. 2015, v.640, p. 72–76, doi: 10.1016/j.cplett.2015.10.015

Article: A. Borodin*, O. Dyachenko*, M. Reichling / "Two-Discharge Source for Metastable Impact Electron Spectroscopy and Ultraviolet Photon Spectroscopy "// Rev. Sci. Instrum. 2016 (submitted)

Article: A.P. Kryshtal, M.M. Kolendovskij, *O.O. Dyachenko*, V.A. Sannik / Quartz resonator using for investigation phase transitions in condensed films // Collection of research materials "Physical and chemical principles of formation and modification of micro- and nanostructures" - 2008, v.1, p. 97

Languages

English	Fluent
Deutsch	Good
Ukrainian	Native
Russian	Native